Mean Loading and Turbulence Scale Effects on the Surface Pressure Fluctuations Occurring on a NACA 0015 Airfoil Immersed in Grid Generated Turbulence

Patrick F. Mish

Thesis submitted to the faculty of
Virginia Polytechnic Institute and State University
in partial fulfillment of degree requirements

Master of Science in Aerospace Engineering

William J. Devenport, Chair
Ricardo Burdisso
Roger L. Simpson

24 May 2001
Blacksburg, Virginia 24061

Keywords: surface pressure response, blade response function, blade/wake interaction, unsteady pressure

Mean Loading and Turbulence Scale Effects on the Surface Pressure Fluctuations Occurring on a NACA 0015 Immersed in Grid Generated Turbulence

Patrick F. Mish

(ABSTRACT)

Detailed surface pressure measurements have been made on a NACA 0015 immersed in two grid generated homogenous flows at Re = 1.17×10^6 for $\alpha = 0°, 4°, 8°, 12°, 16°$, and $20°$. The goal of this measurement was to reveal and highlight mean loading and turbulence scale effects on surface pressure fluctuations resulting from turbulence/airfoil interaction. Also, measurements are compared with the theory of Amiet (1976a,b). The surface pressure response shows a dependance on angle of attack, the nature of which is related to the relative chord/turbulence scale. The dependance on turbulence scale appears to be non-monotonic at low reduced frequencies, $\omega_r = \pi f c/U_\infty$ with both an increase and decrease in unsteady pressure magnitude occuring with increasing mean load. A reduced frequency overlap region exists at $\omega_r > 10$ where the two different scale flows begin to produce similar effects on the surface pressure with increasing angle of attack manifesting as a rise in unsteady surface pressure magnitude. Also, the interaction of the full 3-dimensional wavenumber spectrum affects the distance over which pressure fluctuations correlate and the extent of correlation is affected by angle of attack as demonstrated in the chordwise and spanwise pressure correlation. Amiet's theory is shown to agree favorably with measurements in the leading edge region although demonstrates insufficiencies in predicting unsteady pressure phasing.

ACKNOWLEDGEMENTS

The author would like to thank NASA Langley, in particular Casey Burley and Tom Brooks, for their support under grants NAG-1-1942 and NAG-1-2272. Additionally, the author would like to thank and recognize his advisor Dr. William Devenport. Dr. Devenport's continued patience and infinite insight jointed with his brilliant teaching ability has allowed for great personal growth and tremendous intellectual development without which this work would not be possible. The author considers himself exceptionally fortunate to have the opportunity to work with such a wise and knowledgeable researcher.

Furthermore, the author is in great debt to his parents, Bill and Dolores Mish and fiancé, Anne Sommers for their unrelenting support and encouragement throughout the development of this educational milestone. Also, the author thanks his very good friends (and colleagues) Diego de la Riva and Chittiappa Muthanna for their assistance, both technical and comical.

The author is indebted to Shigeo Hayashibara for his design, construction, and assembly of some 130 microphone circuits, in addition to early development of the prediction code. Semere Bereketab and Hongwei Wang are thanked for their assistance with hotwire measurements and the analysis thereof. Also, Mr. Bereketab's tuft flow visualization cinematography support is appreciated and the author wishes him much success in Hollywood. For Jon Vegard Larssen's assistance with wind tunnel noise assessment and microphone calibration and testing shake-down I express my gratitude. And finally, the author gratefully acknowledges Greg Dudding for his fine craftsmanship and impeccable attention to detail. Few individuals of his trade have the drive, focus, and inherent talent to bring to life the near impossible.

TABLE OF CONTENTS

TABLE OF FIGURES

Chapter 1. Introduction

When a lifting airfoil moves through a turbulent stream an unsteady pressure field develops around the airfoil which produces acoustic waves that manifest into broadband noise. Such phenomena can readily be identified in nearly all types of vehicles (e.g. automobiles, planes, helicopters, ships, submarines, etc.) the results of which can be quite troublesome. For example helicopter noise levels can easily approach 100dB with a large portion of this noise related to the rotor blades cutting through the wake of the leading blade. Sophisticated submarine propulsors which are similar in form to an axial compressor in a turbofan engine can produce considerable noise as the propulsor blades slice through boundary layer produced turbulence. In combat scenarios such noise levels obviously hamper the stealth capability of these vehicles. In addition, with the passage of Bills such as the "Silent Skies Act of 1999" industry is increasingly coming under pressure to reduce the levels of noise pollution associated with turbomachinery propulsors (i.e. turbofans, turbojets, etc) on their aircraft. For these reasons sophisticated models addressing the interaction of a lifting airfoil with turbulence are required.

The past 60 years has shown an increase in model complexity from the relatively crude flat plate approximation to the development of more complex numerical, distortion representations considering real airfoil geometry and angle of attack. The goal of any such model is to predict the unsteady pressure field occurring on the surface of the lifting airfoil which in turn allows the estimation of radiated noise levels. This cannot be accomplished without identifying the blade response function which represents the manner in which the airfoil responses to an incoming turbulent flow. With this target in mind researchers set out to develop a realistic and accurate formulation of the problem.

1.1 Understanding the Turbulence/Airfoil Interaction Problem: Flat Plate Models

The complex nature of turbulence interacting with a lifting body appears nearly intractable upon first sight. How is one to predict the fluctuating pressure or lift on the surface of an airfoil with finite thickness and mean loading in such a complicated process? Further concealing the solution is the distortion of the turbulence by the mean flow field as it impacts on the leading edge and then convects along the chord. The task is daunting, although the fundamental physics at work can be revealed through simplifications and assumptions leading to a practicable solution. Therefore, many researchers have approached this problem based on the assumption that 1) the disturbance (incoming turbulence) is considered to be small compared to the mean free stream velocity and 2) the interaction primarily inviscid thus the problem can be reduced to one of solving the linearized Euler equation.

1.1.1 The Incompressible Parallel Gust: An Exact Analytical Model

Von Karman and Sears (1938) followed by Sears (1941) were some of the first to pioneer the turbulence/airfoil interaction. Sears considers the case of a two-dimensional wing interacting with a sinusoidal gust convected with the free stream having its wave front parallel to the leading edge (what has become known as the Sears gust). The airfoil is considered as a flat plate at zero angle of attack and therefore produces no disturbance to the uniform flow field. As a vortical disturbance convects past the airfoil an irrotational flow field is generated which satisfies the non-penetration condition on the surface. Also, vorticity is shed into the airfoil wake to maintain the Kutta condition at the trailing edge. This response characterizes the unsteady lift and moment experienced by the airfoil. Sears derived an explicit expression for lift and moment that involve a combination of Bessel functions which have become known as the Sears function.

Liepmann (1952) extends Sears theory to consider the case of airfoil encountering turbulence of scale much greater than the span and utilizes statistical concepts in development of the lift response. He formulates the mean C_L squared in terms of an admittance function (Sears functions) and the power spectrum of a sinusoidal gust. This method is extended by Liepmann (1955) to allow the usage of the frequency spectrum of the incoming turbulence. Specifically, he introduces a two-wavenumber spectrum (spanwise and streamwise) to describe the turbulence which allows consideration of the more practical situation wherein turbulence scale is smaller than the span. The sinusoidal variation in angle of attack along the span is accounted for by taking the section lift at each spanwise location to be given by the local angle of attack and the two-dimensional Sears function. Ribner (1956) furthers this statistical approach to allow consideration of the full, 3-wavenumber turbulence spectrum and three dimensional response function.

1.1.2 Approximate Analytic and Numeric Models

Unfortunately there exists no exact analytical solution for the more realistic case of a skewed (three dimensional), compressible gust. Therefore several approximate closed form and numerical solutions have been developed for slightly less complex situations with the goal of developing a rational and accurate three-dimensional, compressible model.

1.1.2.1 The Skewed Incompressible Gust

Ratcheting up the complexity researchers began to consider the somewhat more complex case of an incompressible, skewed gust. Filotas (1969) found a closed form expression for the problem of an infinite, thin airfoil encountering a skewed, incompressible gust at zero angle of attack and derived approximate expressions for the lift and pressure distribution. His results were later demonstrated to be rather crude. Graham (1970a) also considered the skewed gust case and formulated a relationship for the transfer function (airfoil response) based on Sears (1941) analysis. The analysis is rather cumbersome in nature based on the consideration of both streamwise and spanwise shedding of vorticity due to the varying angle of attack along the span. Graham provides the equations to numerically compute unsteady lift, chordwise pressure, and moment.

Mugridge (1970) provides a closed form expression for the lift response of a thin airfoil of finite span immersed in a convected skewed sinusoidal upwash. He also showed the interesting effect that as spanwise wavelength of the gust becomes small compared to the span cancellation of surface pressure fluctuations occurs everywhere except at the extreme edges of the airfoil span.

Amiet (1976a) developed a skewed gust incompressible solution valid at high reduced frequencies and large spanwise wave numbers from which the full compressible, skewed gust response can be derived. This work is extended by Amiet (1976b) to small spanwise wavenumbers utilizing Graham's (1970b) similarity rules with Amiet's (1974) compressible gust solution thus providing a solution to the complete spanwise wavenumber range.

1.1.2.2 The Compressible Parallel Gust

The interaction of turbulence with a lifting body and the noise produced are tied closely to the compressible nature of the free stream fluid. It is therefore critical to consider the effects of compressibility in the turbulence/airfoil interaction problem. Early consideration of this important effect has been given by Possio (1938) and Reissner (1951). Amiet (1974) modifies Miles (1950) solution to consider the case of a compressible two-dimensional gust problem and develops a closed form expression valid at low frequencies. Amiet (1976a) later derived a closed form expression for the two-dimensional, compressible upwash problem valid at high reduced frequency. He employed the first two steps of an iterative procedure given by Landahl in which the leading and trailing edge boundary conditions are alternately applied. For this reason the theory only applies to high frequencies when the acoustic wavelengths are not large compared to the chord.

Amiet (1975) also developed a relationship between the lift response function and turbulence spectrum which allowed prediction of far field acoustic radiation. In addition, he showed acoustic predictions can be made under certain conditions using only the unskewed gust response and limited information about the spanwise wavenumber content of the turbulence.

1.1.2.3 The Skewed Compressible Gust

Having developed solutions for the parallel, compressible and skewed, incompressible gusts researchers began to cast these problems in a somewhat hybrid manner allowing them to formulate approximate solutions to the more realistic case of a skewed, compressible gust. Graham (1970b) extends his work (although still computational in nature) to the case of a skewed, compressible gust encountering a flat plate at zero incidences. He transforms this problem into two sub-problems via a Prandtl-Glauert transformation depending on the spanwise trace speed of the gust along the airfoil leading edge. In the case of a subsonic trace speed the plate response is expressed in terms of the incompressible skewed gust problem which has been solved by Graham (1970a). For a supersonic trace speed the response is recast in terms of the unskewed, compressible gust which has been solved by Possio (1938).

Adamczyk and Brand (1972) formulated a closed form solution for the skewed compressible gust which allows calculation of far field noise. Adamcyzk (1974) wishing to more clearly define the unsteady pressure, lift and moment response developed an approximate theory to the compressible, skewed gust which compared favorably to the exact theory of Graham (1970b).

Chu and Widnall (1974) extend Amiet and Sears' (1970) GASP approximation to derive a similarity rule for the three-dimensional interaction of a two-dimensional wing and convected oblique sinusoidal gust in compressible flow valid at low reduce frequency. Osborne (1971) employed the GASP approximation to transform the Sears' two-dimensional, incompressible solution into one for compressible flow in a straightforward analytic form. Although, as pointed out by Amiet (1974) this method cannot be utilized for the case of a two-dimensional airfoil since the solution involves integration over the infinite span. Therefore, Sing and Widnall develop a similarity rule which is valid in the presence of an infinite span wing. This method coupled with either Sears' (1941) two-dimensional or Filotas' (1969) three-dimensional incompressible flow solutions can be used as the bases for construction of analytic expressions for unsteady lift.

A second order theory for the three-dimensional, compressible case was developed by Graham and Kullar (1977). These researchers used a general perturbation series to derive a second order solution for lift coefficient and compared their results with those of Amiet (1974) and other approximate solutions. They demonstrated insufficiencies in Amiet's solution as spanwise wavenumber tends to zero.

Martinez and Widnall (1980) unified aerodynamic/acoustic theory through the derivation of a closed form expression which couples the airfoil response with the acoustic field. Building on the work of Amiet (1976a) and Adamczyk (1974) they give a high frequency approximation to the airfoil response for a skewed, compressible gust from which both surface pressure fluctuations and far field noise can be determined. Their solution agrees with Adamczyk's (1974) for the case of zero sweep and collapses to Amiet (1976a) for the case of a parallel gust.

1.2 Increasing the Model Complexity: Effects of Angle of Attack and Thickness

The flat plate model provides well as a tool for understanding critical aspects of the turbulence airfoil interaction but, certainly the distortion effects produced by the mean flow field surrounding the airfoil and the shifting stagnation point with varying angle of attack must have important consequences on the interaction. Therefore, researchers aware of the deficiencies of the flat plate, zero incident interaction model began to investigate possible avenues for the incorporation of thickness and mean loading effects.

1.2.1 Heuristic Investigation of Angle of Attack Effects

Perhaps the earliest attempts to consider angle of attack was that of Horlock (1968) and later extended by Morfey (1970). These researchers present a method for determining the lift fluctuation of an airfoil at angle of attack due to a gust parallel to the uniform flow field. Combining this method with established theory for transverse gusts (perpendicular to undisturbed flow) Horlock arrives at the fluctuating lift produced by both gust types. In his formulation Horlock argues that unsteady lift fluctuations arise not just by upwash fluctuations (producing an instantaneous change in angle of attack) but also by the streamwise velocity fluctuations changing the scaling of the lift coefficient.

1.2.2 A Rational Model Considering the Effects of Distortion: Rapid Distortion Theory

Goldstein and Atassi (1976) were conceivably the first to consider the distortion of incoming turbulence in development of the airfoil response function. They employed the technique of Rapid Distortion Theory (RDT) which considers the distortion of an incoming vortical gust (tilting and stretching of vorticity vector) by the steady-state potential flow around the airfoil. They formulate a solution for the case of a two-dimensional, incompressible gust providing separate methods for calculating the effects of angle of attack, camber, and thickness on the unsteady lift response in terms of a correction to the Sears formula. Interestingly, they show the effect modeled by Horlock's theory is completely cancelled through a term arising from the distortion.

McKeough and Graham (1980) extended the RDT based prediction to the case of a skewed gust which they found to be consistent with Goldstein and Atassi's result for zero spanwise wavenumber. They determined that first order corrections to the zero angle of attack case arise from both distortion and the streamwise component of the velocity fluctuation. They also show that in the case of an airfoil immersed in homogenous isotropic turbulence these corrections cancel.

Atassi and Grzedzinski (1989) furthered the capability of RDT as an airfoil response prediction tool through the elimination of a key singularity arising from the infinite distortion of incoming vortical disturbances at the stagnation point. This singularity forms when applying RDT around a closed body, such as an airfoil and extends itself along the surface of the body at the exact location where the airfoil response is desired. Atassi and Grzedzinski showed that the irrotational field generated by the response of the airfoil must contain a canceling singular behavior and thus proposed a three way split of the fluctuating velocity field that accomplished this. Although greatly extending the capabilities of RDT in prediction of the airfoil response Atassi and Grzedzinski's method is a numerical procedure and their solution only considers the response at a few discrete frequencies.

Scott and Atassi (1995) building on Scott (1990) extended the Atassi and Grezedzinski approach to a numerical method for solving subsonic flows with convected, three-dimensional vortical waves around a lifting airfoil. Their approach offers the computational efficiency of potential flow methods while accounting for the convection and distortion of incoming vortical disturbances by the mean flow field surrounding the airfoil. They compare their numerical solution of lift response to the Sears function and solutions of Possio's integral equation investigating the effects of thickness, camber and angle of attack at particular wavenumber frequencies. In general, they find that thickness becomes important at higher frequencies. They also showed that for small angles of attack (~1°) a reduction in unsteady lift occurs at low frequencies.

1.3 Experimental Studies of Turbulence/Airfoil Interaction

Comparatively few experimental studies have complimented the development of airfoil response theories. Those that have been performed usually consist of measurements at a few discrete frequencies or measurement locations providing a crude representation of the airfoil response function.

Jackson, Graham and Maull (1973) measured the lift spectrum on a NACA 0015 in grid generated turbulence (L/c = 0.417) at a Reynolds number (based on chord) of 16000 and compared the admittance function with two-dimensional Sears based on Liepmann's (1952, 1955) two-dimensional theory and his strip theory. They found good agreement with Graham's (1970a) three-dimensional theory while two-dimensional and strip theory overpredicted by an order of magnitude and 50% respectively. Also, the measured admittance increases above the three-dimensional theory at low frequencies the reason for which the authors believe is related to the distortion of incoming turbulence which acts to enhance lift.

Commerford and Carta (1970, 1973) investigated unsteady pressure at 5 chordwise locations on a 5% thick circular arc airfoil immersed in a circular cylinder wake at a chord Reynolds number of 400000. The cylinder wake produced a sinusoidal, two-dimensional upwash gust with a reduced frequency of 3.9. They found reasonable agreement at low angles of attack with the Sears function although noted that the phase angle variation of chordwise pressure was not well predicted.

An experimental study of a circular arc airfoil immersed in a periodic wake generated by a pinwheel was performed by Fujita and Kovasznay (1974). Pressure measurements were made and compared to Meyer's theory (thin airfoil theory) for varying angles of attack in the time domain. They show reasonable agreement between experiment and theory for unstalled angles of attack.

Patterson and Amiet (1976a, 1976b) performed one of the few systematic unsteady pressure measurements which allow unambiguous comparison with theoretical developments. A NACA 0012 was immersed in grid generated turbulence of von Karman like spectrum (L/c = 0.13) and the unsteady pressure measured between 15 and 70% chord through embedded transducers. They also measured radiated noise level with microphones located outside of the wind tunnel jet. One transducer on the airfoil could be moved in the spanwise direction allowing measurement of the spanwise correlation. Measurements were performed at 4 speeds between 40 and 120m/s. They showed reasonable agreement between measured surface pressure spectra and correlations and Amiet's (1976a) high frequency prediction at zero angle of attack. Amiet's (1975) far field predictions also agreed well with far field measurements. These researchers also show an increase in radiated noise when the angle of attack is set to 8° and report (although do not show) an increase in surface pressure fluctuations which is small but measurable.

McKeough and Graham (1980), using a configuration similar to Jackson *et al.* complimented their RDT prediction with unsteady lift measurements on a NACA 0015 at 0° and 10° angle of attack immersed in grid generated turbulence (L/c =0.4, turbulence intensity = 5.8%). Unsteady lift measurements were also made at 0° angle of attack in lower turbulence intensity flow (L/c = 0.38, turbulence intensity = 3.7%). They showed as much as a factor of 2 increase in mean-squared lift fluctuation at low reduced frequencies (<1) and argued that this must be a second order effect due to the canceling of first order effects arising from the distortion and the streamwise component of the velocity fluctuation in the case of isotropic, homogenous turbulence.

Williams and Harris (1984) measured far field noise radiated by a helicopter rotor operating in grid and wake generated turbulence. These researchers uncovered an increase in peak SPL of broadband radiated noise with increasing mean loading. Also demonstrated was a greater rate of increase when the rotor is subject to lower turbulence levels which Williams and Harris feel is related to the distortion of the turbulence encountering the lifting airfoil.

Additional experimental measurements have been made in the specific case of a cascade of blades encountering turbulence. These measurements, although not as general as a single airfoil immersed in turbulent flow still serve well to reveal the underlying physics governing the airfoil/turbulence interaction. Satyanarayana, Henderson, and Gostelow (1974) measured unsteady pressure on a cascade of blades immersed in a transverse gust flow at reduced frequencies between 0.01 and 0.102. These researchers note a strong dependence of the airfoil response on Reynolds number and boundary layer behavior. Fleeter, Capece, and Chiang (1989) investigated the unsteady aerodynamic response using an axial compressor configuration with varying angle of attack. They show a significant effect on the unsteady response with increasing mean loading.

1.4 Motivation for Current Study

Given the number of turbulence/airfoil interaction models and variations which exists there have been comparatively few experimental studies aimed at verifying the accuracy of these models or highlighting real airfoil effects (i.e. thickness, angle of attack). Also, few test have been performed which consider the effects of turbulence scale or intensity on the airfoil response. Therefore, it is the aim of this research to clarify the effects of mean loading in the presence of two turbulence scale flows. Additionally, a comparison of experimental results with Amiet's (1976a,b) theory is presented. Specifically, the goals of this work are to show:

1 The turbulence/airfoil interaction dependence on turbulence scale in the presence of mean loading.
2 The airfoils finite thickness effects as compared to the flat plate model.
3 Mean loading and turbulence scale effects on the correlations in the spanwise and chordwise direction.

These goals are met through the immersion of an instrumented NACA 0015 in two homogenous, isotropic grid generated turbulent flows. The airfoil is equipped with 96 surface pressure-sensing devices distributed across the span and chord allowing nearly complete measurement of the unsteady surface pressure response.

Chapter 2. Apparatus and Instrumentation

2.1 Wind Tunnel

All measurements were performed in the Virginia Tech Stability Wind Tunnel. The tunnel is a continuous, closed jet, single return, subsonic wind tunnel with a 6'x6' test section 24 feet in length. The general design layout is in Figure 2.1.

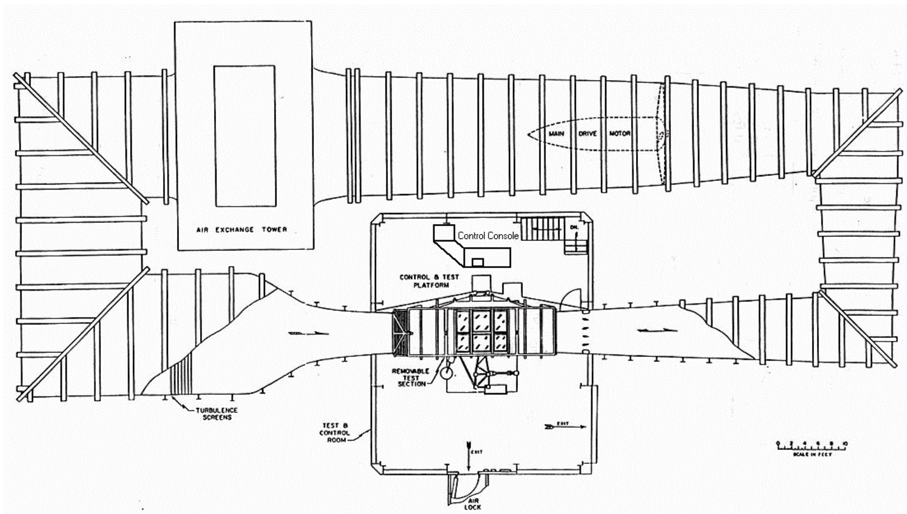

Figure 2.1: Virginia Tech Stability Wind Tunnel

The tunnel is powered by a 600hp DC motor driving a 14 foot propeller providing to a maximum speed of about 60m/s. Tunnel speed is regulated by a custom designed Emerson VIP ES-6600 SCR Drive. Turbulence levels in the test section are extremely low, on the order of .05% or less, and flow in the empty test section is closely uniform (see Choi and Simpson, 1987). Although not originally designed as a low turbulence facility, the addition by the NACA of seven anti-turbulence screens, coupled with the other flow smoothing features of the tunnel, resulted in very low turbulence levels. The test section dynamic pressure is measured with a reference pitot-static probe located 3.5” downstream of the test section entrance.

Acoustic noise levels in the empty wind tunnel are surprisingly low and appear dominated by broadband noise from turbulence ingested into the drive propeller. The characteristics of this noise has been documented by Larssen and Devenport (1999) and is presented for the flow conditions (30 m/s) of the current test in figure 2.2. Acoustic noise levels were measured with a Bruel and Kjaer microphone fitted with a nose cone. The wind generated noise associated with this nose cone has not clearly been identified and therefore can not be subtracted out of the tunnel acoustic measurements. Thus, this measurement is a conservative estimate of the acoustic field within the test section and can be considered to represent the upper bound.

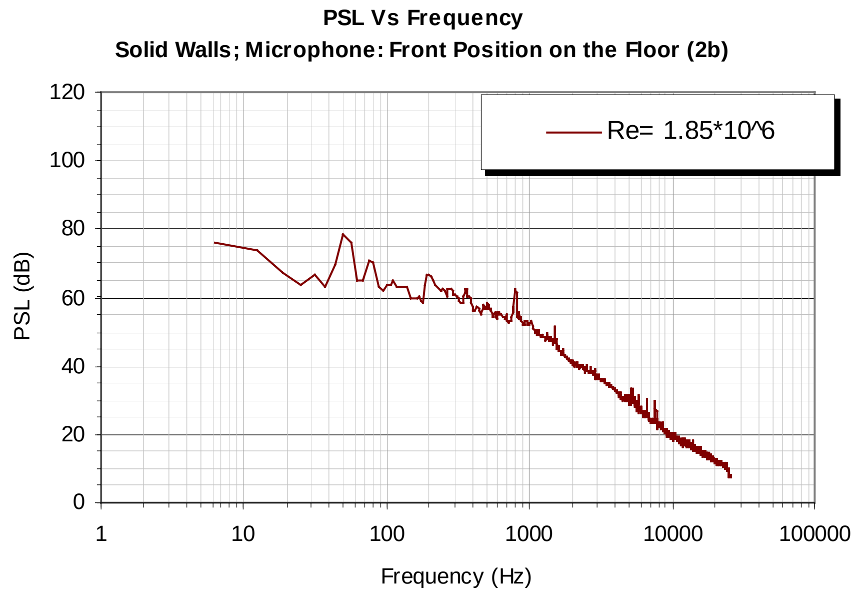

Figure 2.2: Pressure sound level at 30 m/s

Two grids have been developed for the Virginia Tech 6' x 6' Stability wind tunnel for the purpose of generating homogeneous isotropic turbulent flows for the study of unsteady airfoil response. The characteristics of each grid generated flow has been reported by Bereketab, *et al*. 2000 and is summarized here. The first, a square bi-planar grid with a 12" mesh size and an open area ratio of 69.4%, was mounted in the wind tunnel contraction 19.1 mesh sizes upstream of the location planned for the airfoil leading edge, at a point where the cross-sectional area was 32% larger than that of the test section (figure 2.3).

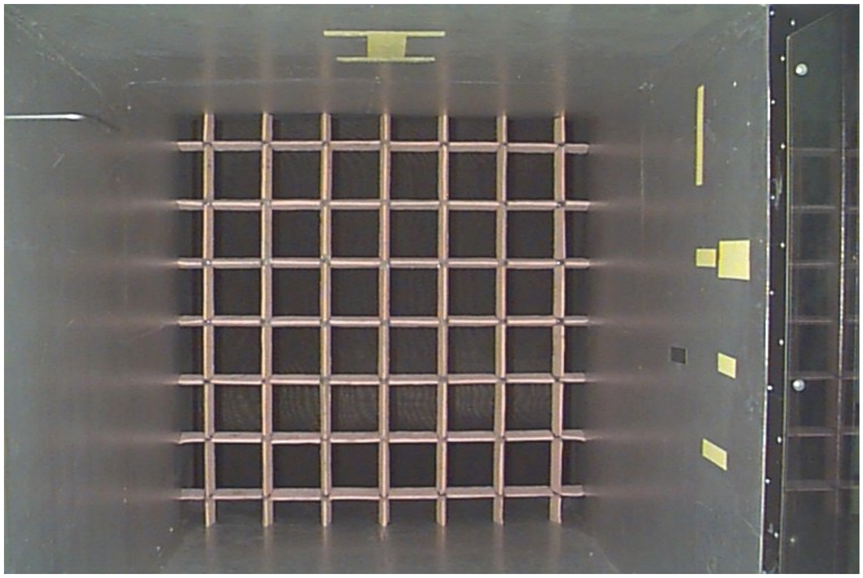

Figure 2.3: Downstream view of large grid

Acoustic foam wedges attached to the downstream side of the grid were used to minimize grid generated noise. The second grid, a metal weave with a 1.2" mesh size and an open area ratio of 68.2% was mounted in the tunnel test section at a position 16.1 mesh sizes upstream of the planned leading edge location (figure 2.4). It should be noted that the small grid is located downstream of the tunnel reference pitot-static probe which requires a correction of the pressure lose across the grid when used as a reference for mean pressure measurements on the surface of the test airfoil.

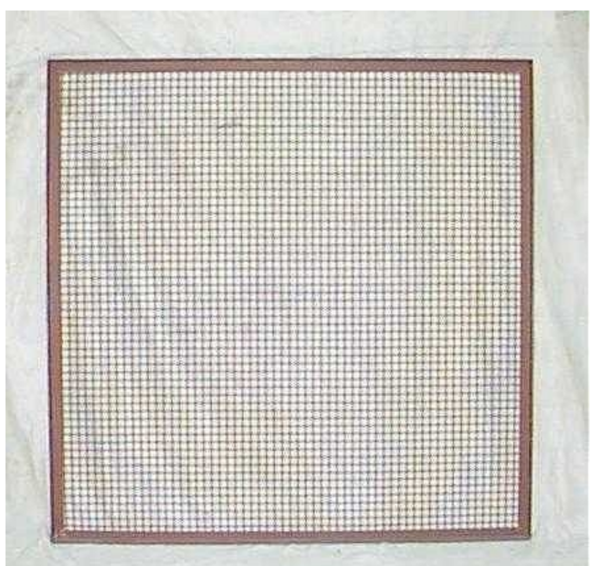

Figure 2.4: View of small grid

Table 2.1 summarizes flow speed and Reynolds number data for each grid as well as Reynolds number based on the chord of the NACA 0015 airfoil used in the subsequent surface pressure measurements.

Table 2.1: Flow speed and Reynolds number

Nominal Flow Speed (m/s)	Small Grid Re	Large Grid Re	Equivalent airfoil chord Re
30	63370	632982	983226

Three-component velocity and turbulence measurements were made with 4-sensor hot-wire probes over a 24"x24" cross section centered on the tunnel centerline in order to reveal the form of the grid generated flows. Turbulence intensities produced by the large grid are between 3% and 4% at all speeds and in all components as shown in figure 2.5.

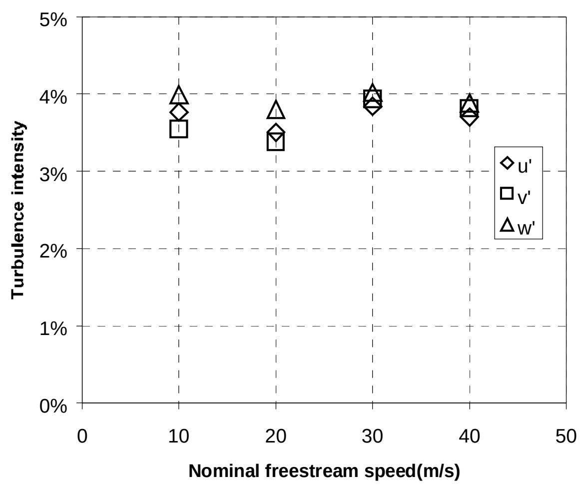

Figure 2.5: Cross-sectional averaged turbulence intensities for large grid flow

Turbulence intensities produced by the small grid are between 3.5% and 5% at all speeds and in all components as demonstrated in figure 2.6.

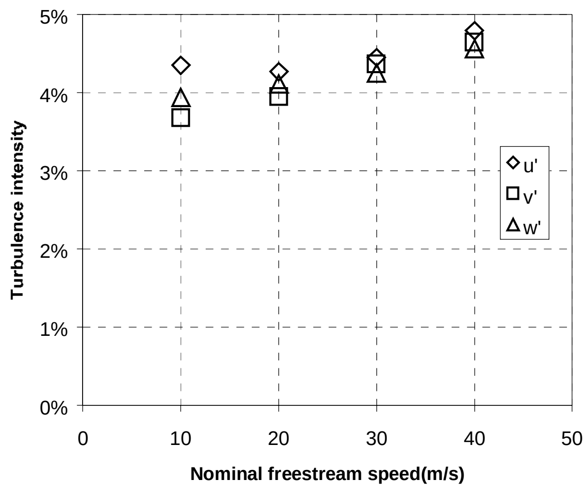

Figure 2.6: Cross-sectional averaged turbulence intensities for small grid flow

The isotropy of the turbulence components in the large grid flow appears best at 30m/s where the difference between the smallest and largest components is less than 5% of the measured intensity as revealed by turbulence stress contours in figure 2.7.

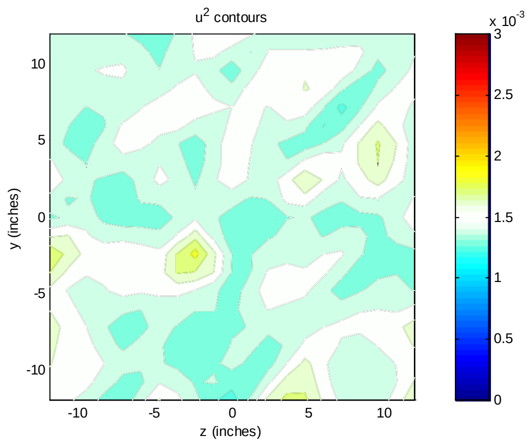

Figure 2.7 (a): Large grid flow contours of u-component turbulence normal stress normalized on U_∞^2

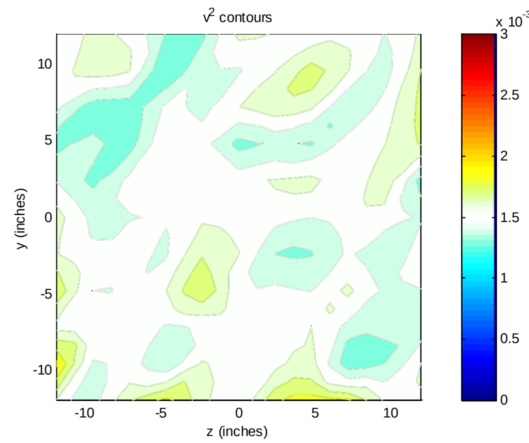

Figure 2.7 (b): Large grid flow contours of v-component turbulence normal stress normalized on U_∞^2

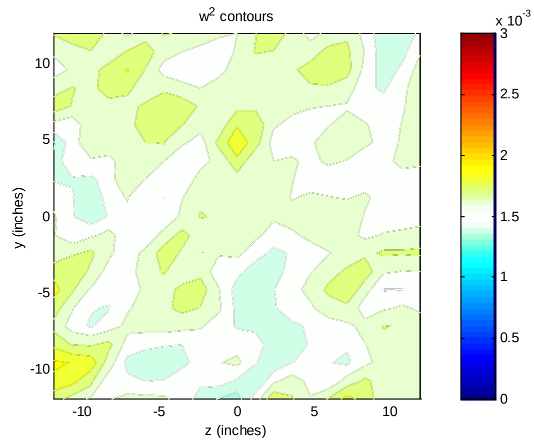

Figure 2.7 (c): Large grid flow contours of w-component turbulence normal stress normalized on U_∞^2

The variation in turbulence stress level appears to be random and within the uncertainty of the measurement. The turbulence stress field is closely homogeneous as well.

The isotropy of the turbulence, as shown in figure 2.8 appears very good at 30m/s in small grid flow, the difference between the smallest and largest components at 30m/s being less than 1 part in 20.

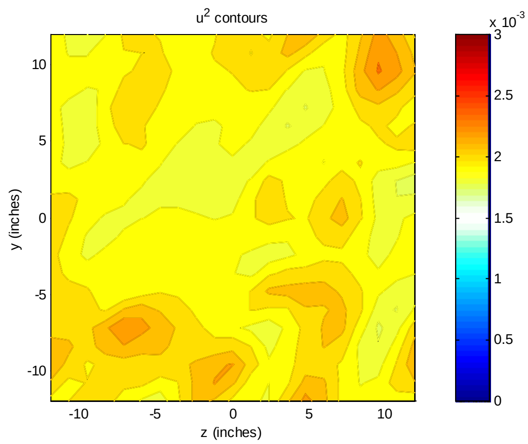

Figure 2.8 (a): Small grid flow contours of u-component turbulence normal stress normalized on U_∞^2

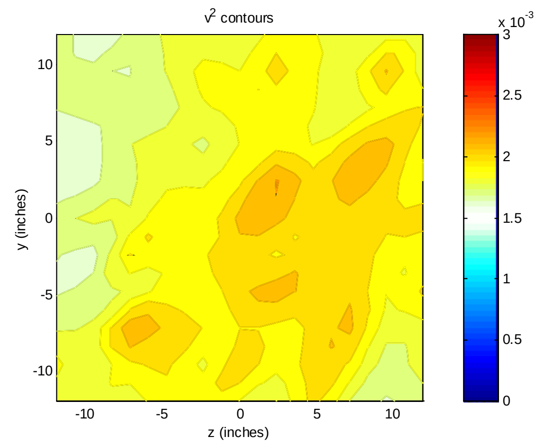

Figure 2.8 (b): Small grid flow contours of v-component turbulence normal stress normalized on U_∞^2

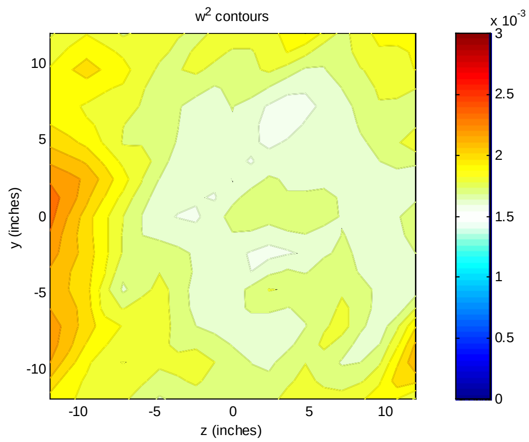

Figure 2.8 (c): Small grid flow contours of w-component turbulence normal stress normalized on U_∞^2

The turbulence stress field shows some slight in-homogeneities at all flow speeds, attributed to a slight bow in this grid (about 0.4" at the grid center in the downstream direction), and the blockage produced by the frame used to support it.

Table 2.2 presents the inferred integral length scale for each grid at 30m/s.

Table 2.2: Longitudinal integral scales (L) and velocity scales (u') that best describe the 2 grid turbulence flows.

	Large grid	Small Grid
u'/U_∞ (%)	3.93%	4.35%
L (in.)	3.22	0.309

As reported in Bereketab, *et al* (2001) for wavenumbers below the upper limit of the inertial subrange, the spectra and correlations measured with both grids can be represented using the von Karman interpolation formula with a single velocity and length scale. The spectra may be accurately represented over the entire wavenumber range by a modification of the von Karman interpolation formula that includes the effects of dissipation.

2.2 Airfoil Model

Surface pressure measurements are made on an instrumented NACA 0015 with chord length of 2-ft and 6-ft span manufactured by Sandia National Labs. The airfoil trailing edge is round with a radius of curvature of 0.1075". Measurement of the airfoil geometry confirms the 0015 shape which is calculated based on

$$\frac{z}{c}=\frac{0.15}{0.2}\cdot\left(0.2969\cdot\frac{x}{c}\right)^{1/2}-0.126\cdot\frac{x}{c}-0.3516\cdot\left(\frac{x}{c}\right)^{2}+0.2843\cdot\left(\frac{x}{c}\right)^{3}-0.1015\cdot\left(\frac{x}{c}\right)^{4}. \tag{2.1}$$

Figure 2.9 presents the measured geometry plotted with the exact (analytically calculated) geometry.

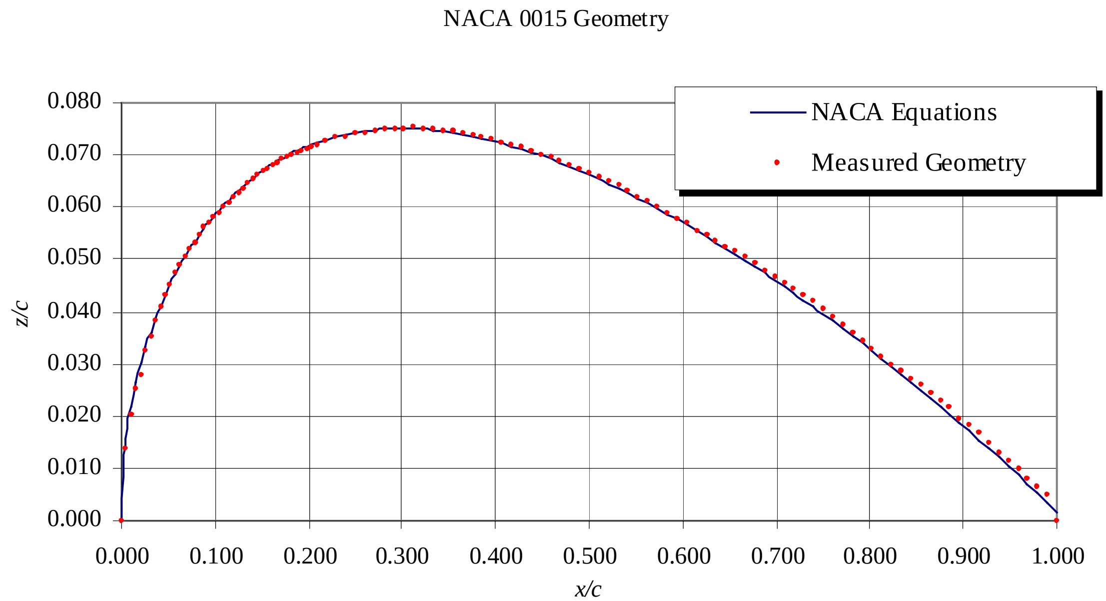

Figure 2.9: NACA 0015 measured and calculated geometry

Minor imperfections are present on the surface of the airfoil consisting of scratches approximately 1/32” deep and ½” to 1” long. These imperfections are located primarily out of the measurement region and cover less then 0.1% of the total surface.

The airfoil model is equipped with a removable access hatch which is 2-ft in span, the length of the chord and half the thickness of the airfoil. The hatch is positioned mid-span. Figure 2.10 reveals the airfoil with hatch removed.

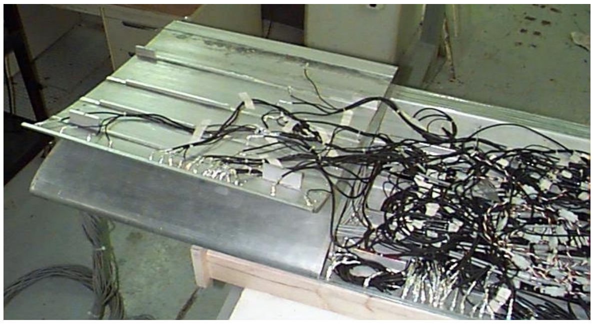

Figure 2.10: Wing with hatch removed

The hatch is placed over the access and shimmed internally to ensure a smooth transition from the hatch surface to the wing. Four bolts are used to fasten the hatch to the airfoil. The hatch is then sealed with 0.00275” clear tape along both sides and the leading and trailing edge. Wax is then used to blend the tape into the surface of the airfoil.

Mean pressure measurements are made with a 48 port scani-valve system. The scani-valve is connected and pressure measured with a Honeywell Model DRAL520GN pressure transducer interfaced with an IBM/AT computer through a data translation DT2801-A A/D converter. 3mm Tygon tubing is used to traverse the distance between the scani-valve and the interior of the wing. 0.075” OD copper tubing is used to transition the Tygon tubing from the inner surface of the wing to the outer surface. Measurement points are located 2” down from the hatch in a chordwise plane exactly perpendicular to the leading edge. Figure 2.11 shows the chordwise location of the pressure ports.

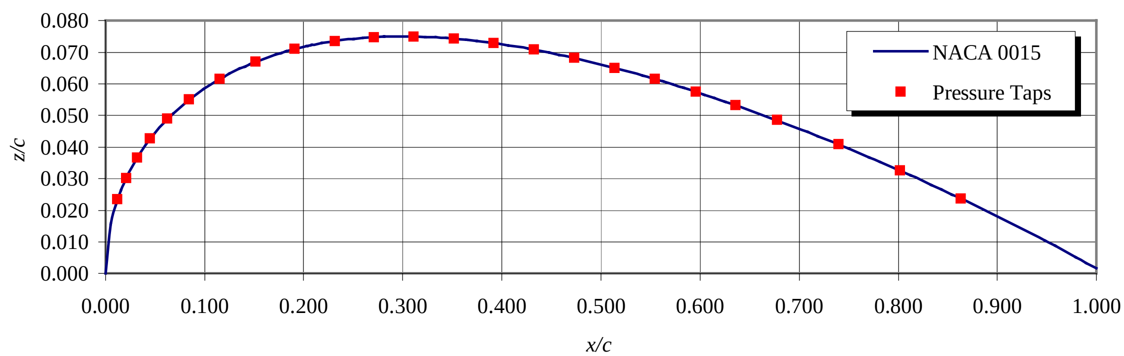

Figure 2.11: Chordwise distribution of mean pressure taps

Mounting of the airfoil model is done to allow rotation of the model about the quarter chord for angle of attack adjustment. Two 4.6” outer diameter (3.75” ID) aluminum pipes protrude from both ends of the airfoil and are bolted to the models internal structure centered at the quarter chord. The pipes then slip through holes in the tunnel roof and floor plating. The pipe protruding through the tunnel roof then slides through a mounting block (Figure 2.12) which allows adjustment of the yaw and rolling angle.

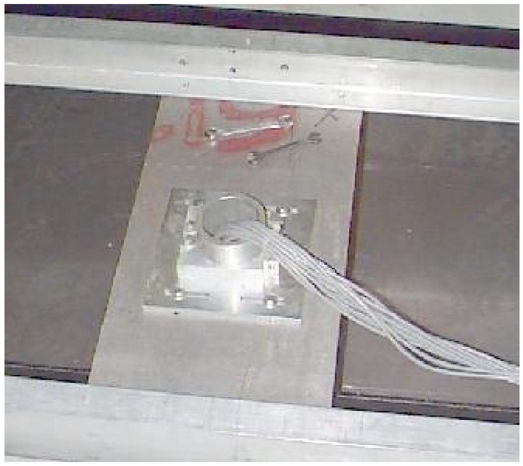

Figure 2.12: Roof mounting block

Finally, the roof pipe is clamped to the mounting block (Figure 2.13) and the floor pipe is clamped to the floor plate.

Figure 2.13: Roof mounting structure

Angle of attack adjustments are made by loosening the clamps and rotating the wing.

Angle of attack is determined by setting the trailing edge to angle of attack markings on the wind tunnel floor. The angle of attack setting is also verified using the mean pressure data plotted with the potential flow solution.

The airfoil model leading edge is located 229.2” (9.6 chords) downstream of the large grid and 19.32” (0.805 chords) downstream of the small grid as shown in figure 2.14.

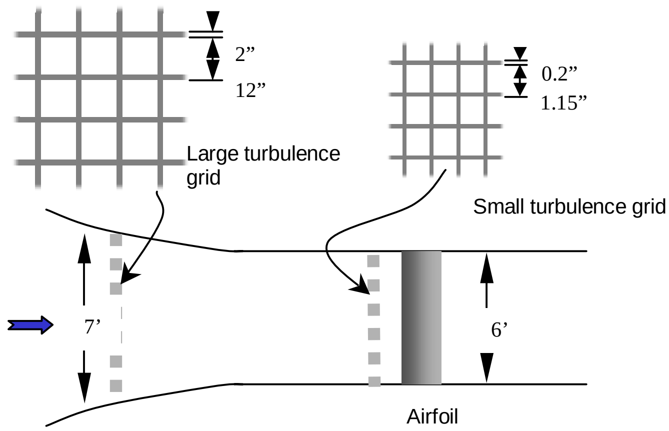

Figure 2.14: Schematic of the wind tunnel contraction and test section showing the locations of the grid and airfoil model.

Turbulence length scales normalized on chord and leading edge radius are presented in table 2.3.

Table 2.3: Turbulence length scales normalized on chord and leading edge radius

	Large grid	Small Grid
L/c	0.134	0.0129
L/r_c	5.41	0.519

Preliminary testing demonstrated insufficient need for a model trip strip. In fact laminar flow is preferred due to the signal contamination associated with turbulent boundary layer pressure fluctuations. The boundary layer was found to transition at a similar chordwise location across the span.

2.3 Microphone System

The airfoil model is instrumented with a unique multiple-microphone system. The system, illustrated schematically in figure 2.15, consists of 96 Sennheiser KE 4-211-2 microphones.

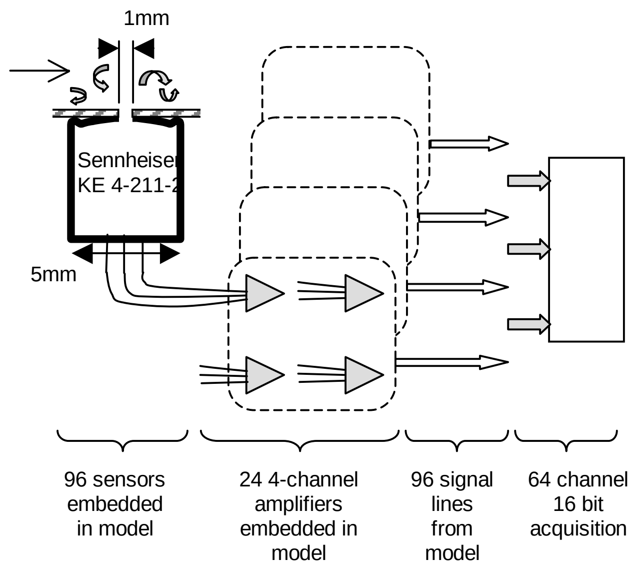

Figure 2.15: Schematic of microphone system

These microphones are sensitive (10mV/Pa), provide low noise signals and a nominal response that is flat to within 1dB from 40Hz to 10000Hz, calibratable over a larger range. The microphones are built with a 1mm pinhole (providing reasonable spatial resolution) which can be recessed a short distance (typically 0.5mm) below the airfoil surface without significantly degrading the response. They can measure signals up to an SPL of 125dB and are insensitive to vibration. Their small physical size allows a minimum sensor spacing of about 5mm (significantly less than the expected correlation length scales). We have built independent operating electronics and amplifier circuitry for each microphone using a compact modular approach that enables these systems to be embedded in the model close to the microphone locations. The system is powered by 6 custom-built quiet power supplies. It is operated, and measurements are made using a Hewlett Packard E1432 based data acquisition system. This system (which is expandable) provides simultaneous measurement of 64 channels with 16 bit accuracy at sampling rates up to 56kHz per channel, and has built in anti-alias filtering for each channel. It is important to note that this system is not limited to a 64-point measurement of the two-point surface pressure correlation function. Because of the spanwise homogeneity of a mean two-dimensional flow the 64-channel/96 microphone system can be positioned and manipulated to behave as a dense two dimensional array of 240 microphones. To understand how consider the actual microphone layout shown in figure 2.16.

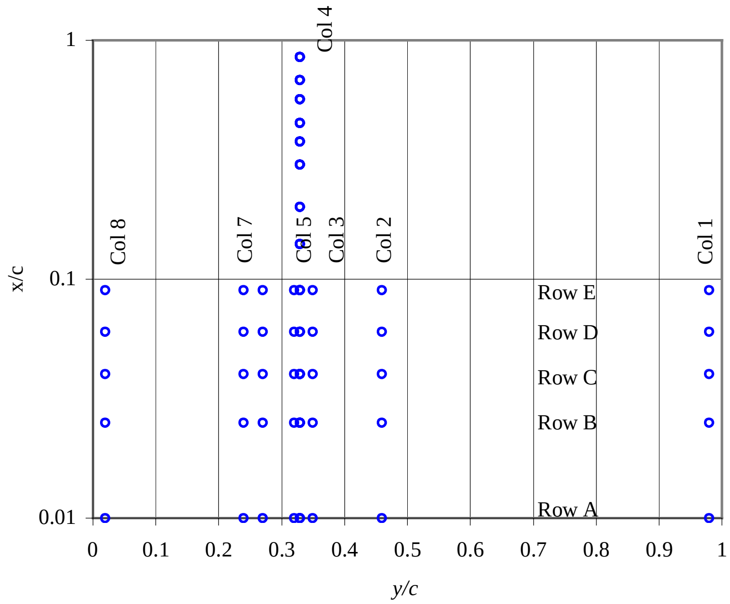

Figure 2.16: Microphone layout

Coordinate *x* in this figure refers to distance downstream from the leading edge, and *z* to distance along the leading edge from the hatch edge. Microphones are located on *both* sides of the airfoil at the locations indicated. At first sight the microphone array appears very sparse in the spanwise direction, but this is deceptive. Since the flow is homogeneous in the *z* direction the absolute position of the sensors in this direction is irrelevant, and the two-point space-time correlation is only a function of their spanwise separation (the array defines many more spanwise separations than it does positions). The following is an example measurement strategy with this array

- Simultaneously measure signals from all microphones in column 4, A1-A8, and B1-B8
- Repeat measurement except with row C, D, E
- Because of spanwise homogeneity, this produces *at least* the same two-point correlation/spectral data as would be obtained from a simultaneous measurement using 240 microphones in the 2D array shown in figure 2.17 (i.e. correlation of every point pivoted about every point). Furthermore the data set includes checks on the homogeneity assumed.

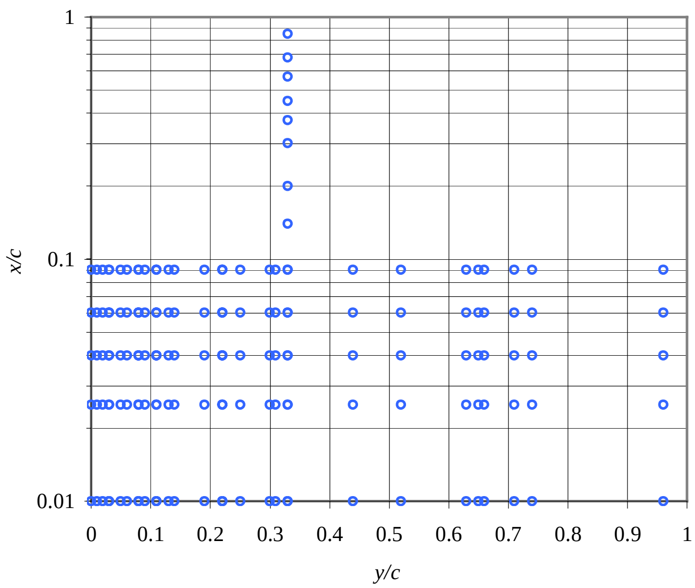

Figure 2.17: Effective microphone array

A central component of any such measurement system is a reliable means for calibrating the microphones. For accurate measurement of the space-time correlation one needs not just amplitude, but full phase vs. frequency calibrations for each microphone sensor. For this purpose we have built a calibrator shown schematically in figure 2.18, adapted from a NASA design.

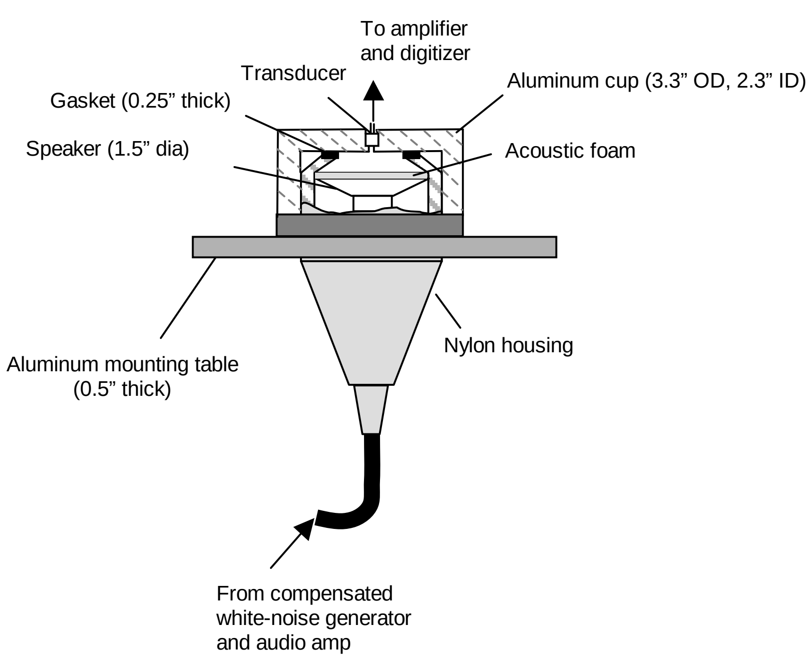

Figure 2.18: Microphone Calibrator

The calibrator consists of a small wide-range loudspeaker mounted on one side of a shallow cavity built into the end of a Nylon housing. The Nylon housing is fixed into a heavy aluminum plate with the open end of the housing extending 2 inches above the plate. The perimeter of the open end of the housing is lined with a rubber gasket that seals the cavity formed by an aluminum cup, which slides over the Nylon housing. Each microphone is placed in a recessed hole on the top of the aluminum cup, which is of similar dimension as those in the wing. The speaker system is driven from an audio amplifier using a white noise signal, compensated for the response of the speaker/amplifier system, generated by the HPE1432A. The cross spectrum between the input signal and microphone signal is then compared with a similar measurement made using the B&K reference microphone. The calibration is shown schematically in figure 2.19 where $V_1(t)$ is the white noise signal generated by the HP1432 (and also, simultaneously measured by the HP1432), P(t) is the pressure signal produced by the speaker signal, and $V_2(t)$ is the voltage signal produced by the microphone which is feed back to the HP1432 for measurement.

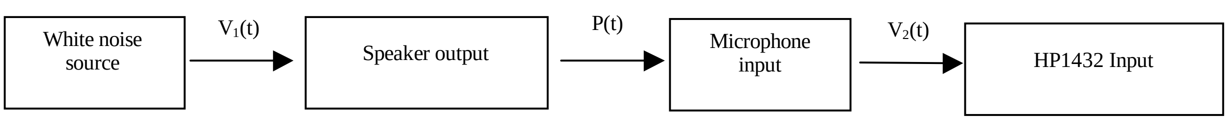

Figure 2.19: Microphone calibration schematic

The Sennheiser microphone response is obtained in the following manner: First, the speaker response, *S(ω)* [Pa/V] is determined using the Bruel and Kjaer reference microphone which has a known response, *bk(ω)* (0.803 V/Pa). This measurement in indicated as superscript *a*,

$$S(\omega)=E\left[\frac{V_2(\omega)}{bk(\omega)}\cdot V_1^*(\omega)\right]\Big/E\left[V_1(\omega)\cdot V_1^*(\omega)\right]=\frac{G^a_{PV_1}}{G^a_{V_1V_1}}\quad \text{[Pa/V]} \tag{2.2}$$

where *E*[] is the expected value. The Sennheiser microphone response is then found in a subsequent measurement (indicated as superscript *b*) as

$$M(\omega)=\frac{E\left[V_2(\omega)\cdot V_1^*(\omega)\right]}{E\left[V_1(\omega)\cdot V_1(\omega)\right]}\cdot\frac{1}{S(\omega)}=\frac{G^b_{V_2V_1}}{G^b_{V_1V_1}}\cdot\frac{G^a_{V_1V_1}}{G^a_{PV_1}}\quad \text{[V/Pa]} \tag{2.3}$$

With this system a phase and amplitude calibration over the full frequency range of a microphone can be performed in less than 1 minute. Calibration and pressure measurements were performed at high (12.8kHz) and low (1.6kHz) sampling rates resulting in adequate frequency resolution across the measurement range. A typical calibration performed in this manner is illustrated in figure 2.20.

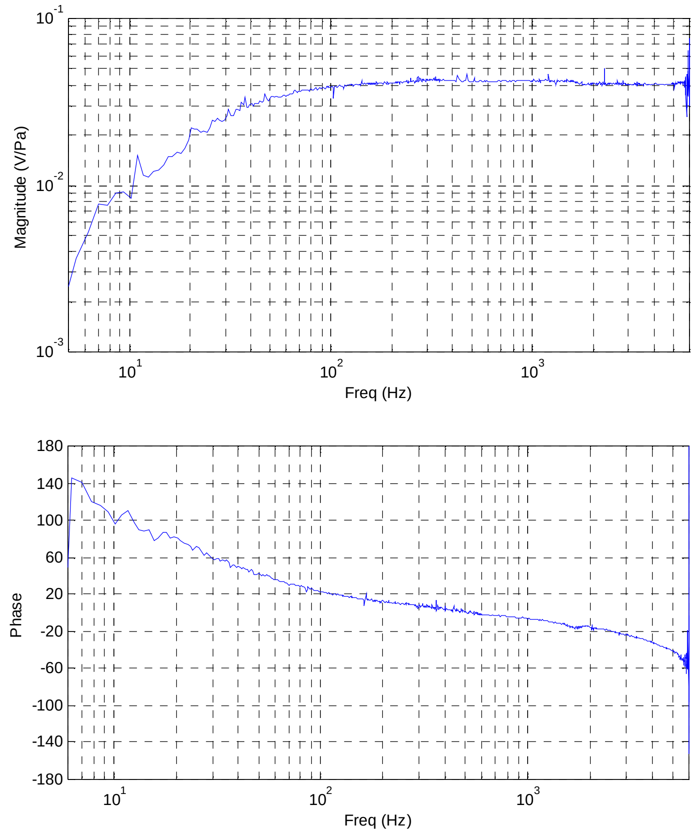

Figure 2.20: Typical magnitude and phase calibrations

The calibrator design was the result of an evolving process to achieve accurate and repeatable magnitude and phase calibrations. The initial calibrator design was handheld in nature allowing for calibration of each microphone while mounted in the wing. This design suffered from several flaws although primarily failing due to unreliable sealing between the calibrator and airfoil surface, particularly in the highly curved leading edge region, and the inability to consistently gather repeatable calibrations. Through further experimentation the Sennheiser microphone calibrations were shown to be unaffected by temperature variations within 70°F ±5°F. Furthermore, the calibrations show little (within the uncertainty of the calibration) drift with time.

The 96 microphones are configured in the wing as shown in figure 2.17 (note that figure 2.17 shows only one side of the airfoil, as each side is a mirror image of the other). Each microphone is mounted from within the airfoil in a slightly larger diameter hole than the microphone. The hole is bored to within 0.5mm of the outer surface of the airfoil. A pin hole is drilled in the center of the bored hole and aligns with the microphone pin hole. A typical cross-section through a microphone and microphone mounting hole is shown in figure 2.21.

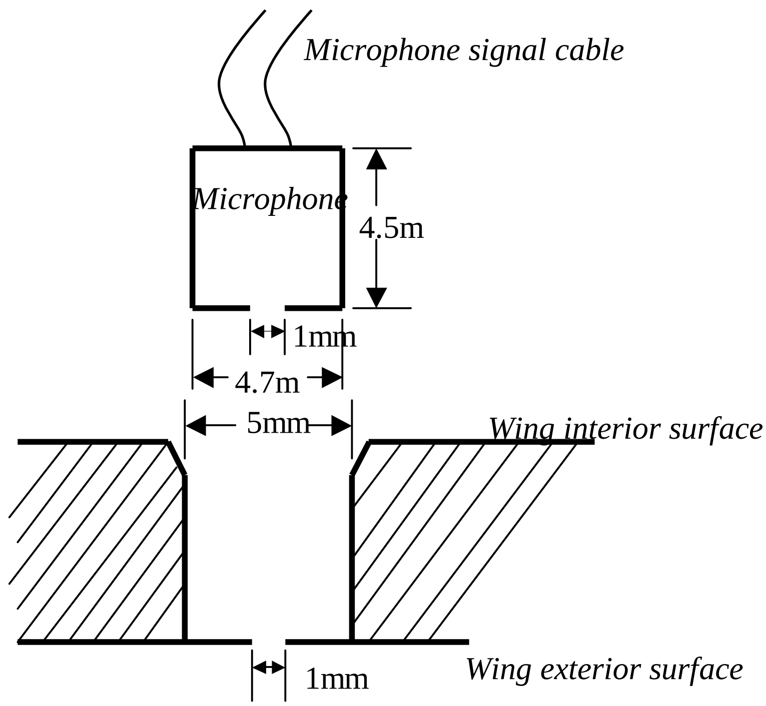

Figure 2.21: Cross-section through typical microphone and microphone mounting hole

Figure 2.22 shows a microphone lying beside a mounting hole on the interior of the wing.

Figure 2.22: Microphone lying beside mounting hole on interior of wing

The microphone is sealed and held in place with hot glue applied to the outer edge of the bored hole.

As stated above, operating electronics are embedded in the wing below and beside the access hatch. Power is supplied to the electronics through 6 power cables which exit the airfoil through the lower (tunnel floor) mounting pipe. Data from each microphone exits the wing on 24 data cables via the upper (tunnel roof) mounting pipe. This configuration which ensures minimal data contamination from the power supplies and cables is shown in figure 2.23.

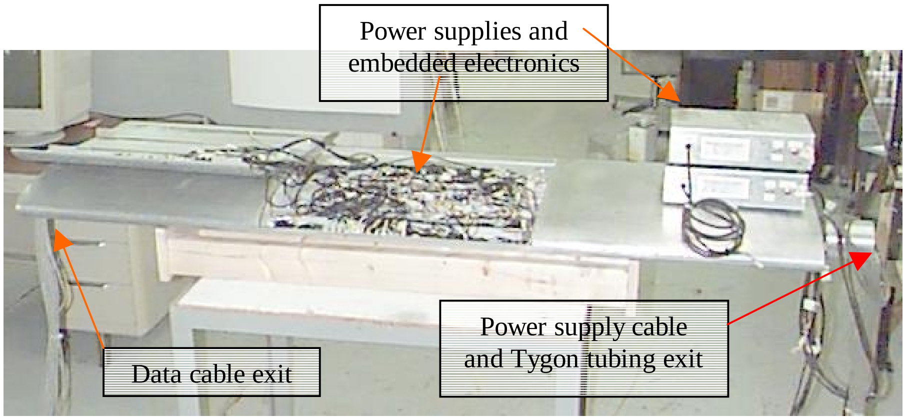

Figure 2.23: Data and power cabling configuration

2.4 Reference Acoustic System

Measurement of the tunnel test section acoustic field was performed simultaneously with some measurements of unsteady pressure. A Bruel and Kjaer model 4138 (figure 2.24) microphone mounted on an aerodynamic stand with microphone tip in the same plane as the wing leading edge was used (Figure 2.25).

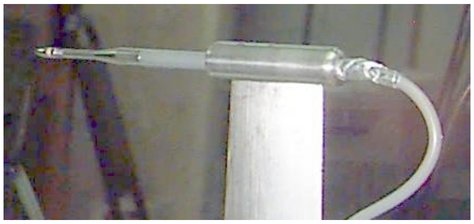

Figure 2.24: Bruel and Kjaer model 4138 reference microphone

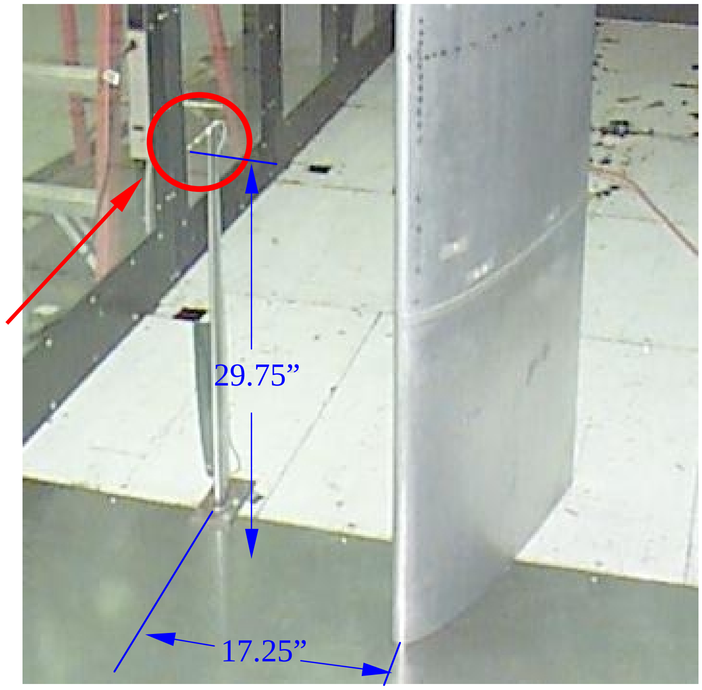

Figure 2.25: Overview of reference microphone mounted on stand next to wing

The microphone was located 17.25” to the starboard side of the airfoil chord line as measured at 0° angle of attack and 18.25” from the starboard test section wall at a height of 29.75”.

The reference microphone signal is conditioned and amplified and data then recorded by the HP1432 while simultaneously recording unsteady pressure as measured by the Sennheiser microphones. As mentioned previously, this microphone is equipped with an aerodynamic wind screen which serves to protect the microphone diaphragm. The noise induced by this wind screen has not been undoubtedly identified and thus the acoustic levels measured will represent an upper threshold of the acoustic field present in the tunnel test section.

2.5 Hot-wire Anemometry

For some measurements a hot-wire probe was mounted just off the airfoil surface at the 14% chord location. The goal of such measurement was to reveal the velocity/pressure correlation of the flow occurring around the airfoil and through interpretation infer the nature of the eddy convection and deformation.

Velocity measurements were made using a single sensor hot-wire probe (figure 2.26).

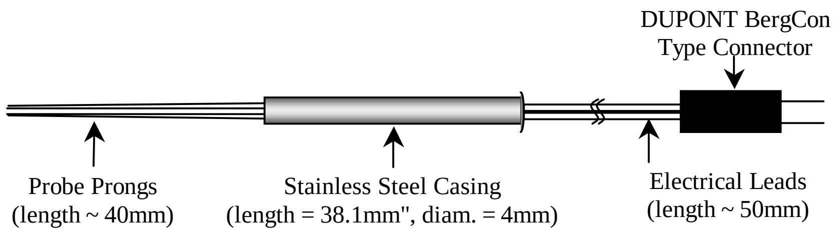

Figure 2.26: Diagram of hot-wire probe

The tip of the probe consists of two stainless steel tapered prongs that hold the sensor wire 40 mm upstream of the main body of the probe. The sensor wire is 0.8 mm in diameter and 5mm in length. The hot-wire is operated with a Dantec 56C17 bridge and a Dantec 56C01 constant temperature anemometer unit. The amplified signal is then recorded simultaneously with pressure measurements by the HP1432E.

Velocity measurements were made 0.875 inches off the surface of the airfoil exactly above a microphone located at 14% chord and 33% span (y/c = 0.33, figure 2.16) for all angles of attack including negative angles of attack. The mounting location was chosen to minimize interference associated with the probe and probe mount wake with unsteady pressure measurements. The hot-wire will allow examination of pressure/velocity correlations on both the suction and pressure side of the blade. The probe is held with epoxy to a small aluminum mounting bracket. The mount bottom is bent at a 90° angle to form a flange which is then epoxied to the surface of the airfoil as displayed in figure 2.27.

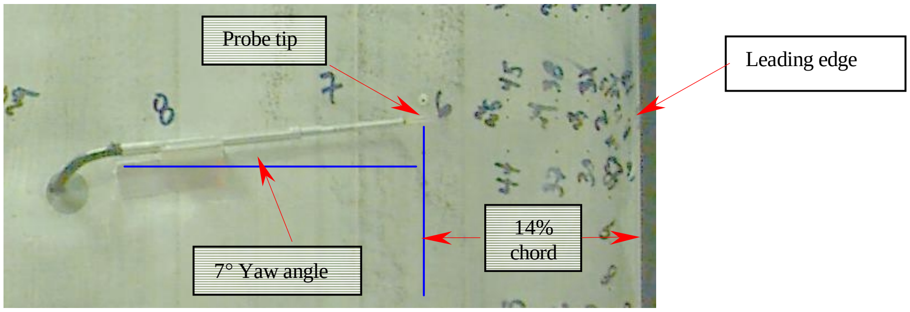

Figure 2.27: View looking down on mounted hot-wire

The mounted probe is yawed 7° to minimize the possibility of the mount wake contaminating the pressure field over the remaining chordwise microphones. The mounted probe tip is in a plane approximately parallel to a chordwise tangent line drawn at the 14% chord location.

The probe was operated at an overheat ratio of 1.7. Calibration is preformed a short period prior to tunnel entry using a jet calibrator. The probe is placed in the jet calibrator and through comparison of the output voltage (E) produced by the hot-wire in the jet flow and the cooling velocity (U_{eff}) sensed by the jet calibrator the hot-wires calibration is obtained. Kings law

$$E^2 = A + BU^n{}_{eff} \tag{2.4}$$

is used. The exponent n is taken as 0.45 and the constants A and B are determined via linear regression from 10 to 15 points. Flow temperatures within the test section were found to fluctuate ±5°F. Hot-wire signals are temperature corrected using the method of Bearman.

2.6 Modified trailing edge

Measurements of the unsteady pressure field are made with a modified sharp trailing edge to reveal trailing edge noise effects. This modification is incorporated using two 1-1/2”wide, 0.025” thick aluminum strips attached to the trailing edge along the entire span on both sides of the airfoil. The strips are attached to the airfoil with double sided tape and meet together to form a 0.050” thick trailing edge which extents the chord by 0.715”. Figure 2.28 illustrates the airfoil in test section after application of the trailing edge modification. A chordwise cross-section is shown in figure 2.29.

Figure 2.28: Airfoil with modified trailing edge

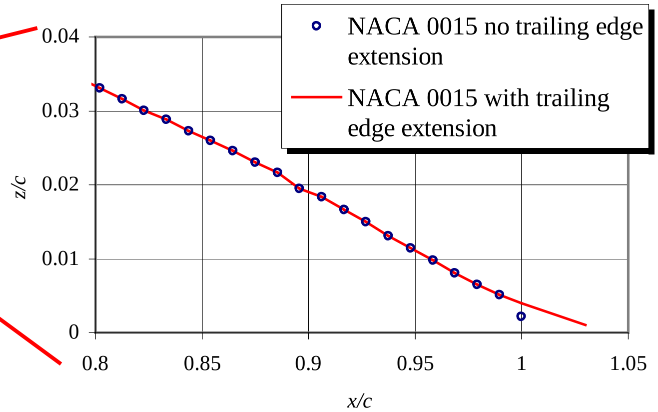

Figure 2.29: Cross section showing trailing edge extension

Figure 2.30 shows a dimensioned cross-section diagram of the airfoil with the trailing edge modification installed.

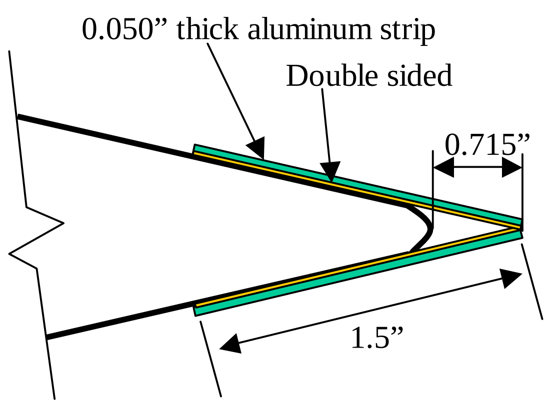

Figure 2.30: Cross section showing dimensioned trailing edge extension

2.7 Tuft flow visualization

Tuft flow visualization was used as an independent method to determine regions of flow separation and examine the homogeneity in the spanwise direction. Tufts, approximately 2-1/2” long made of cotton yarn were attached to the wing in 1” spanwise intervals and varying chordwise intervals with clear tape. The Virginia Tech Stability Wind Tunnel is equipped with clear Plexi-glass windows which provide viewing through one side of the tunnel test section. The tufts are attached to the airfoil on the side exposed to the Plexi-glass and video taped at test velocity (30m/s) for all angles of attack (-20° to 20°). The airfoil with tufts attached is shown in figure 2.31 at 0° angle of attack (flow moving from right to left). Tuft flow visualization was performed following the unsteady pressure measurements in each grid flow and tufts removed immediately after video recording.

Figure 2.31: Airfoil with tufts attached

Examination of the tuft flow visualization indicated significant modification of the flow field through interaction with the tufts. Therefore the actual flow field in which unsteady pressure measurements were made is not necessarily well characterized by the tuft flow. In light of this conclusion these results were not used.

Chapter 3. Predictions

3.1 Mean Pressure

A vortex panel method was used to predict the mean pressure field surrounding the airfoil. 200 points are used to define the geometry of the airfoil. The Virginia Tech Java Vortex Panel applet (http://www.engapplets.vt.edu/) was used to perform the calculations at each angle of attack (0°, 4°, 8°, 12°, 16°, 20°).

3.2 Unsteady Pressure

Part of the theoretical problem of sound due to inflow unsteadiness is that of determining the dynamic pressure distribution on a lifting surface resulting from a time-varying inflow. When the inflow is represented by a Fourier sum of arbitrarily skewed compressible sinusoidal waves encountering a flat plate an approximate closed form expression of the pressure jump across the plat can be derived as done by Amiet (1976a,b).

Amiet, recognizing the poor accuracy of Filotas' (1969) expression recasts the problem into two solution regions, one which is valid at small spanwise wavenumbers (k_y) and the other at high spanwise wavenumbers. In doing so Amiet was able to improve the accuracy of the complete solution to order k_y. Amiet employed Graham's (1970b) similarity rules which relate the general case of a skewed compressible gust to either a parallel compressible gust or a skewed incompressible gust, both of which are much easier to solve depending on the value of the parameter σ, where

$$\sigma = \frac{Mk_x}{\beta k_y} \tag{3.1}$$

and $\beta = \sqrt{1-M^2}$. If $\sigma \le 1$ the similarity is to the skewed incompressible gust, whereas, if $\sigma \ge 1$the similarity is to the parallel compressible gust case.

With the two solution regions defined Amiet (1976b), noting that each of the similarity rules are valid outside of the regime for which they are primarily applicable (Graham 1970b), presents a solution for $\sigma \le 1$ derived from the parallel compressible gust case which is valid for small k_y (< 0.25). Patterson and Amiet (1976a, b), based on Amiet (1976b) give the surface pressure with coordinate system origin at mid-span in this case as

$$\Delta P\left(x, y, t, k_x, k_y\right) = 2\pi\rho_o U w_o g\left(x, k_x, k_y\right) \cdot e^{i\left(k_x Ut - k_y y\right)} \tag{3.2}$$

where $g(x,k_x,k_y)$ is the airfoil response function and defined as

$$g\left(x, k_x, k_y\right) = \frac{S\left(k_x\right)}{\pi}\sqrt{\frac{1-x}{1+x}} \cdot e^{ik_x f\left(k_y / k_x\right)} \tag{3.3}$$

and $S(k_x)$ is the sears function and f is given by

$$f(\xi) = \left(\sqrt{1+\xi^2} - 1\right) \cdot \left(\frac{i\pi}{2} - \ln \xi\right) + \sqrt{1+\xi^2} \cdot \ln\left(1 + \sqrt{1+\xi^2}\right) - \ln 2$$

For large k_y Amiet (1976a) derives the skewed incompressible gust solution using the procedure of Schwartzchild (1902) and Landahl (1961) from which the complete high frequency skewed compressible gust result can be obtained. The problem is formulated based on an infinitesimally thin airfoil representing a line discontinuity at 0° angle of attack. The flow is assumed inviscid and incompressible with Kutta condition applied at the trailing edge. There is no condition specified at the leading edge. The full high frequency, skewed compressible gust derivation is given below.

The unsteady surface pressure field produced by a sinusoidal upwash gust $w = w_0 e^{-i(k_x x + k_y y)}$ with amplitude w_o streamwise and spanwise wavenumbers k_x and k_y (normalized on the half chord b) convecting in a free-stream flow of velocity U, Mach number M, density ρ_o is

$$\Delta p = 2\pi\rho_0 U w_0 g(x, k_x, k_y) e^{i(k_x Ut/b - k_y y)} \tag{3.4}$$

where x and y are chordwise and spanwise coordinates measured from the leading edge (and normalized on the half chord, b), t is time and $g()$ is response function between turbulence velocity and airfoil pressure jump. For a flat-plate airfoil lying in the z = 0 plane between $0 \le x \le 2$ in flow Mach number M the linearized equation for the velocity potential Φ is

$$\left[\nabla^2 - M^2\left(\frac{b}{U}\frac{\partial}{\partial t} + \frac{\partial}{\partial x}\right)^2\right]\Phi(x,z,t) = 0 \tag{3.5}$$

with the boundary conditions

$$\Phi_z(x,0,t) = bw(x)e^{i\omega t} \qquad 0 < x \le 2 \tag{3.6}$$

$$D\Phi/Dt = 0 \qquad\qquad x \geq 2 \tag{3.7}$$

Amiet (1976a) gives a solution for this problem in an iterative manner. The potential can be expressed as

$$\psi^{(1)}(x,y,0) = -\frac{1}{\pi}\int_0^\infty (x/\xi)^{1/2} e^{\left[-(k_y{}^2/\beta^2-\mu^2)^{1/2}+i\mu M\right](x+\xi)}\phi^{(0)}(-\xi,y,0)\frac{d\xi}{x+\xi} \tag{3.8}$$

$$\phi^{(1)} = \phi^{(0)} + \psi^{(1)} \tag{3.9}$$

where $\phi^{(0)}$ is zeroth-order potential, $\phi^{(1)}$ is first-order potential. First-order pressure can be expressed as

$$P^{(1)}e^{i\omega t} = -\rho_0\left(D\Phi^{(1)}/Dt\right) \tag{3.10}$$

A sinusoidal time dependent is assumed, so that

$$\Phi^{(1)}(x,y,0,t) = \phi^{(1)}(x,y,0)e^{i\omega t} \tag{3.11}$$

The trailing-edge pressure correction is found to be

$$p^{(2)}(x,y,0) = -\frac{1}{\pi}\int_0^\infty (r/\xi)^{1/2} e^{\left[-(k_y{}^2/\beta^2-\mu^2)^{1/2}-i\mu M\right](r+\xi)}P^{(1)}(2+\xi,y,0)\frac{d\xi}{r+\xi} \tag{3.12}$$

Where $r = 2 - x$

Now, the pressure on the airfoil can be expressed as

$$P^{(2)} = P^{(1)} + p^{(2)} \tag{3.13}$$

In the case of a gust of the form

$$w = w_0 e^{-i(k_x x + k_y y)} \tag{3.14}$$

the zeroth-order potential becomes

$$\phi^{(0)}(x,y,0) = bw_0\beta^{-1}\left[k_y{}^2/\beta^2 - \mu^2 + (\mu M + k_x)^2\right]^{-1/2} e^{-i(k_x x + k_y y)} \tag{3.15}$$

and thus the trailing edge pressure correction is found to be

$$p^{(2)}(x,y,0) = A\int_0^\infty \frac{1}{(r+\xi)(2+\xi)^{1/2}\xi^{1/2}} e^{-B\xi} d\xi \tag{3.16}$$

where

$$A = \pi^{-3/2} r^{1/2}\rho_0 U w_0 \beta^{-1}\left[\left(k_y{}^2/\beta^2 - \mu^2\right)^{1/2} + (\mu M + k_x)i\right]^{-1/2} e^{-(2+r)\left(k_y{}^2/\beta^2-\mu^2\right)^{1/2} + (2-r)\mu M i - k_y y i}$$

$$B = 2\left(k_y{}^2/\beta^2 - \mu^2\right)^{1/2}$$

Because of the difficulty associated with evaluating (3.16) exactly, we chose to neglect the ξ in the term $(2+\xi)$. The pressure on the airfoil can then be found as

$$P^{(2)} = \left\{1-(x/2)^{1/2}\left\{1-erf\left[\sqrt{2}(2-x)^{1/2}\left(k_y{}^2/\beta^2-\mu^2\right)^{1/4}\right]\right\}\right\}P^{(1)} \tag{3.17}$$

where

$$P^{(1)} = -\rho_0 U w_0 \beta^{-1}\left\{\pi x\left[\left(k_y{}^2/\beta^2-\mu^2\right)^{1/2}+(\mu M+k_x)i\right]\right\}^{-1/2} e^{-x\left(k_y{}^2/\beta^2-\mu^2\right)^{1/2}+(\mu Mx-k_y y)i} \tag{3.18}$$

And finally the pressure jump across the airfoil becomes

$$\Delta p = 2P^{(2)}e^{i\omega t} \tag{3.19}$$

Comparing (3.19) and (3.4) it is clear that the response function $g()$ can be expressed as

$$g(x,k_x,k_y) = -\frac{f(x,k_x,k_y)}{\pi\beta}\left\{\pi x\left[\left(k_y{}^2/\beta^2-\mu^2\right)^{1/2}+i(\mu M+k_x)\right]\right\}^{-1/2} e^{-x\left(k_y{}^2/\beta^2-\mu^2\right)^{1/2}+i\mu Mx} \tag{3.20}$$

where

$$f(x,k_x,k_y) = 1-(x/2)^{1/2}\left\{1-erf\left[\left(2(2-x)\left(k_y{}^2/\beta^2-\mu^2\right)^{1/2}\right)^{1/2}\right]\right\} \tag{3.21}$$

when $k_y \geq \dfrac{M}{\sqrt{1-M^2}}k_x$, and

$$f(x,k_x,k_y) = 1-(x/2)^{1/2}\left\{1-(1-i)E\left[2i(\frac{1}{\pi}(2-x)\left(\mu^2-k_y{}^2/\beta^2\right)^{1/2})^{1/2}\right]\right\} \tag{3.22}$$

otherwise. In these equations, $\beta=\sqrt{1-M^2}$ and $\mu = Mk_x/\beta^2$ and E[] is the Fresnel integral function.

Due to the random nature of turbulence interacting with an airfoil it is necessary to work with statistical quantities such as the cross-power spectrum density of the pressure jump (S_{qq}) at two points on the airfoil surface rather than with ΔP itself. The procedure for formulating S_{qq} in terms of ΔP has been given by Amiet (1975) and summarized here. S_{qq} is defined here as,

$$S_{qq}(x_1, x_2, y_1, y_2, \omega) = \lim_{T\to\infty}\left[\frac{\pi}{T} E\left[\Delta P^*(x_1, y_1, \omega)\Delta P(x_2, y_2, \omega)\right]\right] \tag{3.23}$$

where E[] is the expected value, x_1 and x_2 are different chordwise locations, y_1 and y_2 are different spanwise locations, and T is the sampling period. When replacing ΔP in equation (3.23) with either equation (3.2) or (3.4) and after manipulation the final form of S_{qq} is obtained for a single sided spectrum (i.e. positive frequencies only) as

$$S_{qq}(x_1, x_2, \eta, \omega) = 16(\pi\rho b)^2 \int_0^\infty g^*(x_1, K_x, k_y) g(x_2, K_x, k_y) \Phi_{ww}(K_x, k_y) e^{ik_y\eta} dk_y \tag{3.24}$$

where $\eta = y_1 - y_2$, $K_x = \omega/U$, and Φ_{ww} is the energy spectrum of the turbulence. For programming purposes it is convenient to express $S_{qq}(x_1,x_2,\eta,\omega)$ in Hertz rather than angular frequency. This is accomplished as

$$2\pi \cdot S_{qq}(x_1, x_2, \eta, \omega) = S_{qq}(x_1, x_2, \eta, f) \tag{3.25}$$

where f is frequency in Hertz. Additionally, it is often desired to know $S_{qq}(x_1,x_2,\eta,\omega)$ in terms of P rather than ΔP for comparison with measurements. This is achieved simply by noting that $2P = \Delta P$ and therefore $S^1{}_{qq}(x_1,x_2,\eta,\omega)$ (in terms of P) is given as

$$S^1{}_{qq}(x_1, x_2, \eta, \omega) = \tfrac{1}{4} S_{qq}(x_1, x_2, \eta, \omega) \tag{3.26}$$

To compare with the measurements made using the microphone array a MATLAB code to predict the unsteady surface pressure field using the combined theoretical approach of Amiet (1976a,b) has been developed and utilizes the above formulations of $S_{qq}(x_1,x_2,\eta,\omega)$.

Amiets (1976a,b) prediction scheme requires inputs related to form of the turbulence spectrum, its length scale and turbulence intensity, and half span of the modeled airfoil. All input parameters are summarized in table 3.1.

Table 3.1: Summary of unsteady pressure prediction code input parameters

Input Parameter	**Value**
Turbulence spectral form (Φ_{ww})	von Karman as given by Patterson and Amiet (1976a)
Free-stream velocity, U_∞	30m/s
Large grid length scale, L: *Small grid length scale, L:*	0.0818m 0.0078m
Large grid turbulence intensity: *Small grid turbulence intensity:*	3.93% 4.35%
Airfoil half span, b	0.305m

Chapter 4. Results and Discussion

4.1 Coordinate System and Measurement Conditions

The coordinate system is formed as shown in figure 4.1 with the origin in the plane of the leading edge of the airfoil with *x* directed downstream at mid-span, *y* directed up along the leading edge, and *z* completing the system by the right-hand rule.

The measurement scheme is similar to that described in the Apparatus and Instrumentation section. Three microphone configurations were used to gather data, with the longest chordwise row common to each configuration. Configuration 1 gathers data from the first two spanwise rows (moving back from the leading edge), configuration 2 from the next two spanwise rows and configuration 3 from the last spanwise row. A fourth configuration is used in measurements which were complementary to the core test wherein the second and fourth spanwise rows were used to gather data.

Measurements were made at 11 angles of attack from -20° to +20° in 4° increments, in two grid-generated turbulent flows at one flow speed (30 m/s) corresponding to a chord Reynolds number of 1.17 x 10^6. Positive angle of attack is defined as shown in figure 4.2. Several measurement conditions were considered and presented in table 4.1.

Table 4.1: Measurement conditions

MEASUREMENT CONDITION	***DESCRIPTION***
Unsteady and mean pressure	Measurements of unsteady pressure (via microphone array) and mean pressure (via scani-valve)
Hot-wire (velocity) and unsteady pressure	Simultaneous measurement of velocity (via hot-wire) and unsteady pressure
High frequency unsteady pressure	Measurement of unsteady pressure at higher sampling rate
Trailing edge effects	Measurement of unsteady pressure with modified trailing edge
Matched flow speed	Measurement of unsteady pressure with grid removed matching grid-in mean flow speed
Matched RPM	Measurement of unsteady pressure with grid removed matching grid-in tunnel fan RPM
Symmetry check	Measurement of unsteady pressure at a positive AoA and the same negative AoA
Microphone overload test	Measurement of unsteady pressure at a reduced velocity
Calibration check	Repeated measurement of unsteady pressure at a

	particular AoA and configuration
Flow visualization	Video recording of tuft motion on surface of airfoil

Microphone calibration checks were performed periodically throughout the test by collecting data at a given angle of attack and configuration. Through comparison of auto-spectral data between subsequent calibration checks any microphone calibration drift or change can be inferred.

The microphone saturation and overload test was used to ensure pressure fluctuations were within the measurement range of each microphone. This test is performed by reducing the flow speed to 20m/s and gathering data. Given that a slight reduction in flow speed will not alter the manner in which turbulence interacts with the airfoil other than to reduce the magnitude of pressure fluctuations occurring, the spectral data taken at the test flow speed (30m/s) is compared to the saturation and overload test data for evidence of significant changes in the shape of spectrum implying microphone saturation or overloading.

Measurements were also made with the grid removed at flow speeds which match the mean flow speed with the grid installed and at tunnel fan rotation speeds which match the tunnel fan rotation speed with the grid installed. Matched flow speed measurements allow separation of turbulence/airfoil interaction induced pressure fluctuations from turbulent boundary layer pressure fluctuations. In a similar manner the acoustic field associated with the tunnel fan can be identified through unsteady pressure measurement at matched tunnel fans speed, although this measurement does not account for the grid generated noise as well as noise produced through turbulence interaction with the tunnel fan.

Trailing edge effects on the unsteady and mean pressure were also investigated through the use of a modified trailing edge at the above stated conditions. Also performed were simultaneous velocity (via single wire hot-wire probe)/unsteady pressure measurements. Velocity measurements were made at 14% chord, 1.9cm off the surface of the airfoil at the above stated conditions.

The test matrix is shown in table 4.2.

Table 4.2: Test matrix

MEASUREMENT	***AOA***	***CONFIGURATION***	***GRID SIZE***	***SAMPLING RATE***
Unsteady and mean pressure	0°, 4°, 8°, 12°, 16°, 20°	1, 2, 3	Large	1.6kHz
			Small	12.8kHz

High frequency unsteady pressure	0°, 4°, 8°, 12°, 16°, 20°	1	Large	12.8kHz
	0°	3	Small	25.6kHz
Symmetry check	-8°	4	Large	1.6kHz
			Small	12.8kHz
Hot-wire and unsteady pressure	-16°, -8°, 0°, 8°, 16°	4	Large	1.6kHz
			Small	12.8kHz
Trailing edge effects	0°, 4°, 8°, 12°, 16°, 20°	4	Large	1.6kHz
			Small	12.8kHz
Flow visualization	-20° to 20°	No microphone data taken	Large	n/a
			Small	n/a
Calibration check	0°	1	Large	1.6kHz
Microphone saturation and overload	20°	1	Large	1.6kHz
Matched flow speed	0°, 4°, 8°, 12°, 16°, 20°	4	None	1.6kHz
Matched RPM	0°	4	Tunnel RPM 350	1.6kHz
			Tunnel RPM 378	12.5kHz

500 records with 2048 samples per record of unsteady pressure and velocity data were taken with the HP1432A at sampling rates of 12.8kHz and 1.6kHz for the small and large grid flows respectively. Additionally, to obtain high resolution data across the frequency range of interest the sampling rate at some select conditions was increased to 25.6kHz and 12.5kHz for the small and large grid flows respectively.

After the completion of all unsteady pressure and velocity measurements tuft flow visualization was performed on the surface of the airfoil in both large and small grid turbulent flows. 5.1cm long tufts were placed at 4.2% chord spanwise increments and varying chordwise increments.

This work presents unsteady pressure measurements in both turbulence length scale flows at 30m/s for 0°, 4°, 8°, 12°, 16°, 20° angle of attack.

4.2 Blockage Effects

The airfoils presence in the wind tunnel test section produces effects which act to modify the flow field surrounding the airfoil. The most significant effects were those of solid and wake blockage and restriction of streamline curvature. Solid and wake blockage act to produce an incremental change in the velocity field around the airfoil while streamline curvature restriction acts to alter the lift (and therefore angle of attack) and moment.

The velocity increment related to solid blockage is estimated through the method of Allen and Vincenti (1944). They give

$$\frac{\Delta V}{V} = \varepsilon_{sb} = \lambda\sigma \tag{4.1}$$

where λ is defined as the body shape factor and given as

$$\lambda = \frac{16}{\pi}\int_0^l \frac{z}{c}\left\{\left[1 - P\left(\tfrac{x}{c}\right)\right]\cdot\left(1 + \frac{dz}{dx}\right)\right\}^{1/2} dx \tag{4.2}$$

with z and x as airfoil coordinates, c is chord, and $P(x/c)$ is pressure distribution. Also,

$$\sigma = \frac{\pi^2}{48}\left(\frac{c}{h}\right)^2 \tag{4.3}$$

where h is the wind tunnel height. The NACA 0015 body shape factor is 0.31 which gives a solid blockage factor of 0.71%. That is, at a clear test section velocity of V = 30m/s the incremental change in velocity is ΔV = 0.21m/s.

Wake blockage is estimated based on Maskell's (1965) method and given as

$$\varepsilon_{wb} = \frac{c/h}{2} C_d \tag{4.4}$$

where C_d is the drag coefficient. This method has been used to estimate the blockage at each angle of attack.

The effects on C_l and α associated with streamline curvature restriction is given by Barlow, Rae, and Pope (1999) as

$$\Delta C_{l,sc} = \sigma \cdot C_l \tag{4.5}$$

$$\Delta \alpha_{sc} = \frac{\sigma \cdot C_l}{2\pi} \tag{4.6}$$

Table 4.3 summarizes the effects of solid and wake blockage and streamline curvature restriction for both small and large grid configurations at each angle of attack.

Table 4.3: Summary of blockage effects

	LARGE GRID				***SMALL GRID***			
AoA	**ε_{sb} (%)**	**ε_{wb} (%)**	**$\Delta\alpha_{sc}$ (deg)**	**$\Delta C_{l,sc}$**	**ε_{sb} (%)**	**ε_{wb} (%)**	**$\Delta\alpha_{sc}$ (deg)**	**$\Delta C_{l,sc}$**

0°	0.708	0.082	0.000	0.000	0.708	0.082	0.000	0.000
4°	0.708	0.125	0.094	-0.010	0.708	0.125	0.094	-0.010
8°	0.708	0.167	0.181	-0.020	0.708	0.167	0.196	-0.021
12°	0.708	0.250	0.263	-0.029	0.708	0.300	0.288	-0.032
16°	0.708	0.267	0.313	-0.034	0.708	0.333	0.358	-0.039
20°	0.708	0.217	0.233	-0.025	0.708	0.317	0.383	-0.042

The combined effects of solid and wake blockage produce at most slightly more than 1% change in velocity in both grid flows which is expected to negligibly affect unsteady pressure measurements. Streamline curvature restriction produced up to a 0.38° increase in angle of attack occurring in the small grid flow at α = 16° and as much as a 0.042 reduction in C_l occurring again in the small grid flow at α = 20°. The changes implied by the streamline curvature restriction correction are considered small and will not adversely affect unsteady pressure measurements.

4.3 Uncertainties

An approximation of the uncertainty in unsteady pressure measurements has been made based on repeated measurements. That is, at any one angle of attack three data acquisition configurations are required to define the blade response function with the longest chordwise row of microphones common to each configuration. Therefore, by considering the three repeated measurements of the longest chordwise row the uncertainty in the pressure difference spectra can be obtained at each chordwise location. This technique will, of course not allow for an estimate of the uncertainty in each microphone calibration.

Table 4.4 presents the uncertainty in pressure difference spectra at 1 and 4% chord in decibels (dB) for three angles of attack in large grid flow at 20 to 1 odds (95%).

Table 4.4: Summary of uncertainties in pressure difference spectra at two chordwise locations in large grid flow

ω_f	**Uncertainty at *x/c* = 0.1 (dB)**	**Uncertainty at *x/c* = 0.4 (dB)**
α = 0°		
1	0.58	0.92
10	0.49	0.40
35	0.81	0.18

α = 8°		
1	2.08	0.38
10	1.19	0.22
35	2.90	0.21
α = 20°		
1	0.58	1.73
10	1.44	0.21
35	2.24	0.18

Uncertainties tend to be fairly consistent across the frequency range and show some increase at higher angles of attack. The increase in uncertainty at higher angels of attack may be a consequence of three-dimensional unsteady flow features which did not manifest in repeated measurements. In general the pressure difference spectra from 6% chord appear to be slightly more certain than those at 1% chord.

Table 4.5 presents uncertainties at 1 and 4% chord in the presence of small grid flow for three angles of attack, again at 20 to 1 odds.

Table 4.5: Summary of uncertainties in pressure differenced spectra at two chordwise locations in small grid flow

ω_r	**Uncertainty at *x/c* = 0.1 (dB)**	**Uncertainty at *x/c* = 0.4 (dB)**
α = 0°		
10	0.58	0.46
100	0.50	0.57
300	0.36	0.38
α = 8°		
10	0.33	1.20
100	5.32	1.06
300	10.94	1.47
α = 20°		
10	1.22	0.57
100	2.33	1.18
300	6.52	1.10

Small grid flow uncertainties show similar trends as those of the large grid although are somewhat greater at higher reduced frequencies.

4.4 Mean Flow Field Characteristics

Characterizing the mean flow field around the airfoil in terms of stagnation point, boundary layer transition, and separation location assists in the interpretation of unsteady pressure data.

4.4.1 Large Grid Mean Pressure and Separation

Through examination of mean pressure data, and chordwise and spanwise unsteady pressure auto-spectrum estimated locations of flow separation (and reattachment as is the case at 16° angle of attack) can be inferred. Figure 4.3 shows the experimentally calculated C_L vs. α (angle of attack in degrees) for the present experiment with the airfoil immersed in the large scale flow plotted with McKeough's (1976) data. Lift coefficient is calculated from integration of mean pressure along the airfoil chord. Mean pressure measurements were made at 0°, 4°, ±8°, 12°, 16°, 20° angle of attack with and without the trailing edge modification. Measured pressure is plotted with theoretical data for each angle of attack in figures 4.5-4.10 with $-C_p$ plotted verse *x/c*. McKeough made many measurements of lift, several of which were on a NACA 0015 in several different scale and turbulence intensity flows with the goal of characterizing the mean flow field at angle of attack. In addition, McKeough made measurements of unsteady lift on a NACA 0015 in grid generated turbulence at 0° and 10° angle of attack. The results of McKeough's measurements will be used throughout the discussion of the present experimental result due to the similarities between the two experiments. GS1 through GS6 of figure 4.3 represent turbulent flows with decreasing turbulence intensity and increasing length scale as demonstrated in figure 4.4. GL represents a larger scale turbulence which is similar in turbulence intensity and length scale to the large scale flow of the present experiment. Also plotted in figure 4.3 are McKeough's data for smooth flow (i.e. no grid) at two Reynolds numbers (0.26×10^6 and 0.76×10^6). Figure 4.3 clearly demonstrates in the present large scale turbulent flow experiment an unstalled regime from 0° to 16° angle of attack which is supported by the mean pressure data presented in figures 4.5 to 4.9. At 20° the airfoil is completely stalled as demonstrated by the large loss of lift as shown in figure 4.3 and reduction in mean pressure in figure 4.10. The reduction in lift curve slope at 16° angle of attack indicates the presence of some separated flow and is consistent with McKeough's GL data and further supported by McKeough's own flow visualization test which indicate the development of a laminar separation bubble in the leading edge region and some trailing edge separation. It should be noted that the laminar separation bubble is a three dimensional phenomena as observed by McKeough's flow visualization test. This conclusion is further grounded by comparison of the mean pressure field at 16° angle of attack (figure 4.9) with panel method calculations which show a loss of pressure over the first 5% chord. Also, the chordwise auto-spectra at 16° angle of attack show a distinct increase in level across much of the frequency range as separation begins in the trailing edge region which is consistent with the auto-spectral levels obtained at 20° (fully stalled) angle of attack.

4.4.2 Small Grid Mean Pressure and Separation

Figures 4.11 to 4.16 present mean pressure data plotted with predicted values. As mentioned in Chapter 2 these data were taken with the reference pitot-static probe located upstream of the grid. If P_o and P_∞ are defined as the stagnation and static pressure upstream of the grid and P_{o2} and $P_{\infty 2}$ as the stagnation and static pressure downstream of the grid then the measured pressure coefficient, C_{PM} is formed as

$$C_{PM} = \frac{P-P_\infty}{P_o-P_\infty} \qquad 4.7$$

where P is the pressure measured on the surface of the airfoil. Due to the pressure loss occurring across the grid C_{PM} must be recast in order to determine the true coefficient of pressure on the airfoil surface. Through algebraic manipulation and utilizing the pressure coefficient measured near the stagnation point on the airfoil, C_{PMo} as a reference the true coefficient of pressure, C_P can be obtained as

$$C_P = \frac{P-P_{\infty 2}}{P_{o2}-P_{\infty 2}} = 1 + C_{PM} - C_{PMo} \qquad 4.8$$

This technique was initially utilized to adjust the small grid mean pressure data. Although, upon application the agreement between theory and measured values was poor everywhere except for in the leading edge region with the data situated as much as 12.5% above predicted values at α = 0°. Curiously, the agreement improves as angle of attack increases. Through further manipulation, namely adjusting the measured data to reasonable agreement with predicted values across the chord the experimental values were found to match the prediction quite well with exception to the pressure side leading edge region which showed $-C_P < -1$ for all non-zero α's. This of course is an impossible result and therefore requires at least an attempted justification. Basically, error in the small grid mean pressure data could be introduced by two avenues; 1) The airfoil, which is situated only ¾ of a chord downstream of the grid has a significant upstream influence on the grid which causes non-uniformity in the flow or 2) a measurement error occurred, perhaps in the form of a poor tubing connection or malfunctioning pressure transducer.

First, consider possibility 1). Using a 2-dimensional conformal mapping potential code (Virginia Tech Ideal Flow Machine, http://www.engapplets.vt.edu/) with a Joukowski symmetric

15% thick airfoil the upstream influence caused by the airfoil on the mean velocity at the grid has been estimated. Figure 4.17 shows the streamlines around the airfoil at $\alpha = 4°$. This angle of attack was chosen since the difference in measured and predicted mean pressure values are greatest at small angles of attack. Using results produced by the Ideal Flow Machine along the stagnation streamline a 2% decrease in mean velocity was shown to occur at the grid. This in turn results in a 4% rise in C_P which is not substantial enough to account for the 10% difference in measured and predicted mean pressure values at $\alpha = 4°$. Additionally, the very fact that measured and predicted mean pressure are in better agreement at high angles of attack makes this argument an unlikely culprit.

Now, consider possibility 2). For $C_P > 1$ the measured pressure, P_M must be too high. This situation could develop, if for example an airfoil pressures tap tube was not completely sealed at some connection. In this situation, if the pressure on the surface of the airfoil, P, was below the ambient pressure, P_a the leak would cause an artificial rise in the actual measured pressure, P_M which in turn would cause C_{PM} to be too small. This is one possible and seemingly reasonable cause for the rise in C_P in the leading edge region. Of course, the preeminent solution to this problem is a re-measurement of the small grid mean pressure. This is not feasible for incorporation in this thesis although is planned for future study. Although, for some the implications of this problem may leave a question mark over the fidelity of the measured unsteady pressure in the small grid flow, one should keep in mind that all other measured data (e.g. spanwise homogeneity, lift coefficient) produce expected results.

Figure 4.3 also depicts the small scale flow experimentally calculated C_L vs. α for the present experiment which indicates unstalled flow over the entire angle of attack regime. As angle of attack is pushed beyond 12° the lift curve slope begins to decrease in the presence of a developing laminar separation bubble. This phenomenon is verified through the observance of a flattened segment in the leading edge region of the mean pressure curve of figure 4.14 and, again, via McKeough's flow visualization experiments. The laminar separation bubble extents over the first 4% chord at 16° angle of attack and 5% chord at 20° angle of attack as demonstrated by mean pressure data. McKeough noted that in the absence of small scale turbulence or some other type of small scale energizing disturbance the laminar separation bubble which forms in the leading edge region will burst resulting in stall as angle of attack is increased. It is therefore believed that the small scale (on the order of boundary layer turbulence scales), high intensity turbulence produced by the small grid interacts with the boundary layer allowing an increase in the entrainment of freestream, high kinetic energy fluid which more readily overcomes the severe adverse pressure gradient present at high angle of attack. In addition, this same effect is believed to cause the increase in lift curve slope (slight beyond $2\pi\alpha$) from $\alpha = 0°$ to 12° as compared to the large grid lift curve slope.

4.4.3 Smooth Flow Separation

Although no smooth flow mean pressure data was taken an approximate idea of the flow field surrounding the airfoil can be made through assessment of unsteady lift data (formed by integrating unsteady pressure along the chord). Lift spectra, presented in section 4.10 indicate separated flow fields at $\alpha = 16°$ and 20°. A comparison between the lift spectra at $\alpha = 20°$ (stalled) in the large grid flow with $\alpha = 16°$ and 20° of the smooth flow (figure 4.64) shows similar unsteady lift spectra levels and shape. In addition the smooth flow unsteady lift at α = 16° and 20° rise as much as two decades in G_{ll} above the remaining angles of attack due to large scale pressure fluctuations related to separated flow.

4.4.4 Boundary Layer Transition

Boundary layer transition can be inferred from high pass filtered unsteady pressure time series and supported, in the case of large scale turbulence (wherein the turbulence scales are much larger than those occurring in the boundary layer and therefore tend not to interact) by the smooth flow measurements of unsteady pressure. Time series, when contour plotted with time on the abscissa, chordwise distance on the ordinate and isolines of constant pressure clearly reveal the location where high frequency, turbulent boundary layer pressure fluctuations begin to develop.

Figures 4.18-4.23 show large grid unsteady pressure time series with *x/c* on the vertical axis and *tU/c* on the horizontal axis. These plots have been formed with the large grid high frequency (12.8kHz) data which is high passed filter at 1000Hz to reveal turbulent boundary layer pressure fluctuations. The green line drawn across each plot denotes the approximate location where transition occurs. This location is determined by noting the subtle change in frequency of pressure fluctuations as the chord is traversed. For example, at $\alpha = 0°$ (figure 4.18) in the leading edge region unsteady pressure fluctuations are somewhat smooth and have a longer period than those at more distant chordwise locations. The change between the two regions indicates the approximate location of transition. At higher angles of attack, $\alpha = 12°$, $16°$, and $20°$ (figures 4.21, 4.22, 4.23) transition was found to occur in front of the most leading edge microphone (1% chord) on the suction side of the airfoil. The transition location is therefore taken as the leading edge, although no line has been drawn to indicate this.

Small grid unsteady pressure time series revealed turbulent boundary layer pressure fluctuations at the most leading edge microphone (1% chord) at all angles of attack and therefore have are not presented here.

Boundary layer transition can be approximated based on the flat plate theoretical method of Van Driest and Blumer (1963). This theory is rooted in the physical concept that transition will occur at some critical value of Reynolds number based on vorticity in the boundary layer. Van Driest and Blumer give

$$\frac{1690}{\mathrm{Re}_{x,trans}^{\frac{1}{2}}} = 1.0 + 19.6 \cdot \mathrm{Re}_{x,trans}^{\frac{1}{2}} \left(\frac{(\overline{u'})^2}{U_e^2} \right) \tag{4.9}$$

to predict the transition Reynolds number. Using freestream turbulence levels of 3.93% and 4.35% for the large and small grid test flows (30 m/s) respectively the large grid flow transition Reynolds number is 48550 and small grid flow transition Reynolds number is 40160. This results in a transition location of 4.6% chord in large grid flow and 3.8% chord in small grid flow at $\alpha = 0°$. In the large grid flow this method tends to predict transition prematurely at $\alpha = 0°$ as a consequence of the flat plate model which does not account for the strong favorable pressure gradient in the leading edge region of the airfoil that acts to suppress instabilities. The small grid flow, with an integral length scale on the order of the boundary layer thickness induced near immediate transition which is not well predicted by the method of Van Driest and Blumer.

4.4.5 Stagnation Points

The approximate stagnation point location is easily obtained from predicted mean pressure by observing the point where C_p achieves unity.

4.4.6 Summary of Stagnation, Transition, and Separation Points

Figure 4.24 and 4.25 show a summary of the first 30% and 60% chord with stagnation, transition and separation locations indicated at each angle of attack for small and large scale turbulence respectively. The upper (positive) half of each figure represents the suction side of the airfoil.

Stagnation points for both scale flows, as expected moves down the chord with increasing angle of attack. Also, figure 4.25 demonstrates with increasing angle of attack in the unstalled regime a counterclockwise rotation in transition location about the airfoil. The transition location moves forward on the suction side (until separation occurs) and backward on the pressure side (to a maximum of 45% chord) with increasing angle of attack. Separation as previously discussed occurs in a small region over the leading edge and after 50% chord at 16° angle of attack. At 20° angle of attack the flow separates off the leading edge and does not reattach.

Transition is shown to occur immediately on pressure and suction sides of the airfoil in the small scale flow. As previously discussed and shown in figure 4.24 separation occurs in the leading edge region over 4% chord at 16° and 5% chord at 20° angle of attack.

4.5 Verification of Flow Homogeneity

Flow homogeneity across the span of the airfoil can be verified through comparison of auto-spectra in each spanwise row (rows 1 to 5). Figures 4.26 to 4.30 present auto-spectrum (G_{pp}) versus frequency for the pressure and suction side of the airfoil at $\alpha = 0°$. Similar plots are presented in figures 4.31 to 4.35 and 4.36 to 4.40 for $\alpha = 8°$ and 20° respectively. Here, in the discussion of homogeneity *z/c* is taken as the spanwise coordinate and exactly replaces *y/c* in figure 2.16 (microphone layout).

A slight in-homogeneity is revealed in the leading edge region (figure 4.26, row 1) on the pressure side of the airfoil at $\alpha = 0°$ and is believed to be associated with the access hatch/airfoil seam. This in-homogeneity is quickly dissipated and homogeneous flow resumes over much of the leading edge region with exception to higher frequencies in row 4 and 5, the ambiguities of which are believed to be associated with the 3-dimensional nature of boundary layer transition. Homogeneity is well demonstrated on the suction side of the airfoil at $\alpha = 0°$ (figures 4.26-4.30) with exception to three microphones. The microphone located at 0.98 *z/c* in row 2 on the suction side displays an unusual shape which may be indicative of non-uniform flow in this region possibly as a result of the microphones mounting location near the edge of the access hatch or a faulty cable connection. Data from this microphone is in close agreement with data from other microphones in row 2 at higher angles of attack as shown in figure 4.32 and 4.37. Also, the auto-spectrum in row 1 at 0.98 *z/c* on the suction side takes on an unusual form at higher angles of attack further suggesting some type of flow irregularity in this region. The microphone located at 0.24 *z/c* in row 5 on the suction side was found to be faulty and did not produce reliable data and has therefore been omitted from any further data analysis. A bad calibration is believed to result in the increased levels measured with the microphone at 0.27 *z/c* in row 5 on the suction side.

Figures 4.31 to 4.35 demonstrate homogeneous flow across the frequency range on the pressure side of the airfoil at $\alpha = 8°$ for each spanwise location. On the suction side a slight low frequency in-homogeneity is present in row 1 conceivably related to shifting of the stagnation point along the span. The auto-spectrum measured at 0.98 *z/c* in this row indicates the presence of a strong in-homogeneity perhaps associated with the hatch/airfoil seam. The high frequency roll up shown in the auto-spectra at 0.24 *z/c* in row 3 and 4 (figure 4.33 and 4.34) on the suction side can be attributed to the 3-dimensionality of boundary layer transition. With the airfoil stalled at $\alpha = 20°$ homogeneity is well preserved in row 1, 2, and 3 (figures 4.36, 4.37, and 4.38) on the pressure side. The auto-spectrum at 0.02 *z/c* in row 4 on the pressure side shows significant deviation perhaps related to a 3-dimensional boundary layer disturbance or an airfoil/hatch seam effect. Also, slight spreading apart of spectra at high frequency is apparent in row 4 and 5 on the pressure side further suggesting some type of boundary layer effect. On the suction side significant low frequency variation is shown in row 1, 2 and 3 which may result from 3-dimensional stall effects. In-homogeneities associated with the airfoil/hatch seam are revealed in data taken on the suction side at 0.98 *z/c* in row 1. High frequency homogeneity is well demonstrated across the chord on the suction side.

These data show well preserved homogeneity across the airfoil span at all angles of attack. Some slight hatch/airfoil interface, three dimensional effects, and possible poor microphone cable connection are present although these do not adversely affect the experiment results.

4.6 Sources of Noise

In investigating unsteady pressure on the surface of an airfoil many sources of pressure fluctuations are present, all of which have the potential to dominate the pressure field and contaminate the desired turbulence/airfoil interaction measurement. These pressure fluctuations can result from windtunnel acoustic field, boundary layer, stall, and convection of eddies.

Through the application of cross-spectral methods boundary layer noise can be removed for cases where the microphone separation is greater than the dominant boundary layer turbulence length scale. This technique has been utilized in all spectral data presented by pressure differencing pressure and suction side data. A possible technique to allow the subtraction of the acoustic field would be to consider the cross-spectrum of signals generated on the airfoil surface with that measured by the reference microphone. Although, given the reference microphones close proximity to the airfoil it is unclear if some correlation between the desired signal would exist thus potentially diminishing the turbulence/airfoil interaction signal upon subtraction. This technique therefore has not been used. Also, matched flow speed and RPM data and reference microphone measurements provide a technique to assess the airfoil response in the presence of smooth flow and serve well as a baseline estimation of the noise level.

Pressure difference auto-spectra (in decibels, dB) are presented at eight chordwise locations (1, 2.5, 4, 6, 9, 14, 20, and 30%) for the cases of matched flow speed at all angles of attack, matched RPM at $\alpha = 0°$, and reference microphone measurement in figures 4.41 and 4.43. Figures 4.42 and 4.44 present the corresponding coherence and phase of these signals. The pressure difference auto-spectrum in N^2/m^4, $G_{\Delta P\Delta P}$ is defined as

$$G_{\Delta P\Delta P}(\omega_r, x) = G_{P1P1}(\omega_r, x) + G_{P2P2}(\omega_r, x) - \mathrm{Re}(G_{P1P2}(\omega_r, x)) \tag{4.10}$$

where $G_{P1P1}(\omega_r,x)$ and $G_{P2P2}(\omega_r,x)$ are, respectively, the auto-spectra of pressure fluctuations on the pressure and suction sides of the airfoil at a given chordwise (x) location, and $G_{P1P2}(\omega_r,x)$ is the cross-spectrum between pressure and suction sides. Also, $\omega_r = \dfrac{\pi \cdot f \cdot c}{U_\infty} \equiv$ reduced frequency where, c = chord (m), f = frequency (Hz), U_∞ = free-stream velocity (m/s). Coherence and phase are defined as

$$\gamma^2 = \frac{|G_{P1P2}|}{G_{P1P1}G_{P2P2}} \tag{4.11}$$

$$\phi = \arctan\left(\frac{\mathrm{Im}(G_{P1P2})}{\mathrm{Re}(G_{P1P2})}\right). \tag{4.12}$$

As stated in the test matrix (table 4.2) matched flow speed data was taken for α = 0°, 4°, 8°, 12°, 16°, 20° and matched RPM data for α = 0°. At the unstalled (0°, 4°, 8°, 12°) angles of attack the matched flow speed and matched RPM spectra remain as much as 30dB below the reference microphone spectrum at all eight chordwise locations over much of the frequency range varying from as high as 115dB at α = 12° to as low as 65dB at α = 0°. The reference microphone, as discussed in Chapter 2 may, by it's existence in the flow generate noise and thus the spectrum produced represents an upper bound on the tunnel acoustic field. Therefore, the fact that smooth flow data remains below the upper bound tunnel acoustic field indicates the low level of noise present at the airfoil surface. Also, across chord phasing (figures 4.42 and 4.44) remains at nearly 0° at each chordwise location for the unstalled angles of attack indicating the primary source of pressure fluctuation is acoustic related. Coherence, although reaching to 0.8 at some frequencies is quite 'spiky' and falls off at higher reduced frequencies (>10) beyond 9% chord demonstrating the weak nature of the dominant pressure fluctuation.

Stalled angle of attack spectra (16° and 20°) are well above the reference microphone spectrum, which is expected considering the unsteadiness associated with stall. The α = 16° and 20° spectra remain within 8dB of each other at all eight chordwise locations with, interestingly the α = 16° spectrum in general residing at a higher level than the α = 20° spectrum. These spectra achieve between 120 and 130dB at the lowest reduced frequency and fall to as low as 80dB at the highest reduced frequency. Therefore, it can be concluded that at stalled angles of attack the large unsteady pressure fluctuations occurring in the presences of the separated flow will dominate the unsteady pressure measurement.

Therefore, based on the low pressure difference spectral levels of matched flow speed, matched RPM and reference microphone data and the application of cross-spectral techniques (i.e. pressure differencing) the turbulence/airfoil interaction pressure fluctuations are expected to be the dominate source of pressure unsteadiness at unstalled angles of attack. At stalled angles of attack the large pressure fluctuations associated with the separated flow field are expected to dominate the unsteady pressure measurement.

4.7 Time Series

As described above many types of pressure fluctuations exist within the unsteady surface pressure field. These pressure fluctuations can be further revealed and the physics more clearly defined through investigation of the instantaneous pressure field (i.e. calibrated time series).

Figure 4.45 to 4.56 present contour plots of the instantaneous pressure field in space (x/c) and time (tU_∞/c) for each angle of attack on both pressure and suction sides of the airfoil immersed in large and small grid turbulence. Large grid instantaneous pressure is high pass filtered at 10Hz and small grid at 30Hz to remove low frequency uncertainties which arise from the microphone calibration. Low pass filtering is performed by the data acquisition system (HP1432) and ensures unaliased data beyond 500Hz in the large grid flow and 5000Hz in the small grid flow. Plotting instantaneous pressure as such will reveal the convection speed of various types of pressure fluctuations occurring on the surface of the airfoil. For example, a fluctuation which is convecting with the mean free stream velocity will have a 1 to 1 slope. Similarly, a fluctuation propagating downstream at sound speed will have a slope of 12 to 1 (speed of sound + mean free stream velocity to mean free stream velocity) and a fluctuation prorogating upstream at sound speed will have a slope of 10 to 1.

At $\alpha = 0°$ eddies strike the leading edge and cause an instantaneous adjustment of angle of attack (due to the upwash velocity) which is made at sound speed (slope of 12:1) as well as a pressure rise in the leading edge region on one side of the airfoil which is balanced by a pressure reduction on the opposing side. The eddy continues to distort and convect close to the mean free stream velocity (1:1 slope) over the leading edge and across the surface. This phenomenon is clearly demonstrated in the larger scale turbulence (figure 4.45 and also visible at the smaller scale (figure 4.46). The small grid data, which is taken at a higher frequency also reveals turbulent boundary layer pressure fluctuations occurring over much of the chord and are shown as the hashed high and low pressure fluctuations.

As angle of attack is moved to 4°, 8° and 12° (figures 4.47 - 4.52) the stagnation point begins to move off the leading edge and pressure fluctuations become more severe over the leading edge region. Pressure fluctuations propagating at sound speed as well as free stream velocity are clear visible in both turbulence scale flows. The variation in upwash velocity is nicely demonstrated in the leading edge region through the oscillation between high and low pressure with time. That is, if we consider an idealized disturbance to be a sinusoidal wave, one side of the airfoil leading edge will experience a steady rise above the mean pressure as the first quarter of the wave is encountered followed by a steady decrease back to mean pressure at the wave mid-point and then further decreasing below mean pressure to the three-quarter point and finally a rise back to mean pressure. The opposing side of the airfoil will experience exactly the opposite pressure which, as will be shown later is supported well by phasing of pressure difference auto-spectrum.

Pushing the angle of attack to 16° the large grid measurements show (figure 4.53) pressure fluctuation propagating close to sound speed on the pressure side of the airfoil while eddy convection at slightly less than mean velocity is visible on the suction side. As mentioned above at α = 16° in the large scale flow a laminar separation bubble develops over the first 8% chord. At the point of reattachment high frequency pressure fluctuations are expected due to the unsteady nature of separation although these are not well revealed by the 1600Hz sampling rate in the large grid flow. The flow separates again at 50% chord and a region of back flow develops which reduces the eddy convection speed and is shown as a decrease in slope of pressure fluctuations occurring over this region. In the presence of small scale turbulence (figure 4.54) the flow remains attached and both sound speed and free stream velocity propagation speeds are visible.

Finally, in the large scale turbulence at α = 20° (figure 4.55) the airfoil is completely stalled with considerable back flow occurring over much of the suction side airfoil surface. This results in large scale pressure fluctuations convecting at roughly half the mean free stream velocity (1/2:1 slope). Pressure fluctuations transmitting downstream as well as upstream (slope 10:1) at near sound speed are present on the pressure side of the airfoil. The flow remains attached at α = 20° in the presence of small scale turbulence (figure 4.56). Pressure fluctuations are similar to those shown at α = 16° with a slight increase in magnitude on the suction side due to increased unsteadiness in the presence of the strong adverse pressure gradient.

4.8 Turbulence Characteristics

A note on some important distinctions between the large and small scale turbulence flow is necessary and will serve to facilitate the discussion of turbulence/airfoil interaction. Figure 4.57 presents the relationship between the average wavenumber magnitude, $|k|$ and the streamwise wavenumber, k_1 for the small and large grid turbulence as well as the turbulence produced in McKeough's (1976) unsteady lift experiments, assuming von Karman spectral forms. The average wavenumber magnitude is defined as $|k| = \sqrt{k_1 + k_2 + k_3}$, where k_2 is the spanwise wavenumber and k_3 the later wavenumber. This figure shows a large separation (1 order of magnitude) in $|k|b$ between large and small scale turbulence occurring over 0.1 to 1 k_1b. Also, a ¾ order of magnitude difference in $|k|b$ occurs between the large grid flow and McKeough's flow. The large separation in wavenumber magnitude results in two distinct turbulence/airfoil interaction regimes, one which enhance unsteady pressure fluctuations and the other which suppresses unsteady pressure fluctuations in the presence of mean loading. The large grid spectrum begins to roll up at $k_1b = 2$ and converges near the small scale spectrum at $k_1b = 30$. McKeough's spectrum curves up at $k_1b = 1$ and converges with the large grid spectrum at $k_1b = 2$. The region over which the wavenumber magnitude spectra begin to converge denotes the onset of a similar turbulence/airfoil interaction phenomena in each of the turbulent flows, namely enhanced unsteady pressure fluctuations in the presence of mean loading.

4.9 Pressure Difference Spectra

4.9.1 Large Grid

Pressure difference auto-spectra levels for the large grid are plotted in decibels (dB) against reduced frequency, ω_r at eight chordwise locations in figure 4.58 and 4.60 for all angles of attack, α. Spectra were averaged along the airfoil span to minimize uncertainties. Coherence γ^2 and phase ϕ between pressure and suction side fluctuations at the same eight locations are plotted in figures 4.59and 4.61, again for all angles of attack.

The pressure difference spectra exhibit a flattened region extending to $\omega_r = 3$ for all unstalled angles of attack (0°, 4°, 8°, 12°, 16°) up to 14% chord. The flattening of pressure differenced spectra at low ω_r correlates well with the flattening of $|k|$ as k_1b becomes small and thus seems to imply that for small values of k_1 the turbulence flow field appears similar to the airfoil.

A slight variation of spectral levels with angle of attack is visible for the unstalled angles of attack in the $\omega_r < 4$ region primarily at 1, 2.5, 4 and 14% chord in the form of a reduction in level of up to 4 dB with increasing angle of attack. This reduction in spectral level is quite an unforeseen result given the earlier results of McKeough (1976) and Patterson and Amiet (1976a, b). McKeough demonstrated an increase in unsteady lift (as a consequence of increased unsteady pressure) on a NACA 0015 between $\alpha = 0°$ and $10°$ occurring primarily at low ω_r. Patterson and Amiet observed a slight increase in surface pressure on a NACA 0012 occurring between $\alpha = 0°$ and $8°$. McKeough and Graham (1980) maintained the increase in unsteady lift (and therefore pressure) at low reduced frequencies must be at least a second order effect in the case of isotropic, homogenous turbulence. This result can be rationalized by considering a Taylor series expansion of the blade response in α. The unsteady pressure receives equal contributions from both upwash and downwash velocity, both of which have equal probability of occurrence in isotropic flow and therefore any effects due to angle of attack must only depend on even powers of α. The source of this reduction in unsteady surface pressure is unclear although the manner in which it manifests itself seems to depend on the turbulence scale. Keeping in mind the large separation which exists between the large and small grid flows in $|k|$ below $k_1 b = 3$ a correlation and possible source of this effect may be revealed by inspection of small scale turbulence flow spectra.

In the $\omega_r > 10$ range, an increase in spectral level is shown with increasing angle of attack This high reduced frequency region corresponds to a region of high $|k|$, similar in magnitude to that of the small scale flow, as shown in figure 4.57. The increase in spectral level with increasing angle of attack appears to be related to the increased distortion of small wavenumber turbulence which is modified by the potential velocity field.

At the stalled angle of attack (20°) the shape of the spectrum is distinctly different from the unstalled with the exception of the 1% chord location. In the leading edge region (2.5, 4, and 6% chord) the 20° angle of attack spectrum is up-to 5dB higher than at the unstalled angles of attack. This result appears to be related to low frequency pressure fluctuations which occur around the airfoil as a consequence of the stalled flow field and are verified by comparison with smooth flow unsteady pressure data at $\alpha = 20°$ (stalled) which exhibit similar shape. Between 9 and 30% chord the stalled spectrum begins to rise 5 to 15dB above unstalled spectrum across the reduced frequency range as a result of strong pressure fluctuations related to backflow occurring on the suction side of the airfoil.

Figures 4.59 and 4.61 nicely demonstrate the anti-phasing that occurs as the airfoil encounters turbulence, which, as discussed above is clearly visible in the calibrated time series. This phenomenon is primarily a low reduced frequency (<10) occurrence in the presence of an actual airfoil with thickness and is visible up to 20% chord. The across chord pressure phasing does not remain at 180° due to the finite distance which separates the pressure and suction side microphone. That is to say the phasing becomes spatially aliased as a consequence of integration across all spanwise wavenumbers which tends to shift the two pressure signals to 0° phasing. This phenomenon reveals an important breakdown of the flat plate model in the presences of real airfoil thickness.

A reduction in coherence from 0.85 at α = 0° to 0.1 at α = 16° and a shift from 180° phasing at α = 0° to 0° phasing at α = 16° occurs at 1 to 9% chord. This effect results from the shifting of the stagnation point with angle of attack. As angle of attack is increased the stagnation point moves further down the pressure side of the airfoil (as shown in figure 4.25) and in doing so situates the microphone on the pressure side in front of the stagnation point, in effect placing it in the region of suction side pressure fluctuations. The gradual shift from anti-phasing at α = 0° and 4° to in phasing of across chord pressure fluctuations demonstrates this occurrence nicely. The stagnation point has moved downstream of the 1% chord location at α = 8° at which point the across chord pressure fluctuations begin to shift away from anti-phasing. The further the stagnation point moves down the pressure side of the airfoil the closer the phasing shifts to 0°. In the flat plate model of Amiet pressure fluctuations are taken to be 180° out of phase. The angle of attack induced phase shift demonstrates the invalidity of such formulations in the presence of a real airfoil at angle of attack.

Coherence at 14, 20 and 30% chord reaches a peak level of 0.3 at α = 0° and falls off to zero above ω_r = 20. The phasing of across chord pressure fluctuations at α = 0°, 4° and 8° remain 180° out of phase up to ω_r = 6. Interestingly, at α = 12°, 16°, and 20° the phasing shifts from 0° to 180° and back to 0° with increasing ω_r. As ω_r increases beyond this point the phasing shifts to 0° and coherence falls to less than 0.1.

Where appropriate experimental data has been shown with theoretical calculations. Agreement within 1dB at ω_r < 3 and within 8dB at ω_r > 3 is demonstrated between experimental data at 1% chord for α = 0° and Amiet (1976a, b). The agreement at ω_r < 3 begins to deteriorate as the chord is traversed with Amiet's theory falling increasingly below data at 2.5 to 30% chord where as much as 10dB difference occurs. The agreement at high reduced frequencies (between

10 and 40) is within 4dB at 2.5% and 4% chord. Between 6% and 30% chord the high reduced frequency agreement is within 15dB.

4.9.2 Small Grid

Pressure difference spectra for the small grid are plotted against reduced frequency at 1, 2.5, 4, and 6% chord for all angles of attack in figure 4.62. These spectra are formed in an identical manner as those of the large grid. Coherence and phase of the pressure differenced auto-spectra are shown in figure 4.63 at corresponding chordwise locations for all angles of attack.

The small scale turbulence spectra of figure 4.62 are fairly flat at $\omega_r < 20$ for small angles of attack (<8°), particularly in the leading edge region (1, 2.5% chord). It should be noted that the "spikiness" visible at low reduced frequency is a result of calibration irregularities and not a consequence of airfoil/turbulence interaction. This flattened region, as with the large scale turbulence flow occurs over a similar ω_r range as the flattened region of $|k|$.

As angle of attack is increased the overall level of the spectra begin to rise and become less flat at $\omega_r < 20$. Also, significantly less coherence as compared to large scale turbulence flow is demonstrated between suction and pressure side microphones, particularly at high angles of attack. This increase in spectral level is interesting in that a similar reduction in spectra level with increasing angle of attack, as shown to occur in large scale turbulence flow does not arise. It is at this point where the two distinct interaction regimes are revealed, the reason for which may be suggested by figure 4.57 through the order of magnitude difference in $|k|$. That is, in this flattened region, when the turbulence flow field is comprised primarily of order 10 $|k|$ the potential velocity field produced by the airfoils at angle of attack acts to distort the turbulence in a manner which reduces the magnitude of unsteady pressure fluctuations. As $|k|$ is increased to order 100 the effect is reversed causing an escalation of unsteady pressure fluctuations and, with high enough angle of attack (>8°) the flattened region disappears all together.

The pressure difference phasing (figure 4.63) shows at 1% chord a shift from 180° to 0° phasing with increasing angle of attack as a result of the stagnation point moving off the leading edge. This occurrence remains visible at higher angles of attack at 2.5, 4, and 6% chord. Also interesting to note is the 0° phasing at $\alpha = 0°$ which occurs beyond 1% chord. This seems to be the same type of thickness effect which occurred in the large grid flow although is exaggerated in the small grid flow due to the increased energy content at higher spanwise wavenumbers. As the coherence falls to zero above ω_r = 10 the phasing at all angles of attack becomes erratic as a result of the lack of signal correlation.

Agreement within 5dB between data and Amiet's theory is demonstrated at 1% chord for $\alpha = 0°$ and deteriorates to as much as 15dB as the chord is traversed. The shape of Amiet's theory agrees well at 1 and 2.5% chord although rolls off too quickly with increasing frequency at 4 and 9% chord.

4.10 Unsteady Lift Spectra

Unsteady lift spectra for large and small scale turbulence flows and smooth flow are plotted in figure 4.64 and 4.65 at all angles of attack. The lift spectra of figure 4.64 are composed of the pressure response of microphones from 1 to 85% chord (i.e. all microphones in longest chordwise row) and of figure 4.65 of microphones from 1 to 14% chord. Figure 4.65 has been formed using only microphones to 14% chord for comparison and also out of concern due to uncertainties which arise from integration across the large chordwise microphone separation distances when considering the complete chord lift spectrum. Also, noise from turbulent boundary layer pressure fluctuations and trailing edge separation increase the level of uncertainty in the lift spectra formed by pressure fluctuations occurring along the entire chord. These spectra are created by differencing spanwise averaged pressure spectra across chord and integrating along the chord.

Normal force per unit span =

$$G_{NN}(\omega_r) = \iint G_{\Delta P \Delta P'}(\omega_r, x, x')dx \cdot dx' \qquad (4.13)$$

Tangential force per unit span =

$$G_{TT}(\omega_r) = \iint \left(G_{P1P1'} + G_{P2P2'} + G_{P1P2'} + G_{P2P1'}\right)dz \cdot dz' \qquad (4.14)$$

where, $G_{\Delta P \Delta P'}$ is the cross spectrum between $G_{P1P1'}$ and $G_{P2P2'}$ and prime (') indicates a different chordwise location. Finally, the spectra are rotated from the resulting normal and tangential to chord components into the direction of lift as

$$G_{LL}(\omega_r) = G_{NN}\cos^2(\alpha) + G_{TT}\sin^2(\alpha) - 2\cdot\mathrm{Re}(G_{TN})\cdot\sin(\alpha)\cos(\alpha) \quad [\mathrm{N}^2/\mathrm{m}^2]. \tag{4.15}$$

Figure 4.64 shows considerable 'spikiness' as a result of forming the lift spectra across the entire chord when compared to figure 4.65. The unsteady pressure data from microphones located beyond 30% chord are dominated by boundary layer pressure fluctuations which, when incorporated into the lift spectrum produced considerable discrete frequency variations.

The large grid data of figure 4.64 shows the same trends with angle of attack, namely a decrease in unsteady lift with increasing angle of attack at the unstalled angles as figure 4.65 with the complete chord lift spectra residing a half an order of magnitude higher than the 14% chord lift spectra. In the presence of stall (α = 20°) the large grid lift spectrum of figure 4.64 rises and takes on a significantly different form from the unstalled spectra. This change in spectrum level and shape is not shown in the 14% chord large grid lift spectra (figure 4.65) and demonstrates the majority of unsteady lift is generated beyond 14% chord at stall. This suggests the usage of flat plate theory in the leading edge region may still provide order of magnitude results even in the presence of stall.

The small grid lift spectra of figure 4.64 are similar in shape and approximately an order of magnitude above the 14% chord small grid lift spectra. The complete chord lift spectra show a drop in unsteady lift at $2 < \omega_r < 6$ which must be associated with pressure fluctuations occurring beyond 14% chord. Also, the complete chord lift spectra and 14% chord lift spectra show an increase in unsteady lift with increasing angle of attack

Smooth flow lift spectra of figure 4.64 and 4.65 indicate an increase in unsteady lift of up-to a decade and a half with increasing angle of attack at the unstalled angles of attack (0°, 4°, 8°, 12°) in the low reduced frequency range (<5). The primary contribution to the unsteady lift in this regime is unsteady boundary layer pressure fluctuations. At stalled angles of attack (16° and 20°) an order to an order and a half magnitude jump across the reduced frequency range in unsteady lift is visible as a result of the unsteadiness associated with stall. It is interesting to note the occurrence of more unsteady lift at 16° angle of attack as compared to 20° angle of attack.

For the large scale turbulent flow of figure 4.65 at unstalled angles of attack the lift spectra exhibit a distinct difference in form and up-to 3 decades increase in spectral levels than the smooth flow lift spectra. As angle of attack is increased a reduction in unsteady lift of half a decade of spectral level occurs at ω_r <5. This effect is also demonstrated in the unsteady lift formed by integrating across the entire chord and therefore does not appear to be a local result of leading edge pressure fluctuations. This angle of attack effect is also surprising in light of McKeough's (1976) lift spectra which, as mentioned above exhibit an increase in spectral level with increasing angle of attack. McKeough's turbulence spectra are of similar scale to that of the large grid demonstrating a non-monotonic dependence on turbulence scale. The source of this reduction in spectral level seems to be associated with relative scale of turbulence to airfoil chord and the manner in which this turbulence distorts in the presences of the airfoil mean velocity field at angle of attack.

At ω_r > 20 an increase in unsteady lift with increasing angle of attack is visible. This effect agrees well with the rise in unsteady pressure in the ω_r > 20 region and demonstrates the ability of the mean velocity field to modify the effect of high wavenumber components and increase the magnitude of unsteady lift with increasing angle of attack.

The large scale turbulence flow stalled (20°) unsteady lift spectra are similar in shape and magnitude to the smooth flow 16° angle of attack spectra. This demonstrates the inability of large grid generated turbulence to interact with the large scale fluctuations occurring in the presence of stall. That is, across the reduced frequency range fluctuations related to stall tend to dominate the unsteady lift with the grid generated turbulence producing little effect.

Small scale turbulence lift spectra shown in figure 4.65 maintain at least half decade in magnitude over smooth flow unsteady lift spectra and, again exhibit a form distinctly different from that of the smooth flow (recalling that the small grid flow does not stall at any angle of attack) demonstrating the uncontaminated nature of this data. The "spikiness" visible at ω_r < 3 is related to microphone calibration irregularities.

As angle of attack is increased an overall rise in lift response across the reduced frequency range is demonstrated with up-to a decade increase in magnitude at low reduced frequencies and half a decade of magnitude at high reduced frequencies. This rise in unsteady lift with angle of attack corroborates well with unsteady pressure difference spectra.

Again, the effect of turbulence scale to airfoil chord is revealed by these lift spectra and marks the distinction of the two turbulence/airfoil interaction regimes which occur as discussed above. That is, the full 3-dimensional wavenumber spectrum describing the turbulence of both large and small grid flows are identical in form but differ considerably is scale. The lift spectra of the two flows reveals the mean velocity field's distortion capability and how, at angle of attack the distortion capabilities differ in the two flows.

4.11 Chordwise Cross-Spectra

4.11.1 Large Grid

Normalized chordwise cross-spectra are plotted versus the logarithm of *x/c* for large scale turbulence flow in figure 4.66 at all angles of attack at 4 reduced frequencies (1.1, 2.9, 5.8, and 11.6). These spectra are formed by taking the pressure difference cross-spectrum between the microphone located at 1% chord and all other microphones in the same chordwise row as shown in equation 4.16.

$$G_{\Delta P \Delta P'}\left(\omega_r, x, x', \eta\right) = G_{P1P1'} + G_{P2P2'} - 2\,\mathrm{Re}(G_{P1P2'}) \qquad (4.16)$$

where prime (') indicates a different chordwise location, x = 0.01 (normalized on chord) and x' = all other chordwise locations and η = 0 (recall η is the spanwise separation distance, y_1-y_2) Finally, the normalized cross-spectrum is achieved, as displayed by equation 4.17 by taking the magnitude of the cross-spectrum divided by the auto-spectrum at the 1% chord location.

$$\gamma_{\mathrm{alt}} = \frac{\left|G_{\Delta P \Delta P'}\right|}{G_{\Delta P \Delta P}} \qquad (4.17)$$

Forming the spectra in this manner reveals the amplitude of the unsteady pressure distribution correlating with the leading edge.

At all reduced frequencies (figure 4.66 A, B, C, D) the chordwise γ_{alt} at the unstalled angles of attack tend to band together and fall off linearly (on this log scale) with increasing chord. The roll-off becomes steeper with increasing reduced frequency. This sharp decline reveals the high rate at which unsteady pressure fluctuations correlating with leading edge region drop off. This quick drop in unsteady pressure correlation is a result of a similar interaction which pushes the pressure difference spectra out of 180° phasing. That is, as the chordwise separation distance becomes large the coherence becomes increasingly spatially aliased. The increasingly modified mean velocity field produced by the airfoil as angle of attack is increased appears to have little effect on the interaction of the three wavenumber components with respect to chordwise pressure correlations. Also, note for 16° angle of attack at 1.1 and 2.9 reduced frequency (figure 4.66 A and B) a jump is visible between 5% and 9% chord and may be related to the laminar separation bubble present in this region.

In the case of stalled flow at $\alpha = 20°$ the roll off tends to be slightly steeper than that of the unstalled angles of attack and an increase in γ_{alt} is shown at 20% chord at 5.8 and 11.6 reduced frequency. Also, a rise in γ_{alt} is shown to occur at $\omega_r = 1.1$ beyond 15% chord which is similar in form to the $\alpha = 16°$ γ_{alt}. This low frequency trailing edge rise in correlation may be related to low frequency 'breathing' which occurs in the presence of a large separated flow region. This 'breathing' occurs around the entire airfoil and therefore increases the correlation of trailing edge pressure fluctuations with those occurring at the leading edge.

Amiet's (1976a,b) theory being a 3-d approximate solution is capable of predicting the fall in chordwise coherence as a result of the spatial aliasing. The theory shows a nearly linear decrease (on this log scale) at all reduced frequencies and agrees to within 0.05 γ_{alt} at $\omega_r = 1.1$ up to 6% chord with $\alpha = 0°$ data. The agreement deteriorates at $\omega_r = 2.9$ and 5.8 as the $\alpha = 0°$ data tends to roll off with increasing chord although at $\omega_r = 11.6$ favorable agreement is shown in the first 3% chord. Beyond 10% chord the agreement between Amiet's theory and measured $\alpha = 0°$ data is poor with difference in γ_{alt} of up to 0.25. The poor agreement beyond 10% chord may be a consequence of the airfoils finite thickness which the flat plate model is clearly unable to address.

4.11.2 Small Grid

Small scale turbulence flow normalized cross-spectra are plotted against the logarithm of x/c at 6.1, 31.5, and 59.8 reduced frequency for all angles of attack in figure 4.67. These spectra are formed in a similar manner to those of the large scale turbulence flow.

At $\omega_r = 6.1$ a sharp roughly linear fall-off in γ_{alt} level occurs from 0% to 6% chord. A slight variation with angle of attack is shown to occur manifesting primarily as a faster drop off in chordwise correlation distance. γ_{alt} levels beyond 20% chord are below 0.1 at all angles of attack. At $\omega_r = 31.5$ the correlation at $\alpha = 0°$ is shown to be significant up to 30% chord. As angle of attack is increased the fall-off increases and the extent of chordwise correlation decreases. Little correlation is shown to occur beyond 10% chord in the presence of mean loading. The chordwise correlation shown at ω_r = 59.8 is similar to ω_r = 31.5, showing similar rates of decrease.

Unlike the large grid chordwise correlation the small grid chordwise correlation is affected by angle of attack. This demonstrates the ability of the mean velocity field to distort the incoming turbulence in such a manner as to reduce the chordwise correlation of pressure fluctuations with increasing angle of attack and also serves to denote the two turbulence/airfoil interaction regimes which arise in the two different turbulence scale flows.

Also interesting to note is the small grid chordwise correlation at ω_r = 6.1 which falls off nearly twice as fast as the large grid chordwise pressure correlation at ω_r = 5.8. The higher average wavenumber magnitude of the small grid flow implies a dominance of smaller scale turbulence which produce spatial aliasing at relatively small separations and therefore result in the increase rate of decay of chordwise pressure correlation.

Agreement with Amiet's (1976a,b) theory is within 0.15 γ_{alt} at ω_r = 31.5 and 59.8 across much of the chord for $\alpha = 0°$. The agreement is within 0.15 γ_{alt} in the leading edge region at ω_r = 6.1 although the theory does not tend to decrease at the same rate as the data. The differences shown between the data and Amiet's theory again appear to be a result of the airfoils finite thickness.

4.12 Spanwise Cross-spectra

4.12.1 Large Grid

The large scale turbulence flow coherence between pressure difference fluctuations as a function of spanwise separation (η/c) are plotted at 2.5% and 6% chord for 0.57, 2.9, 5.8, and 22.6 reduced frequency at all angles of attack in figure 4.68 and 4.69 respectively. Coherence is defined as

$$\gamma = \sqrt{\frac{\left|G_{\Delta P \Delta P'}\right|^2}{G_{\Delta P \Delta P} \cdot G_{\Delta P' \Delta P'}}} \tag{4.18}$$

where,

$$G_{\Delta P \Delta P'}(\omega_r, \eta) = G_{P1P1'} + G_{P2P2'} - 2\,\mathrm{Re}(G_{P1P2'}) \tag{4.19}$$

and prime (') indicates a different spanwise location.

Coherence at $\omega_r = 1.1$ of figure 4.68A demonstrates a smooth roll-off for $\alpha = 0°$ and 4°. The roll-off of coherence with increasing spanwise separation is an expected occurrence and is a similar phenomenon to that revealed by the chordwise unsteady pressure correlation. Mugridge (1970), in his formulation of the skewed incompressible gust solution showed this effect. He noted that as the spanwise wavelength of the gust becomes small compared to the span cancellation of surface pressure fluctuations occurs. As angle of attack is pushed higher the roll-off becomes sharper and less smooth. This effect is a result of boundary layer pressure fluctuations. This phenomenon therefore tends to produce a quick drop in coherence following by a small jump back up in coherence as turbulence/airfoil interaction pressure fluctuations begin to correlate all occurring over the small spanwise separation region. Outside of the small separation region coherence levels decrease with increasing angle of attack at the unstalled angles of attack. This angle of attack effect suggests that the distortion of turbulence, in particular stretching of eddies around the leading edge by the mean field acts to suppress the correlation of pressure fluctuations over large separations.

Coherence curves at 6% chord (figure 4.69A) demonstrates similar trends in shape as those at 2.5% chord although correlating over a larger separation extent.

Coherence at 2.5% chord at 2.9 reduced frequency (figure 4.68B) behaves in a similar manner as those of $\omega_r = 1.1$. The coherence of $\alpha = 0°$, 4° and 8° demonstrate a smooth roll-off and band tightly together. At $\alpha = 12°$ a spike is present below $\eta/c = 0.01$ and the roll-off sharpens. A similar phenomenon is visible at $\alpha = 16°$ below $\eta/c = 0.05$ both of which appear to be a result of boundary layer pressure fluctuation correlation. The stalled angle of attack rolls off to less than 0.2 by $\eta/c = 0.2$ significantly deviating from the unstalled angles of attack. The sharp decrease in coherence at the stalled angle of attack indicates a significant modification of the turbulence in the presence of the stalled mean velocity field.

The unstalled angles of attack at 6% chord at $\omega_r = 2.9$ (figure 4.69B) band together with exception $\alpha = 16°$ which deviates as much as 0.1 in level for small (<0.5) separations. At stall ($\alpha = 20°$) the coherence level falls of to less than 0.2 by $\eta/c = 0.13$ and then levels off as pressure fluctuations resulting from stall begin to correlate over large spanwise separations.

At $\omega_r = 5.8$ the coherence at 2.5% chord (figure 4.68C) exhibits a smooth roll-off at $\alpha =$ 0° and 4°, both of which band tightly together while $\alpha = 8°$, 12° and 16° show a spike at very small spanwise separations related to boundary layer pressure fluctuation correlation and roll-off sharper with increasing angle of attack. 20° angle of attack behaves similar to that at ω_r = 2.9, rolling off very quickly with increasing spanwise separation.

Similar spikes resulting from turbulent boundary layer pressure fluctuations are visible at 6% chord at ω_r =5.8 (figure 4.69C) for all unstalled angles of attack. The boundary layer, as shown in figure 4.25 is turbulent or nearing turbulent on the pressure side of the airfoil at all angles of attack. At stall the level of coherence behaves very near that shown at 2.5% chord although tending to decrease slightly faster.

The coherence of ω_r = 11.6 at 2.5% chord (figure 4.68D) drops off sharply at α = 0°, falling to a coherence of 0.2 by η/c = 0.2 and the rate of decrease increases with angle of attack. The formation of a spike followed by a small jump up in coherence at small spanwise separations visible at α = 4°, 8°, 12°, and 16° indicates the correlation of boundary layer pressure fluctuations.

The data at 6% chord for ω_r =11.6 (figure 4.69D) shows higher levels of uncertainty as well as correlation of boundary layer pressure fluctuations which produce a sharp spike at small spanwise separations at all angles of attack. As a consequence of turbulent boundary layer pressure fluctuations the overall level of coherence is reduced at each angle of attack as compared to coherence levels at 2.5% chord (figure 4.68D).

Amiet's (1976a,b) theory agrees nearly exactly with data at α = 0° for ω_r = 5.8 and 11.6 across the η/c range (figures 4.68C and 4.69C). Agreement between theory and measurement deviate, with theory falling below data by as much as 0.15 at ω_r = 1.1 and 2.9 in the η/c < 0.3 extent at both chordwise locations. The general trend and shape of the correlation is duplicated by Amiet's theory with overall reasonable agreement in the case of no mean loading. The airfoil thickness and distortion it produces through the mean velocity field therefore seem to have only a minor impact on spanwise correlation.

4.12.2 Small Grid

The small scale turbulence flow coherence are plotted versus η/c at ω_r = 3.05 and 6.1, 31.5, and 59.8 for all angles of attack in figure 4.70. The spectra are formed in a similar manner as those of the large scale turbulence flow.

At ω_r = 3.05 and 6.1 the correlation remains above γ = 0.2 up to η/c = 0.15. The roll off is sharper, falling to less than 0.1 at η/c = 0.02 for α = 8°, 12°, 16°, and 20°. The rather quick roll off visible at all angles of attack results from the high wavenumber dominated small scale flow. In addition, the presence of turbulent boundary layer pressure fluctuations will tend to lower the level of coherence between microphones.

Coherence levels drop off very quickly at ω_r = 31.5 and 59.8, falling to γ < 0.2 by η/c = 0.05. Measurements for all angles of attack tend to band together with the only deviation occurring above α = 8° at which point the thickened boundary layer cause a correlation of boundary layer pressure fluctuations which manifests through the spike present at η/c = 0.025.

Amiet's (1976a,b) theory shows γ up to 0.35 greater than α = 0° data and decreases at a similar rate for ω_r = 3.05. At ω_r = 6.1 theory γ is 0.25 greater than α = 0° data for η/c < 0.05 and tends to decrease at a faster rate. Theory falls below the measurement beyond η/c > 0.05 with as much at 0.18 difference in coherence levels. The prediction falls off at a much slower rate at ω_r = 31.5 and 59.7 with up to a 0.7 difference in coherence levels. In general the theory tends to predict the spanwise correlation well at low frequencies, holding the shape and level within reasonable agreement to that measured.

Chapter 5. Conclusions

A NACA 0015 airfoil has been instrumented with 96 pressure sensing microphones to allow detailed surface pressure measurements. The calibrated airfoil system was installed in the Virginia Tech stability wind tunnel and surface pressure measurements made in two grid generated homogenous flows (L/r_c = 5.41 and 0.519) at Re = 1.17 x 10^6 for α = 0°, 4°, 8°, 12°, 16°, and 20°. The goal of this measurement was to reveal and highlight mean loading and turbulence scale effects on surface pressure fluctuations resulting from turbulence/airfoil interaction.

A) In the large scale flow (L/r_c = 5.41) mean and unsteady pressure measurements show an unstalled flow field from α = 0° to 16° with a small laminar separation bubble developing in the leading edge region and some separation in the trailing edge region at α = 16°. At α = 20° the airfoil is shown to be completely stalled.

B) In the small scale flow (L/r_c = 0.519) mean and unsteady pressure measurements show no stall occurring at any angle of attack. Separation is shown to occur in the trailing edge region at α = 20°.

C) Matched flow speed and RPM unsteady pressure measurements demonstrate low pressure difference spectral levels indicating turbulence/airfoil interaction pressure fluctuations are dominant in the measurement.

D) The surface pressure response shows a dependance on angle of attack the nature of which is related to the relative chord/turbulence scale. The dependance on turbulence scale appears to be non-monotonic based on the following;

1. A 4dB reduction of pressure difference spectra level in the ω_r < 4 region at 1, 2.5, 4, and 14% chord is shown to occur in the large grid flow. The source of this reduction is related to the distortion of incoming turbulence
2. As angle of attack is increased the overall level of small grid pressure difference spectra begin to rise as much as 18dB and become less flat at ω_r < 20. The modification of incoming turbulence by the mean field seems to produce this increase in spectral level.
3. As angle of attack is increased a reduction in unsteady lift of half a decade of spectral level occurs at ω_r <5 in the large grid flow. The source of this reduction seems to be associated

with the manner in which this turbulence distorts in the presences of the airfoil mean velocity field at angle of attack.

4. As angle of attack is increased an overall rise in lift response across the reduced frequency range is demonstrated with up-to a decade increase in magnitude at low reduced frequencies and half a decade of magnitude at high reduced frequencies in the small grid flow.

E) Also, an overlap region exists where the two different scale flows begin to produce similar effects on the surface pressure with increasing angle of attack. This conclusion is based on the following;

1. In the large grid flow at ω_r > 10 range, an increase in pressure difference spectral level of up-to 10dB is shown with increasing angle of attack. The cause of this rise appears to be related to the distortion of incoming turbulence.

F) For small values of k_1 the turbulence flow field appears similar to the airfoil in the large grid flow and at $\alpha = 0°$ and 4° in the small grid flow based on

1. The pressure difference spectra of the large grid flow exhibit a flattened region extending to ω_r = 3 for all unstalled angles of attack and all chordwise stations which extends over a similar range as the flatten region of $|k|$.
2. The small scale turbulence spectra of the small grid flow are fairly flat at ω_r < 20 for small angles of attack (<8°), particularly in the leading edge region (1, 2.5% chord).

G) Also, the interaction of the full 3-dimensional wavenumber spectrum affects the distance over which pressure fluctuations correlate and the extent of correlation is affected by angle of attack. This is based on the following;

1. At all reduced frequencies the chordwise normalized cross-spectra at the unstalled angles of attack tend to band together and drop off quickly with increasing chord in the large grid flow.
2. The roll-off of chordwise correlation at ω_r =3.1 and 31.5 occurs over a small chordwise distance in the small grid flow. The roll-off rate increases with increasing angle of attack.
3. At all ω_r a smooth decrease in spanwise coherence occurs and a reduction in level with increasing angle of attack is visible. The mean velocity field's ability to distort the turbulence in a manner which reduces the spanwise correlation is demonstrated. This effect is revealed in both large and small scale flows.

H) The theory of Amiet (1976a,b) does not predict well the pressure difference phase shift from 180° to 0° which occurs at $\omega_r > 10$ in large grid flow and at $\omega_r > 20$ in the small grid flow as a result of spanwise and lateral wavenumber interaction with streamwise wavenumbers.

I) Amiet's (1976a,b) theory agrees favorable with measured pressure difference spectra at $\alpha = 0°$ in the leading edge region with agreement deteriorating as the chord is traversed based on the following

1. Large grid measured pressure difference spectra agree with Amiet (1976a, b) within 1dB at $\omega_r < 3$ and within 8dB at $\omega_r > 3$ at 1% chord for $\alpha = 0°$. The agreement at $\omega_r < 3$ begins to deteriorate as the chord is traversed with Amiet's theory falling increasingly below data at 2.5 to 30% chord where as much as 10dB difference occurs. The agreement at high reduced frequencies (between 10 and 40) is within 4dB at 2.5% and 4% chord. Between 6% and 30% chord the high reduced frequency agreement is within 15dB.
2. Agreement within 5dB between small grid data and Amiet's theory is demonstrated at 1% chord for $\alpha = 0°$ and deteriorates to as much as 15dB as the chord is traversed. The shape of Amiet's theory agrees well at 1 and 2.5% chord although rolls off too quickly with increasing frequency at 4 and 9% chord.

J) Amiet's (1976a,b) chordwise correlation shows reasonable agreement with measurements in the leading edge region although tends to over predict the correlation at large chordwise separations. This is based on the following

1. Amiet's (1976a,b) theory shows a nearly linear decrease (on this log scale) at all reduced frequencies and agrees to within 0.05 γ_{alt} at $\omega_r = 1.1$ up to 6% chord with $\alpha = 0°$ data. The agreement deteriorates at $\omega_r = 2.9$ and 5.8 as the $\alpha = 0°$ data tends to roll off with increasing chord although at $\omega_r = 11.6$ favorable agreement is shown in the first 3% chord.
2. Agreement with Amiet's (1976a,b) theory is within 0.15 γ_{alt} at $\omega_r = 31.5$ and 59.8 across much of the chord for $\alpha = 0°$. The agreement is within 0.15 γ_{alt} in the leading edge region at $\omega_r = 6.1$ although the theory does not tend to decrease at the same rate as the data.

K) Amiet's (1976a,b) theory nearly exactly predicts the spanwise correlation at higher reduced frequencies in the presence of large grid flow and shows favorable agreement at low reduced frequencies in the presences of small grid flow. This is based on the following

1. Amiet's (1976a,b) theory agrees nearly exactly with large grid data at $\alpha = 0°$ for $\omega_r = 5.8$ and 11.6 across the η/c range. Agreement between theory and measurement deviate, with theory falling below data by as much as 0.15 at $\omega_r = 1.1$ and 2.9 in the $\eta/c < 0.3$ extent. The general trend and shape of the correlation is duplicated by Amiet's theory with overall reasonable agreement in the case of no mean loading. The airfoil thickness and distortion it produces through the mean velocity field therefore seem to have only a minor impact on spanwise correlation.
2. Amiet's (1976a,b) theory shows γ up to 0.35 greater than $\alpha = 0°$ small grid data and decreases at a similar rate for $\omega_r = 3.05$. At $\omega_r = 6.1$ theory γ is 0.25 greater than $\alpha = 0°$ data for $\eta/c < 0.05$ and tends to decrease at a faster rate. Theory falls below the measurement beyond $\eta/c > 0.05$ with as much at 0.18 difference in coherence levels. The prediction falls off at a much slower rate at $\omega_r = 31.5$ and 59.7 with up to a 0.7 difference in coherence levels. In general the theory tends to predict the spanwise correlation well at low frequencies, holding the shape and level within reasonable agreement to that measured.

References

Adamczyk J J, 1974, "Passage of a swept airfoil through an oblique gust", Journal of Aircraft, vol. 11, no. 5, pp. 281-287.

Adamcyzk J J, and Brand R S, 1972, "Scattering of sound by an airfoil of finite span in a compressible stream", Journal of Sound and Vibration, vol. 25, no. 1, pp. 139-156.

Allen H J and Vincenti W G, 1944, “Wall Interference in a Two-Dimensional-Flow Wind Tunnel with Consideration of the Effects of Compressiblity”, NASA TR 782.

Amiet R K, 1974, "Compressibility effects in unsteady thin airfoil theory", AIAA Journal, vol. 12, no. 2, pp 252-255

Amiet R K, 1975, "Acoustic radiation from an airfoil in a turbulent stream", Journal of Sound and Vibration, vol. 41, no. 4, pp. 407-420.

Amiet R K, 1976b, “Airfoil Response to an Incompressible Skewed Gust of Small Spanwise Wave-Number”, AIAA Journal, vol. 14, no. 4, pp. 541-542.

Amiet R K, 1976a, "High-frequency thin airfoil theory for subsonic flow", AIAA Journal, vol. 14, no. 8, pp. 1076-1082.

Amiet R K and Sears W R, 1979, “The Aerodynamic Noise of Small Perturbation Subsonic Flow”, Journal of Fluid Mechanics, vol. 44, pt. 2, pp. 227-235.

Aravamudan K S and Harris W L, 1979, "Low frequency broadband noise generated by a model rotor", Journal of the Acoustical Society of America, vol. 66, no. 2, pp. 522-533.

Atassi H M, Dusey M and Davis C, 1993a, "Acoustic radiation from a thin airfoil in non-uniform subsonic flows, AIAA Journal", vol. 31, pp. 12-19.

Atassi H M, Fang J and Patrick S, 1993b, "Direct calculation of sound radiated from bodies in non-uniform flows, Journal of Fluids Engineering", vol. 115, pp. 573-579, December.

Atassi H M and Grzedzinski J, "Unsteady disturbances of streaming motions around bodies", Journal of Fluid Mechanics, vol. 209, pp. 385-403, 1989.

Barlow J B, Rae W H, and Pope A, 1999, “Low-Speed Wind Tunnel Testing”, John Wiley & Sons, 3rd edition, pp.353-361.

Bereketab S, Wang H, Mish P and Devenport W J, 2000, "The Surface Pressure Response Of A NACA 0015 Airfoil Immersed In Grid Turbulence. Volume 1: Characteristics of the turbulence", Final report to NASA Langley under grant NAG 1-1942, AOE Dept., Virginia Tech.

Blake W K, 1986, *Mechanics of Flow Induced Vibrations*, vol. II, pp. 735-756, Academic Press, New York.

Choi K and Simpson R L, 1987, "Some mean velocity, turbulence and unsteadiness characteristics of the Virginia Tech Stability Wind Tunnel", Report VPI-AOE-161, Virginia Tech, Blacksburg VA.

Commerford G. L. and Carta F. O., 1970, "An exploratory investigation of the unsteady aerodynamic response of a two-dimensional airfoil at high reduced frequency", United Aircraft Research Laboratories, East Hartford, Connecticut, Report UAR-J182.

Commerford G L and Carta F. O., 1973, "Unsteady Aerodynamic Response of a Two Dimensional Airfoil at High Reduced Frequency", AIAA Journal, Vol 12, No.1, pp. 43-48.

Fang J and Attassi H M, 1993, "Numerical solutions for unsteady subsonic vortical flows around loaded cascades", Journal of Turbomachinery, vol. 115, pp. 810-816.

Filotas L T, 1969, "Response of an infinite wing to an oblique sinusoidal gust", Basic Aerodynamic Noise Research, pp. 231-246.

Fleeter S, Capece V, and Chiang H D, 1989, "Unsteady Aerodynamic Gust Response Including Steady Flow Separation", AIAA Journal, Vol 28, No. 6, pp 1024-1031.

Fujita H and Kovasznay L G, 1974, "Unsteady Lift and Radiated Sound from a Wake Cutting Airfoil", AIAA Journal, Vol 12, No. 9, pp. 1216-1221.

Goldstein M E and Attassi H, 1976, "A complete second order theory for the unsteady flow about an airfoil due to a periodic gust", Journal of Fluid Mechanics, vol. 74, pt. 4, pp. 741-765.

Graham J M R, 1970a, "Lifting surface theory for the problem of an arbitrarily yawed sinusoidal gust incident on a thin airfoil in incompressible flow", Aeronautical Quarterly, May, pp. 182-198.

Graham J M R, 1970b, "Similarity rules for thin airfoils in non-stationary subsonic flows", Journal of Fluid Mechanics, vol. 43, pt. 4, pp. 753-766.

Graham J M R and Kullar I, 1977, "Small perturbation expansions in unsteady airfoil theory", Journal of Fluid Mechanics, vol. 83, part 2, pp. 209-224.

Hall K C and Verdon J M, 1991, "Gust response analysis for cascades operating in non-uniform mean flows", AIAA Journal, vol. 29, no. 9, pp. 1463-1471.

Henderson G H and Fleeter S, 1993a, "Forcing function effects on unsteady aerodynamic gust response. Part 2 - Low solidity airfoil response", Journal of Turbomachinery, vol. 115, pp. 751-759.

Henderson G H and Fleeter S, 1993b, "Airfoil wake and linear theory gust response including sub and super-resonant flow conditions", Journal of Propulsion and Power, vol. 9, no. 6 (Nov Dec), pp. 847-857.

Henderson G H and Fleeter S, 1997, "Vortical gust response of a low solidity vane row including steady loading and dynamic stall effects", Journal of Turbomachinery, vol. 119, July, pp. 482-490.

Horlock J H, 1968, "Fluctuating lift forces on airfoils moving through transverse and chordwise gusts", Journal of Basic Engineering, vol. 90, pp. 494-500.

Humbad N G and Harris W L, 1980, "Model rotor low-frequency broadband noise at moderate tip speeds", AIAA paper 80-1013.

Humbad N G and Harris W L, 1981, "Tip geometry effects on model helicopter rotor low frequency broadband noise", AIAA 7th Aeroacoustics conference, October 5-7, Palo Alto, CA, AIAA-81-2003.

Jackson R, Graham J M R and Maull D J, 1973, "The lift on a wing in a turbulent flow", Aeronautical Quarterly, vol. 24, pp. 155-166.

Kemp N H, 1952, "On the lift and circulation of airfoils in some unsteady-flow problems", Journal of the Aeronautical Sciences, vol. 19, pp. 713-714.

Landahl M, “Unsteady Transonic Flow”, Pergamon Press, New York, 1961, pp. 27-30.

Larssen J V and Devenport W J, 1999, "Acoustic Properties of the Virginia Tech Stability Wind Tunnel", Rept. VPI-AOE-263, AOE Dept., Virginia Tech, avail. *http://www.aoe.vt.edu/aoe/physical/vpi-aoe-263.pdf*

Liepman H W, 1955, "Extension of the statistical approach to buffeting and gust response of wings of finite span", Journal of the Aeronautical Sciences, vol. 22, pp. 197-200.

Lorence C B and Hall K C, 1996, "Sensitivity analysis of the aeroacoustic response of turbomachinery blade rows", AIAA Journal, vol. 34, no. 8, August, pp. 1547-1554.

Manwaring S R and Fleeter S, 1993, "Rotor blade unsteady aerodynamic gust response to inlet guide vane wakes", Journal of turbomachinery, vol. 115, pp. 197-206.

Martinez R and Widnall A E, 1980, "Unified aerodynamic-acoustic theory for a thin rectangular wing encountering a gust", AIAA Journal, vol 18, no. 6, June, pp. 636-645.

Maskell E C, 1965, “A Theory of the Blockage Effects on Bluff Bodies and Stalled Wings in a Closed Wind Tunnel”, ARC R&M 3400.

McKeough P J, 1976, "Effects of turbulence on aerofoils at high incidence", Ph.D. Dissertation, University of London.

McKeough P J and Graham J M R, 1980, "The effect of mean loading on the fluctuating loads induced on aerofoils by a turbulent stream", The Aeronautical Quarterly, vol. 31, pp. 56-69.

Miles J W, 1950, “Quasi-Stationary Airfoil Theory in Subsonic Compressible Flow”, Quarterly of Applied Mathematics, vol. 8, pp 181.

Morfey P C, 1970, "Lift fluctuations associated with unsteady chordwise flow past an airfoil", ASME Journal of Basic Engineering, vol. 92, pp. 663-665.

Mugridge B D, 1970, "Sound radiation from airfoils in turbulent flow", Journal of Sound and Vibration, vol. 13, pp. 362-363.

Myers M and Kershen E J, 1995, "Influence of incidence angle on sound generation by airfoils interacting with high frequency gusts", Journal of Fluid Mechanics, vol. 292, pp 271-304.

Osborne C, 1971, “Compressibility Effects in the Unsteady Interaction Between Blade Rows”, Ph.D. thesis, Graduate School of Aerospace Engineering, Cornell Univ, Ithaca, N.Y.

Osborne C, 1973, "Unsteady thin-airfoil theory for subsonic flow", AIAA Journal, vol. 11, no. 2, pp. 205-209.

Patterson R W and Amiet R K, 1976a, "Acoustic radiation and surface pressure characteristics of an airfoil due to incident turbulence", NASA CR 2733.

Patterson R W and Amiet R K, 1976b, "Acoustic radiation and surface pressure characteristics of an airfoil due to incident turbulence", 3rd AIAA Aero-Acoustics Conference, Palo Alto, CA, July 20-23, 1976, AIAA paper 76-571.

Reissner E, 1951, "On the application of Mathieu functions in the theory of subsonic compressible flow past oscillating airfoils", NACA TN 2363.

Ribner H S, 1956, “Statistical Theory of Buffeting and Gust Response: Unification and Extension”, Journal of Aeronautical Sciences, vol. 23, pp 1075-1118.

Satyanarayana B, Henderson R E, Gostelow J P, 1974, “A Comparison Between Experimental and Theoretical Fluctuating Lift on Cascades at Low Frequency Parameters”, ASME

Schwartzschild K, “Die Beugung und Polarisation des Lichts durch einen Spalt-I”, Mathematische Annalen, Vol. 55, 1902, pp. 177-247.

Scott J R, Ph.D. dissertation, University of Notre Dame, April 1990 (unpublished)

Scott J R and Atassi H M, 1995, "A finite-difference, frequency domain numerical scheme for the solution of the gust response problem", Journal of Computational Physics, vol. 119, pp75-93.

Sears W R, 1941,"Some aspects of non-stationary airfoil theory and its practical application", Journal of the Aeronautical Sciences, vol. 18, no. 3, pp. 104-108.

Sing C and Widnall S, 1974, “Prediction of Unsteady Airloads for Oblique Blade-Gust Interaction in Compressible Flow”, AIAA Journal, vol. 12, no. 9, pp. 1228-1235.

Van Driest E R and Blumer C B, 1963, “Boundary Layer Transition, Free Stream Turbulence, and Pressure Gradient Effects”, AIAA Journal, Vol. 1, pp. 1303-1306.

von Karman T and Sears W R, 1938, "Airfoil theory for non-uniform motion", Journal of the Aeronautical Sciences, vol. 5, no. 10, pp. 379-390.

Williams M and Harris W L, 1984, "Helicopter rotor broadband noise due to rotor-turbulence interaction", FDRL Report 84-1, Department of Aeronautics and Astronautics, MIT.

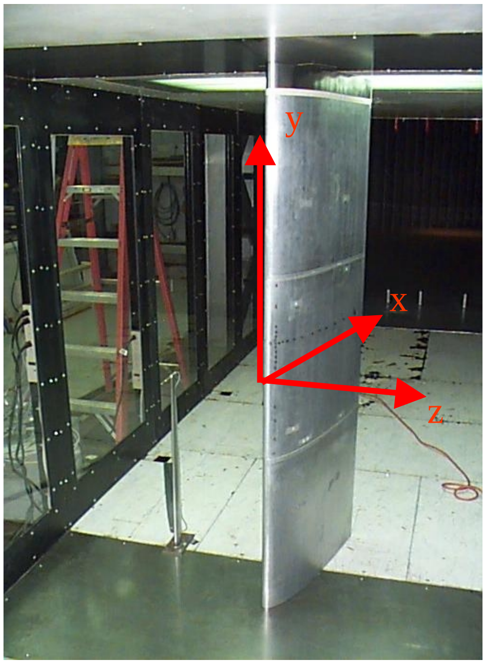

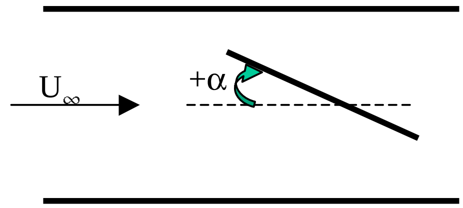

Figure 4.2: Top down view of airfoil in wind tunnel test section defining positive angles of attack

Figure 4.1: Coordinate system

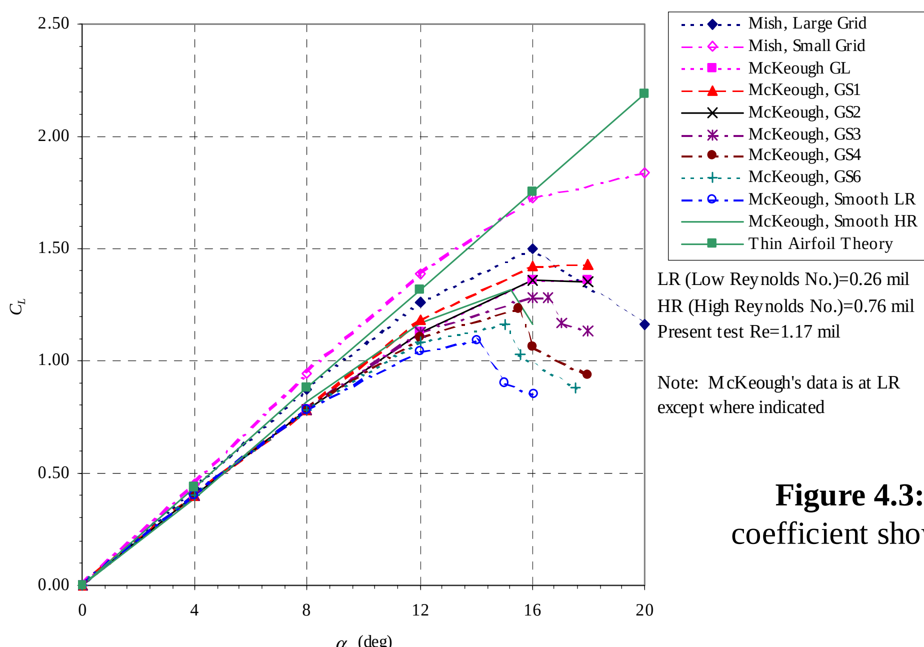

Figure 4.3: Mean pressure calculated lift coefficient shown with McKeough's (1976) data

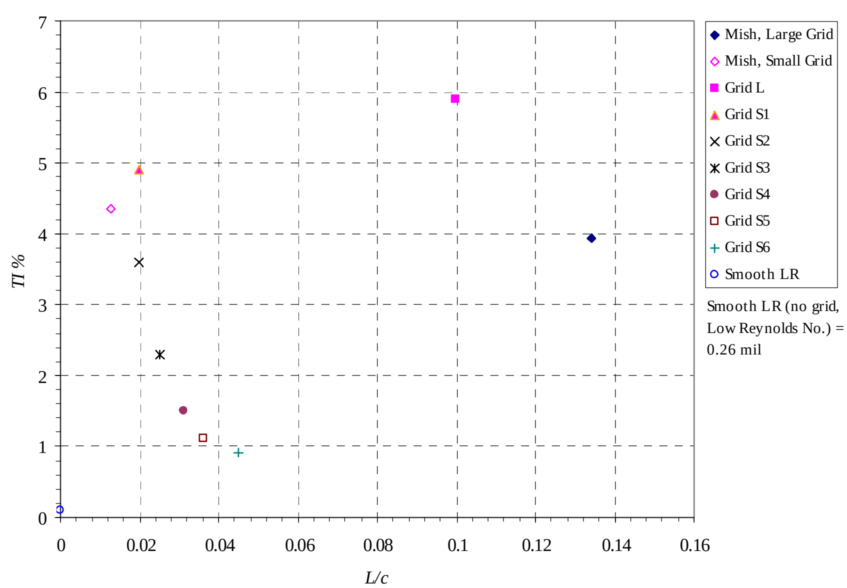

Figure 4.4: Turbulence intensity versus length scale normalized on chord from McKeough (1976) and the present experiment

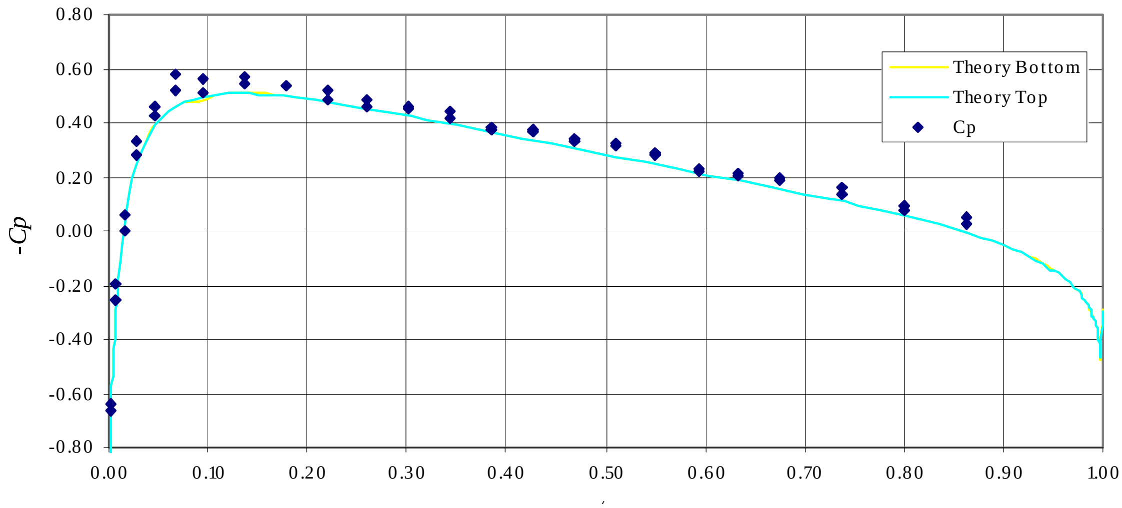

Figure 4.5: Large grid mean pressure at 0° AoA

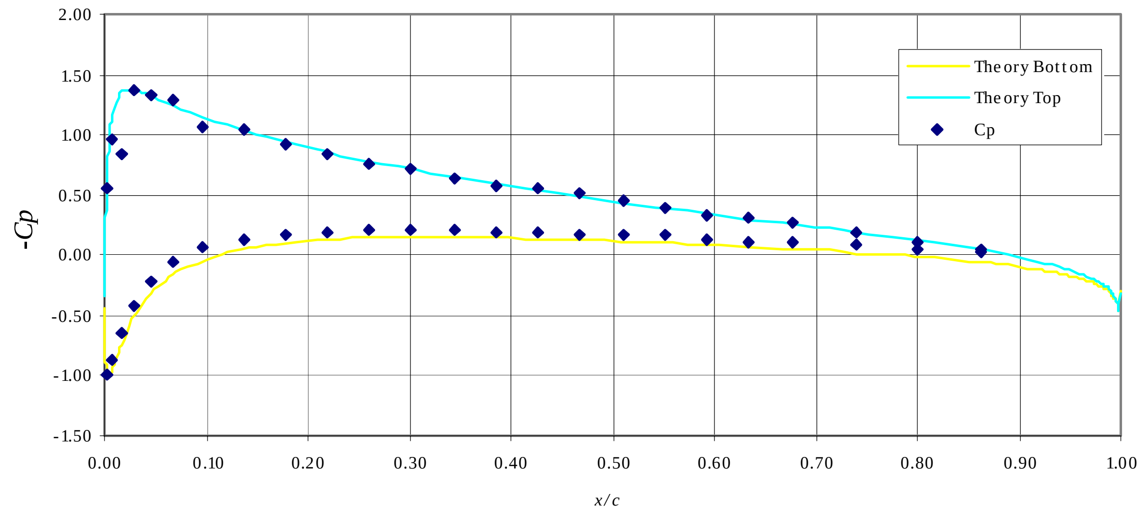

Figure 4.6: Large grid mean pressure at 4° AoA

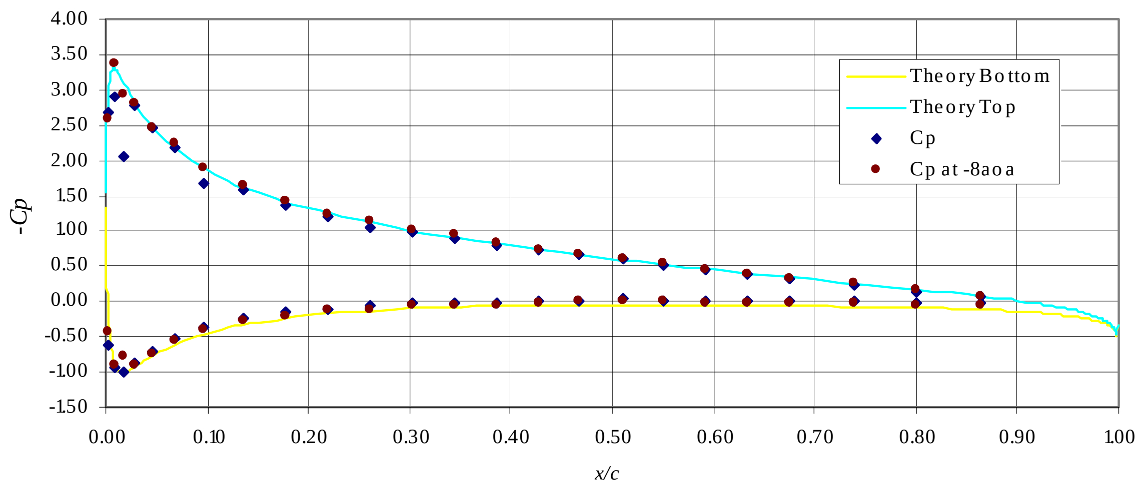

Figure 4.7: Large grid mean pressure at 8° AoA

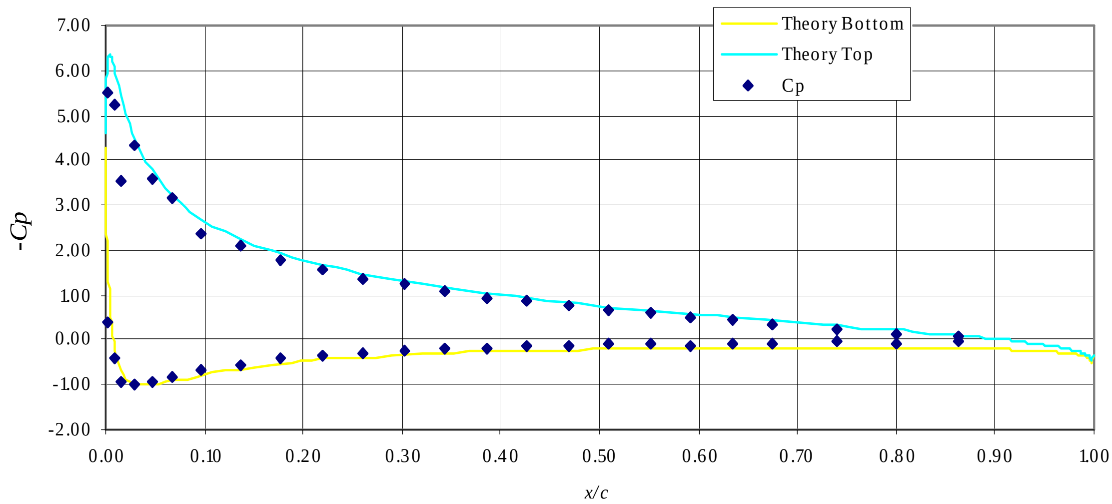

Figure 4.8: Large grid mean pressure at 12° AoA

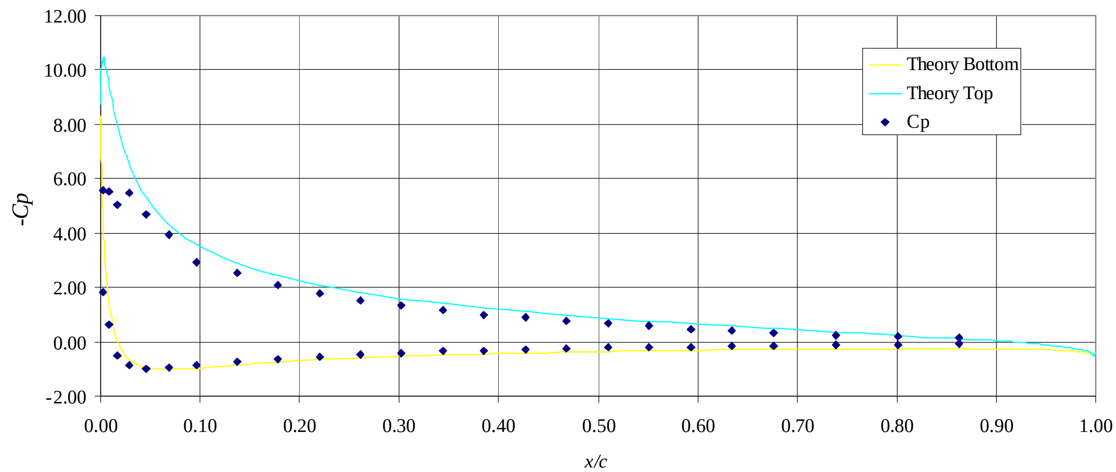

Figure 4.9: Large grid mean pressure at 16° AoA

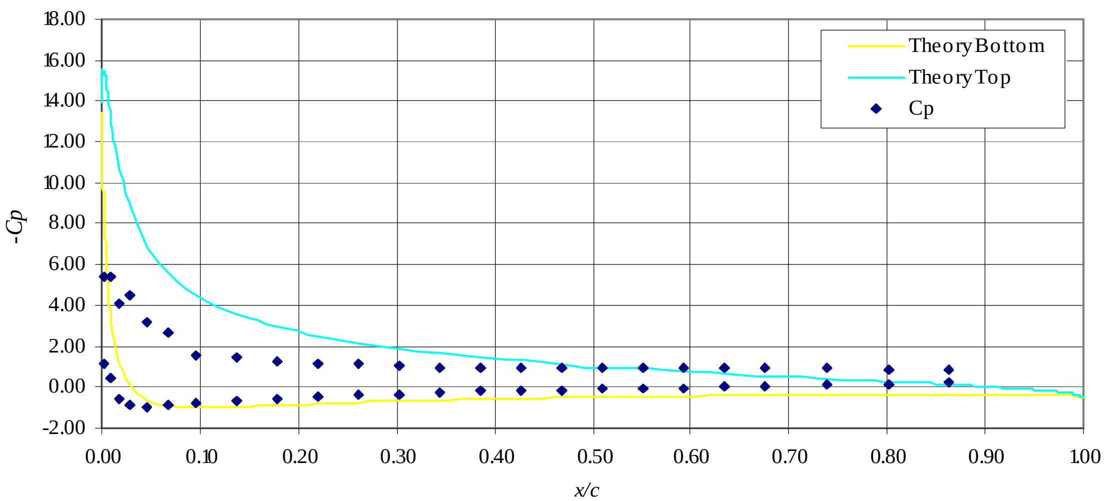

Figure 4.10: Large grid mean pressure at 20° AoA

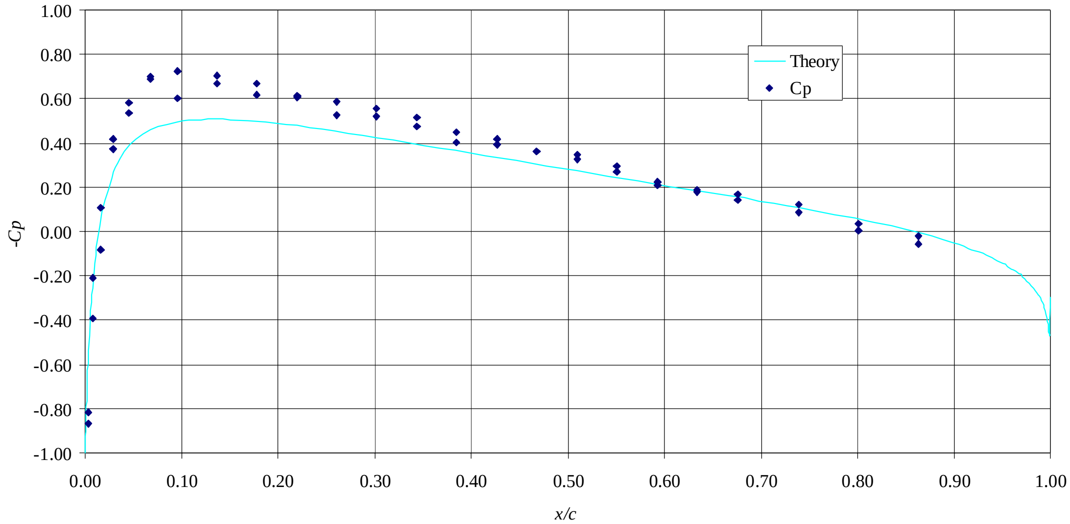

Figure 4.11: Small grid mean pressure at 0° AoA

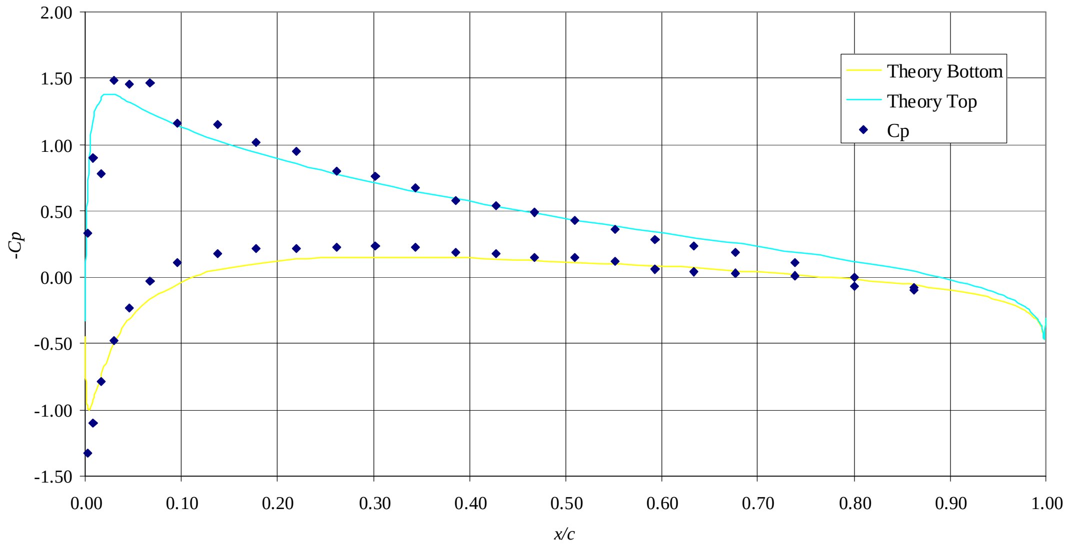

Figure 4.12: Small grid mean pressure at 4° AoA

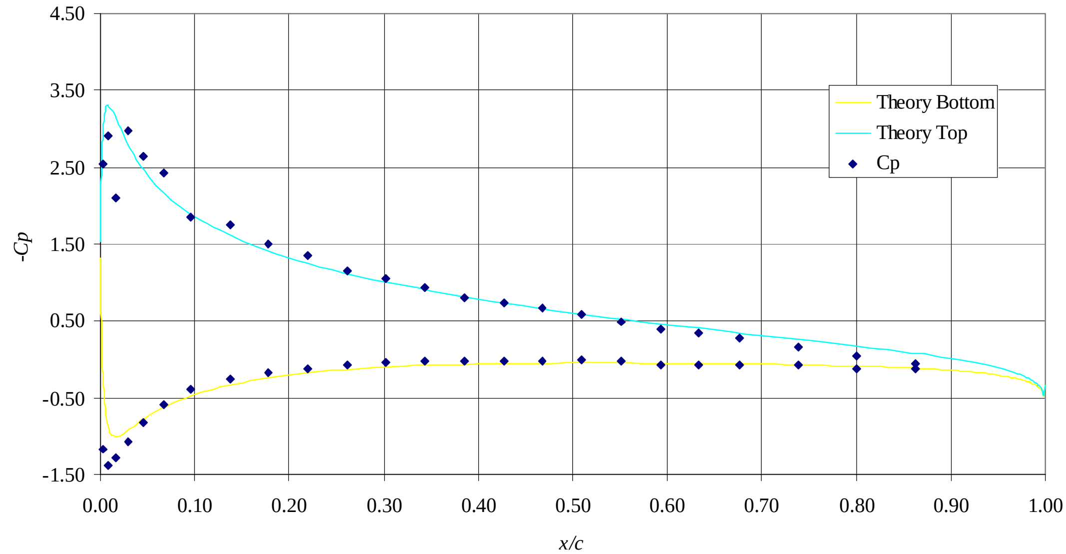

Figure 4.13: Small grid mean pressure at 8° AoA

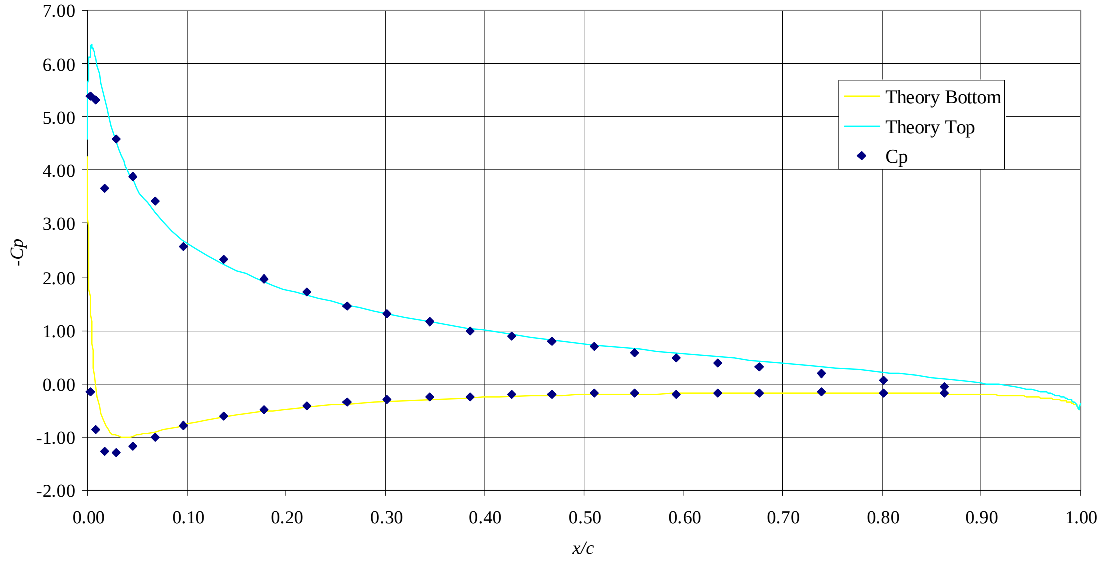

Figure 4.14: Small grid mean pressure at 12° AoA

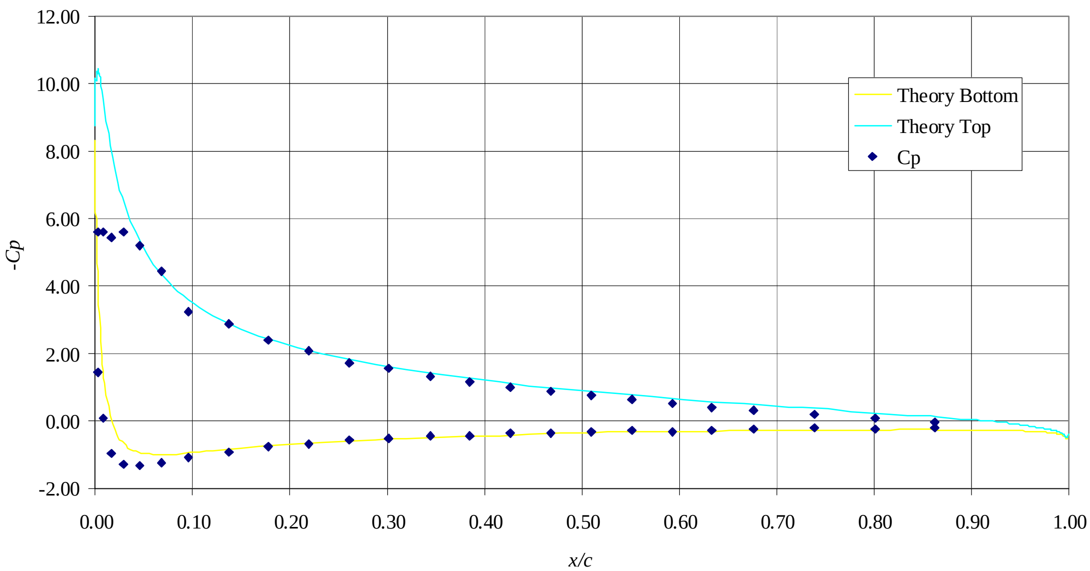

Figure 4.15: Small grid mean pressure at 16° AoA

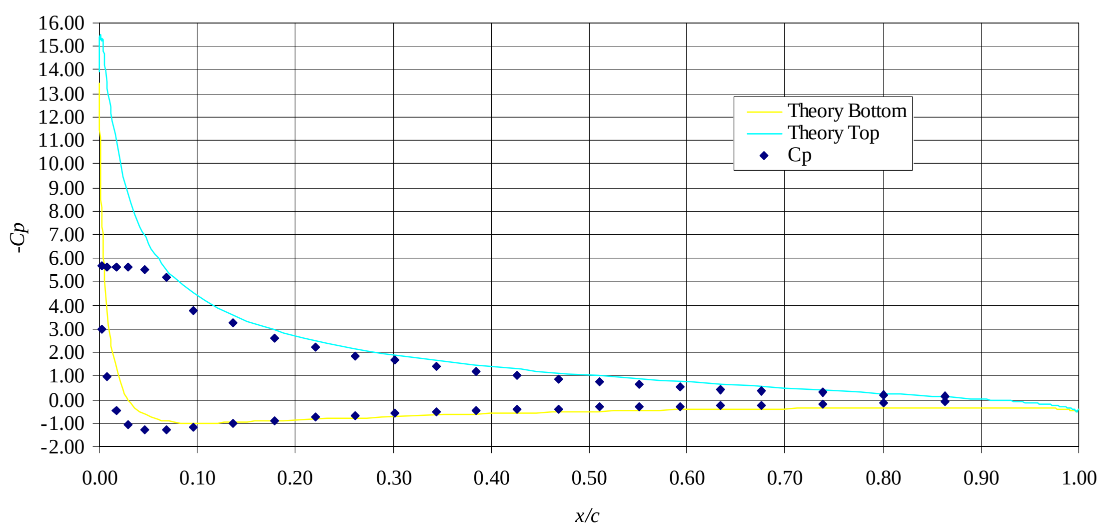

Figure 4.16: Small grid mean pressure at 20° AoA

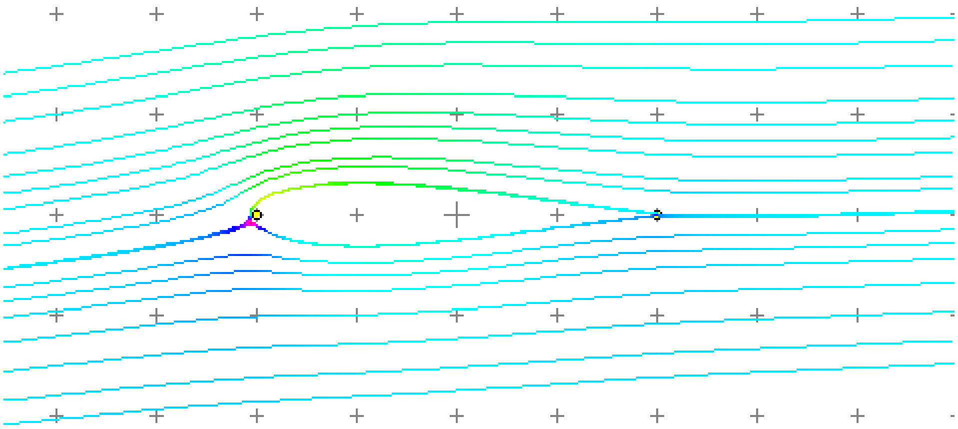

Figure 4.17: 15% thick Joukowski airfoil at $\alpha = 4°$ showing streamlines used to calculate upstream influence on the small grid

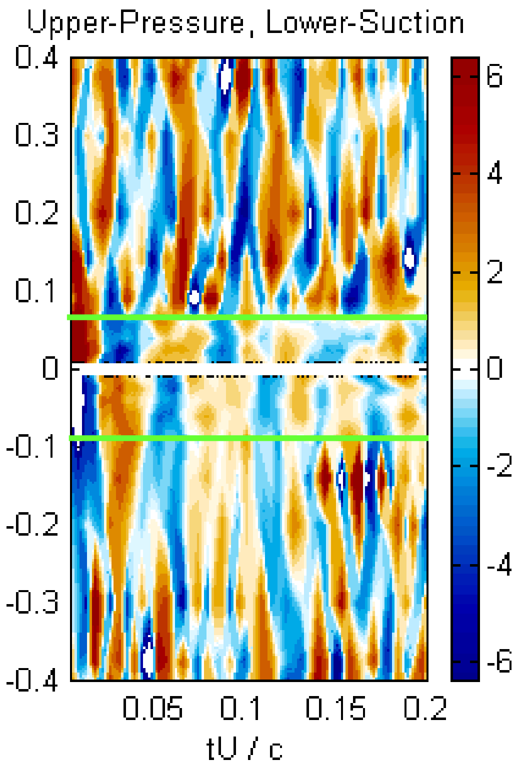

Figure 4.18: Large grid unsteady pressure time series at $\alpha = 0°$

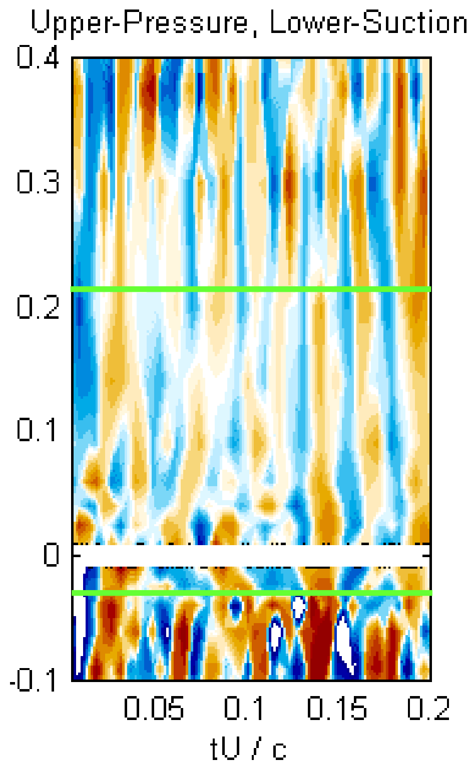

Figure 4.19: Large grid unsteady pressure time series at $\alpha = 4°$

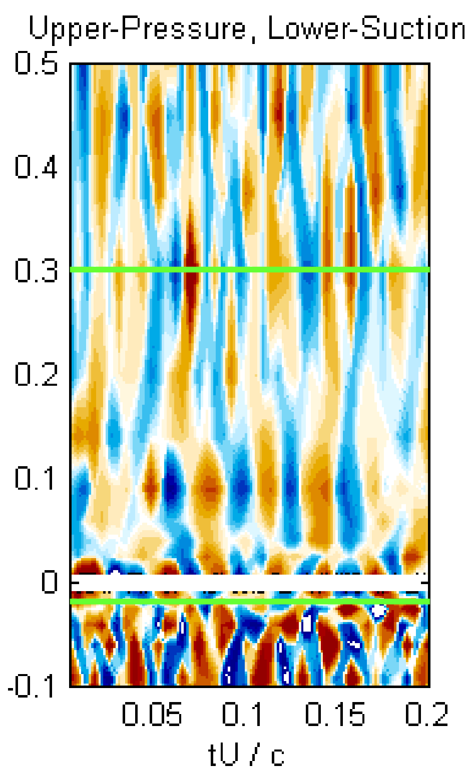

Figure 4.20: Large grid unsteady pressure time series at $\alpha = 8°$

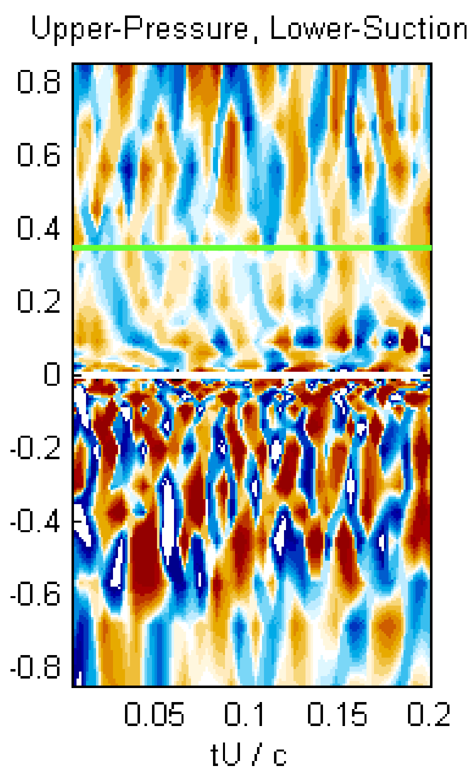

Figure 4.21: Large grid unsteady pressure time series at $\alpha = 12°$

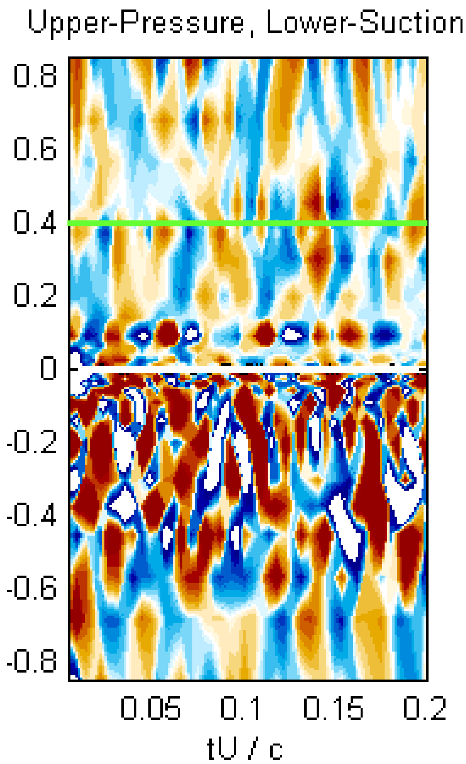

Figure 4.22: Large grid unsteady pressure time series at $\alpha = 16°$

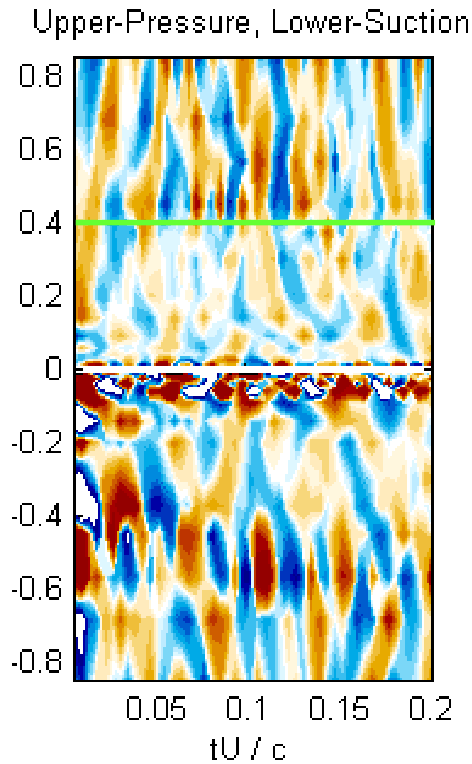

Figure 4.23: Large grid unsteady pressure time series at $\alpha = 20°$

Figure 4.24: Stagnation and separation locations of *small* scale turbulence flow

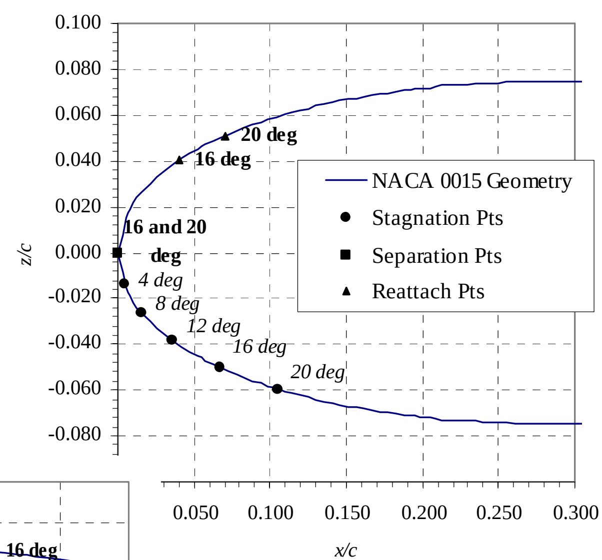

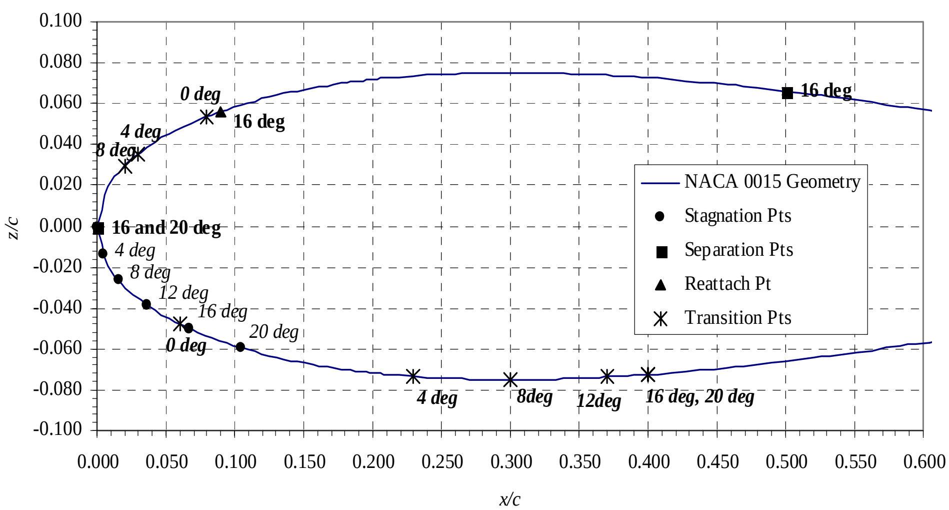

Figure 4.25: Stagnation, transition, and separation locations of *large* scale turbulence flow

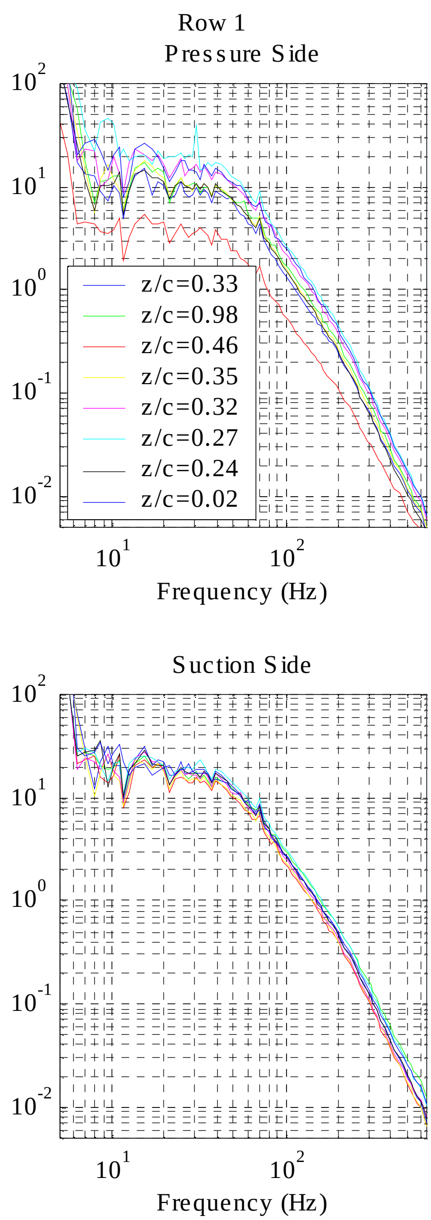

Figure 4.26: 0° AoA spanwise row 1 auto-spectra

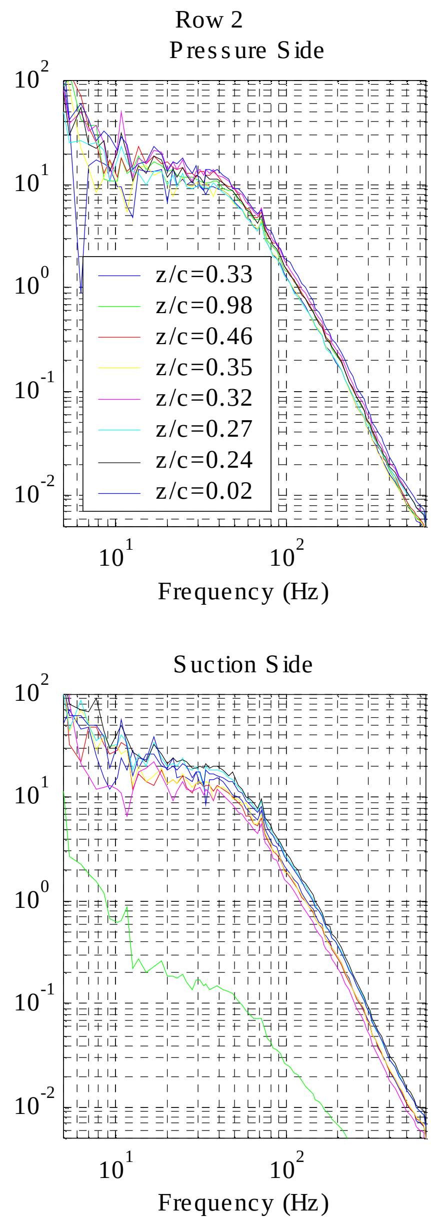

Figure 4.27: 0° AoA spanwise row 2 auto-spectra

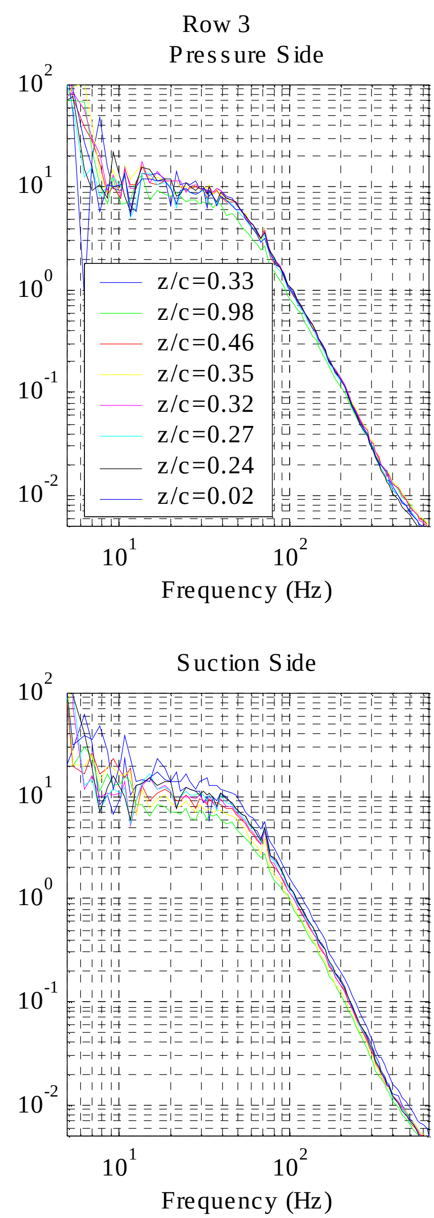

Figure 4.28: 0° AoA spanwise row 3 auto-spectra

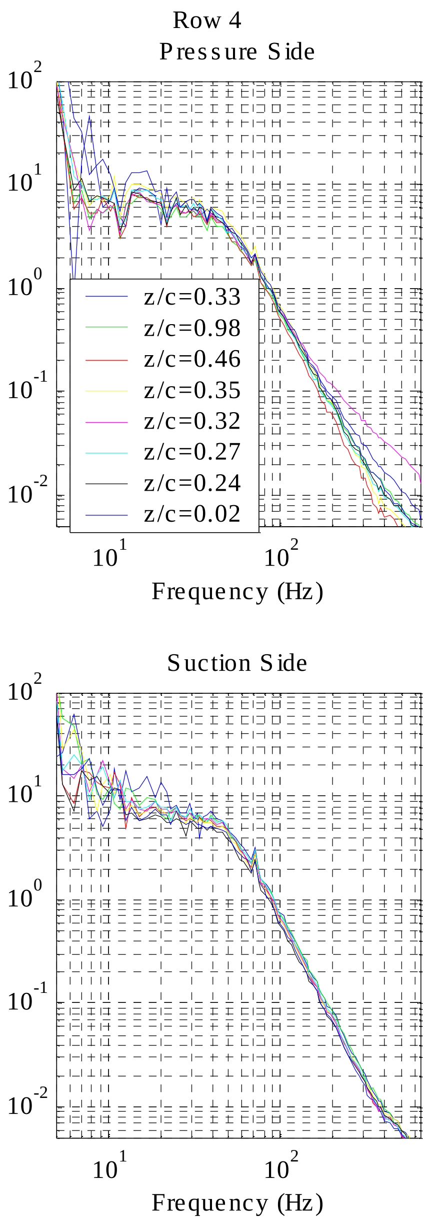

Figure 4.29: 0° AoA spanwise row 4 auto-spectra

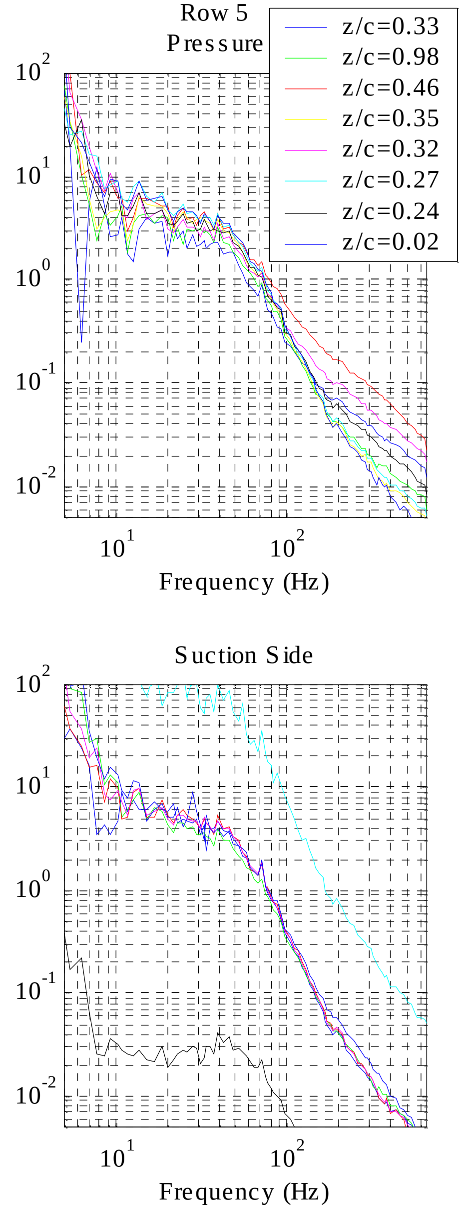

Figure 4.30: 0° AoA spanwise row 5 auto-spectra

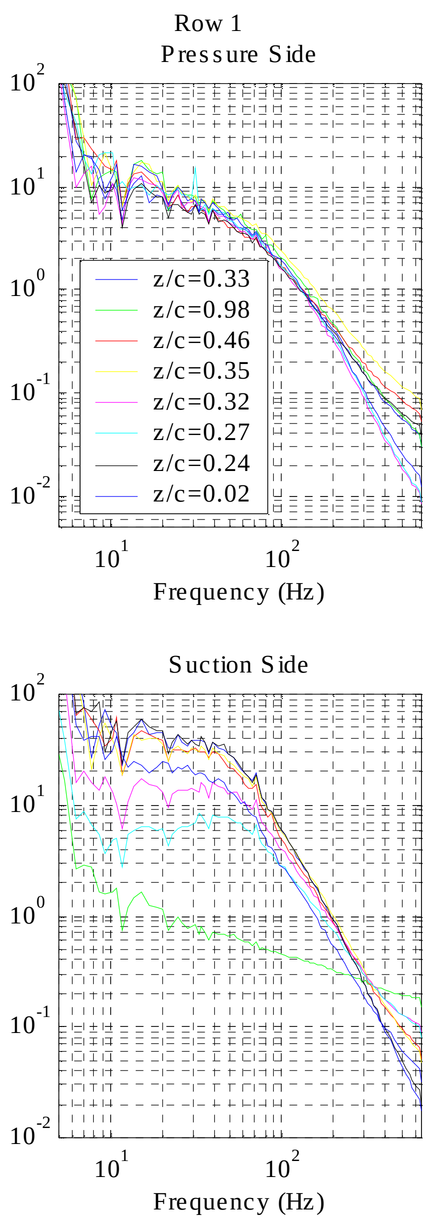

Figure 4.31: 8° AoA spanwise row 1 auto-spectrum

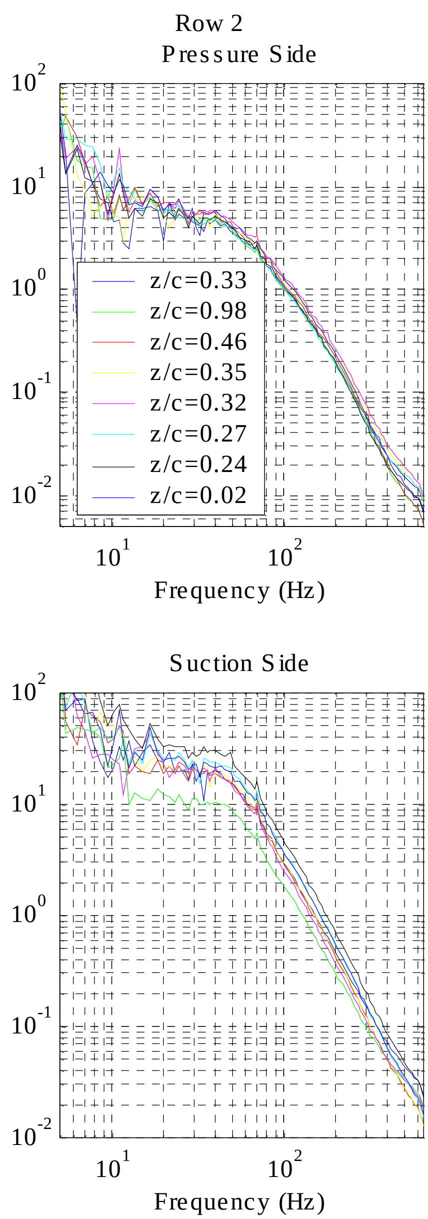

Figure 4.32: 8° AoA spanwise row 2 auto-spectrum

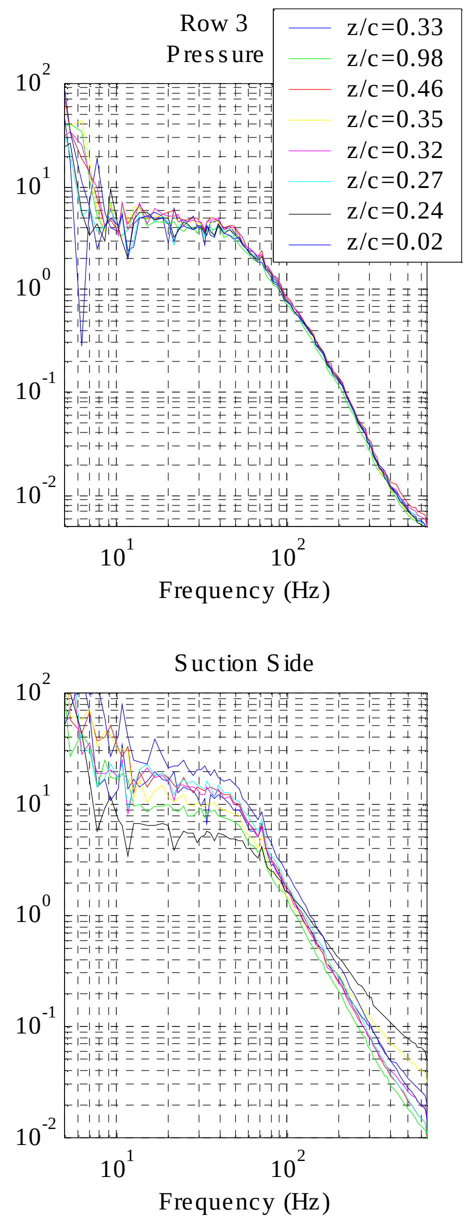

Figure 4.33: 8° AoA spanwise row 3 auto-spectrum

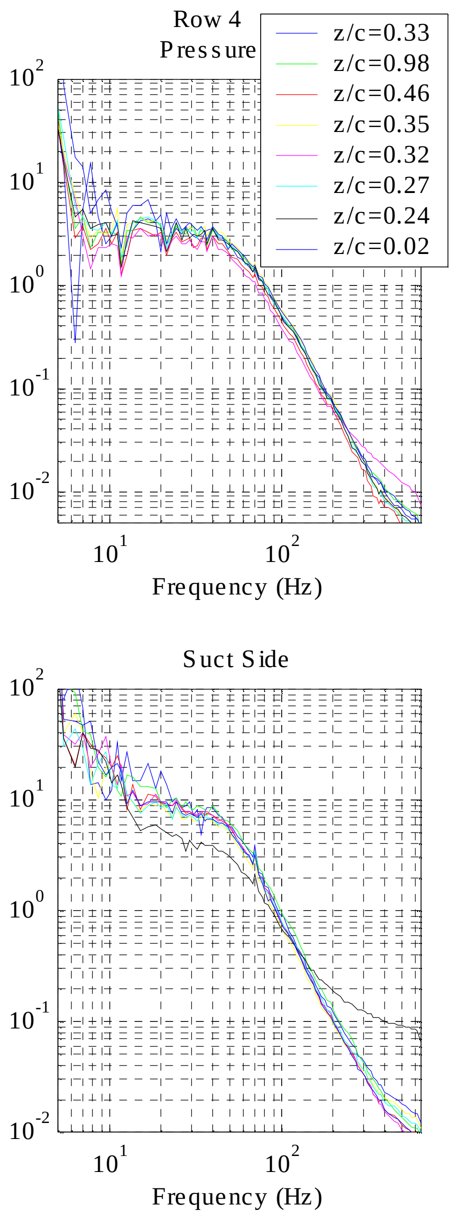

Figure 4.34: 8° AoA spanwise row 4 auto-spectrum

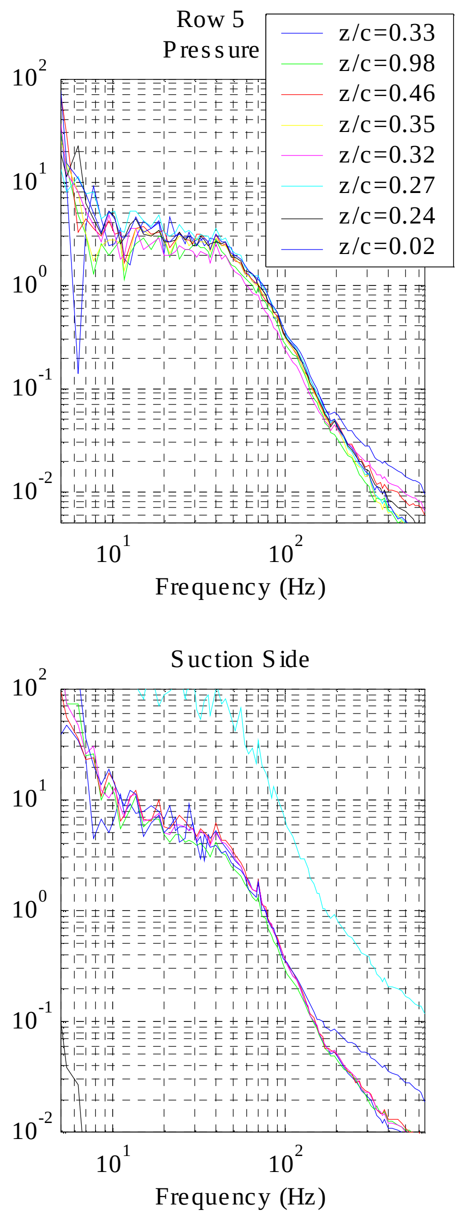

Figure 4.35: 8° AoA spanwise row 5 auto-spectrum

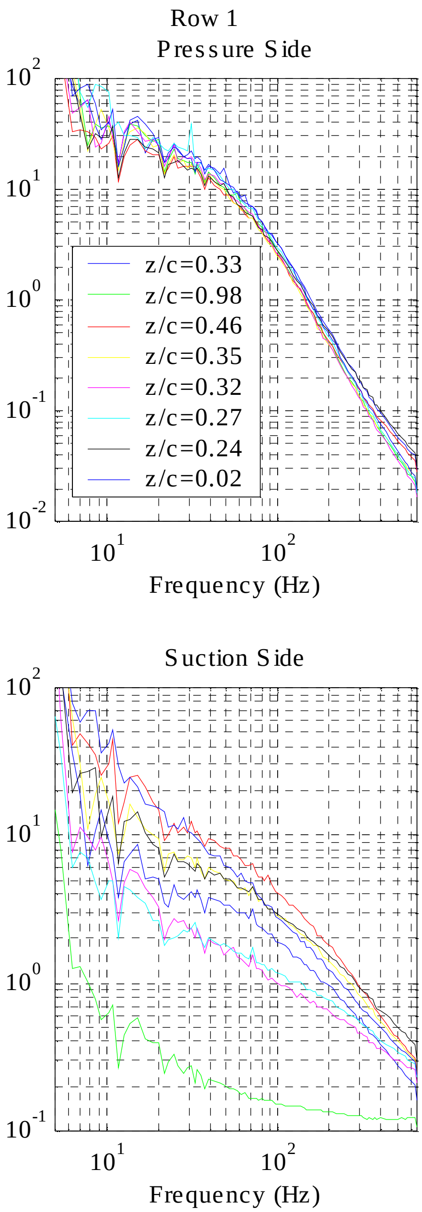

Figure 4.36: 20° AoA spanwise row 1 auto-spectrum

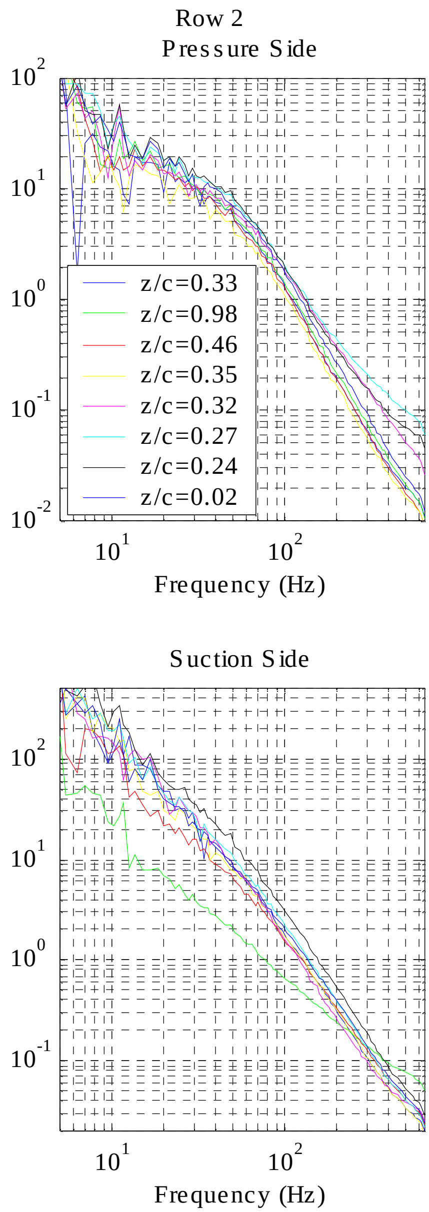

Figure 4.37: 20° AoA spanwise row 2 auto-spectrum

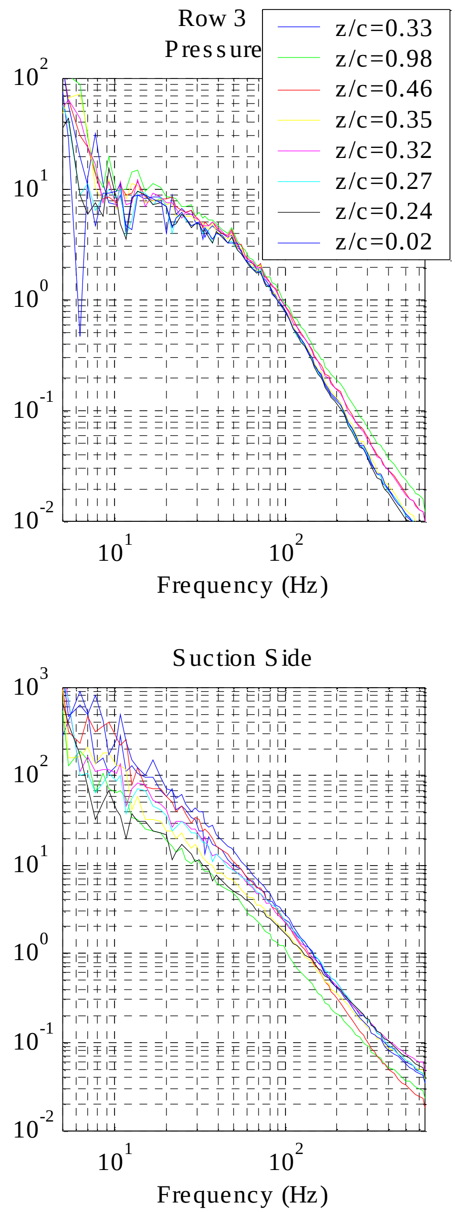

Figure 4.38: 20° AoA spanwise row 3 auto-spectrum

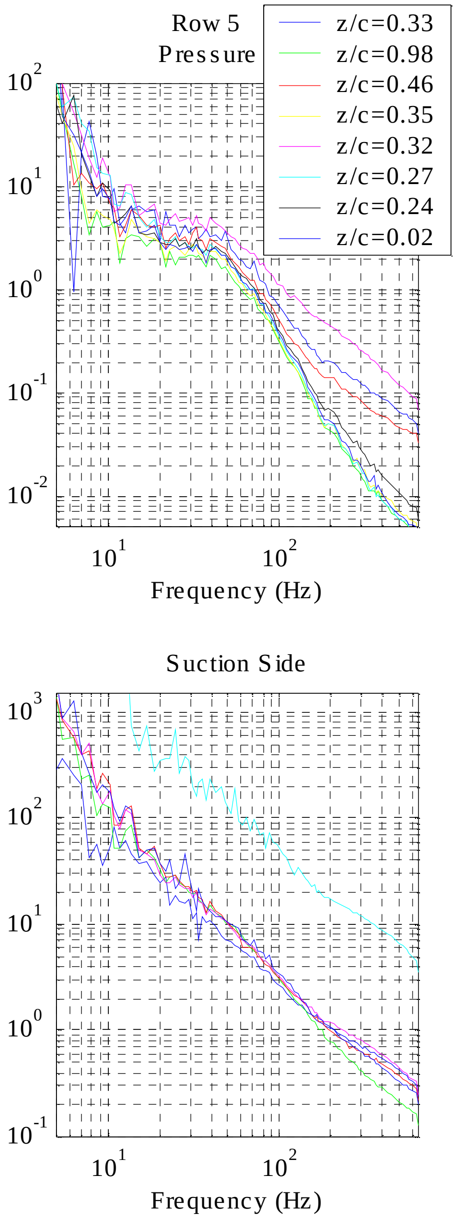

Figure 4.39: 20° AoA spanwise row 4 auto-spectrum

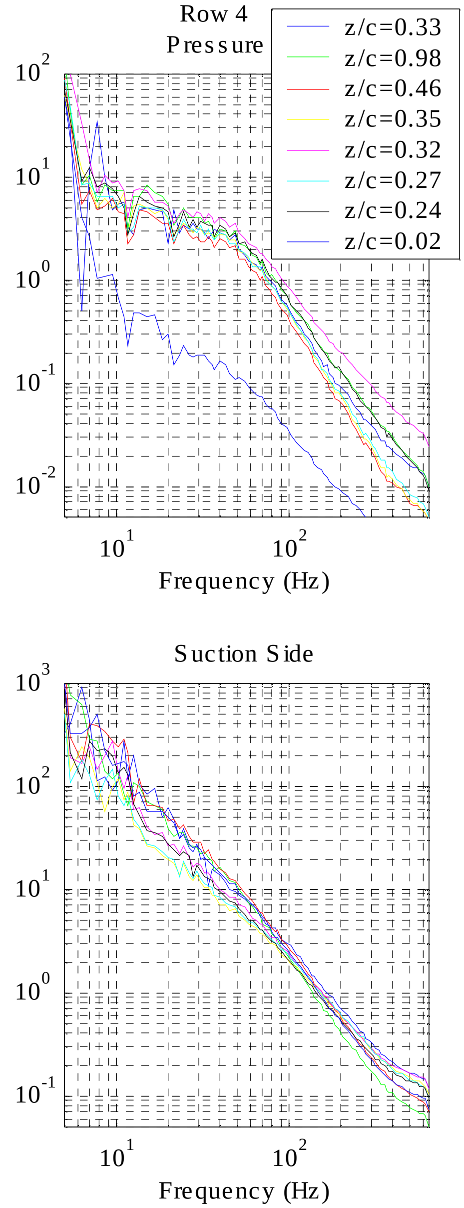

Figure 4.40: 20° AoA spanwise row 5 auto-spectrum

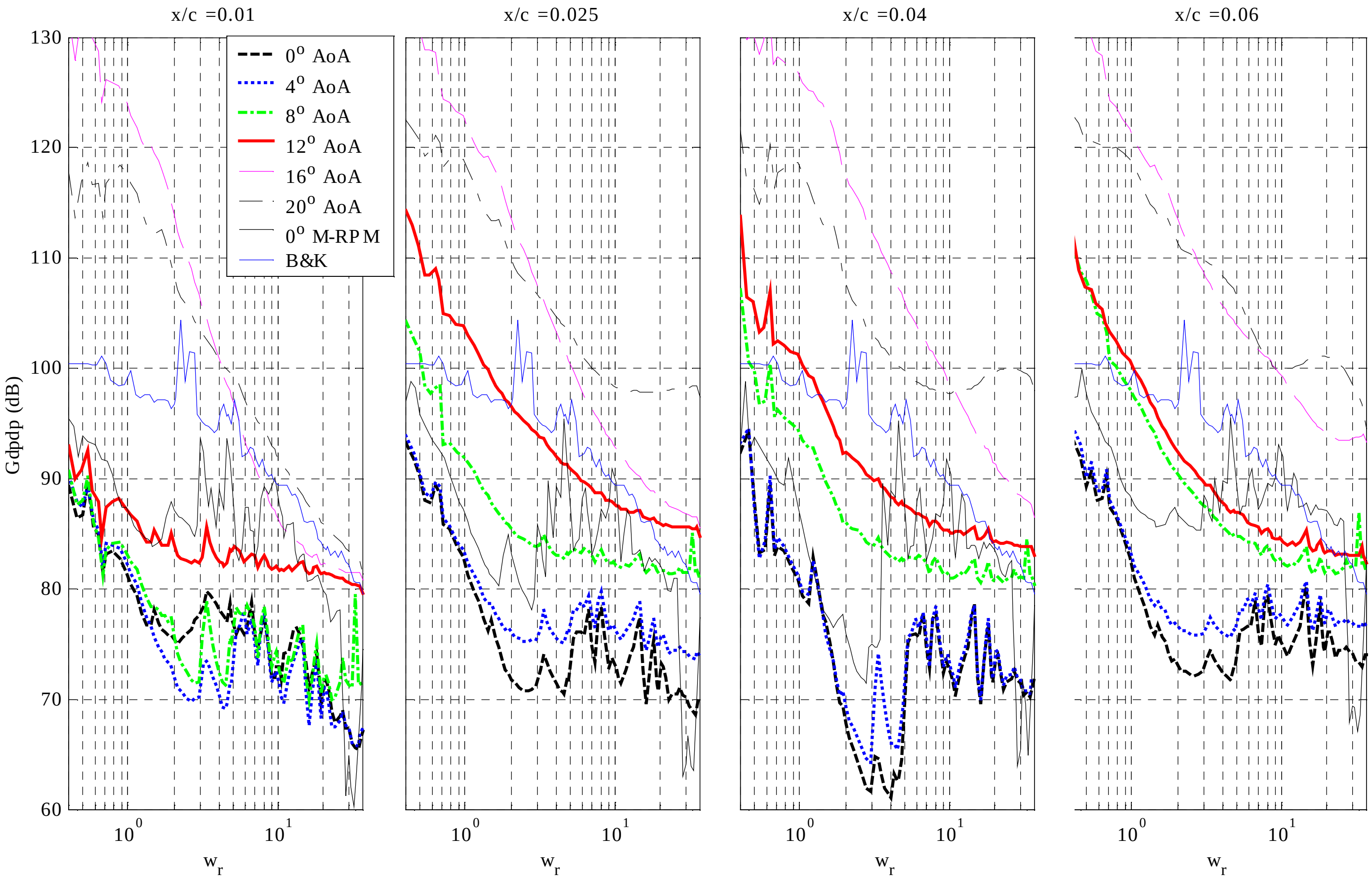

Figure 4.41: Pressure difference matched flow speed data plotted at all angles of attack with matched RPM data at α = 0° and reference (B&K) microphone data at *x/c* = 0.01, 0.025, 0.04, 0.06

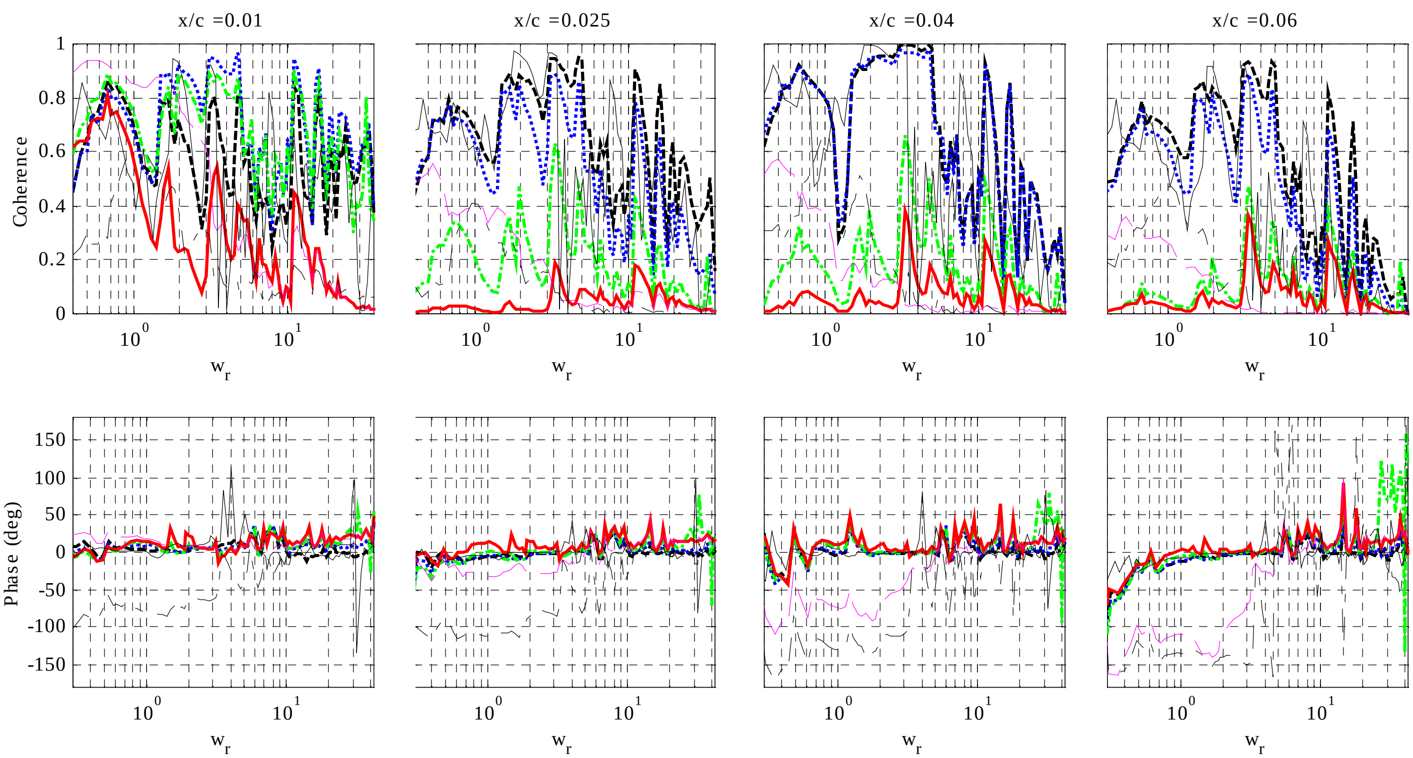

Figure 4.42: Coherence and phase of matched flow speed data plotted at all angles of attack with matched RPM data at α = 0° and reference (B&K) microphone data at *x/c* = 0.01, 0.025, 0.04, 0.06

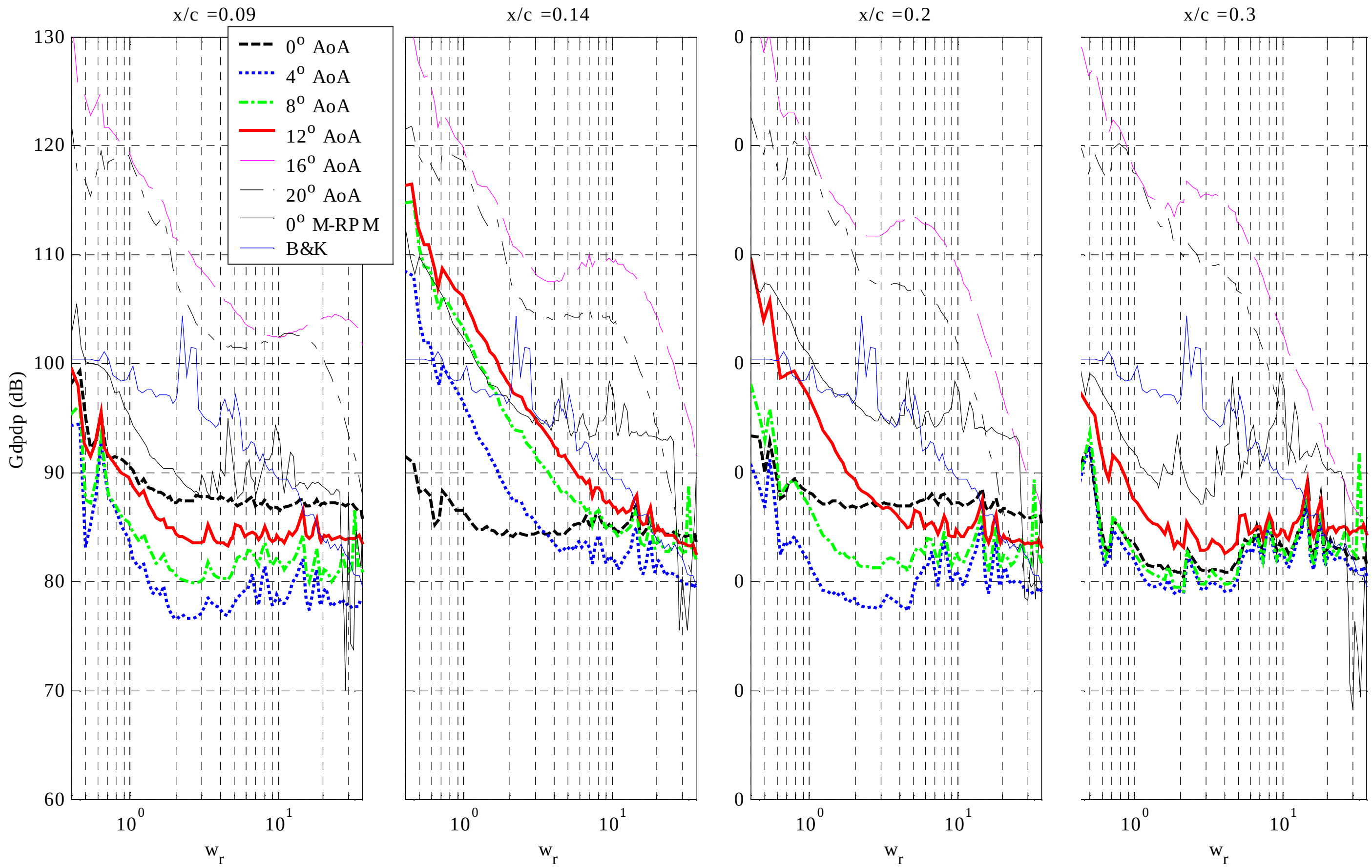

Figure 4.43: Pressure difference matched flow speed data plotted at all angles of attack with matched RPM data at $\alpha = 0°$ and reference (B&K) microphone data at *x/c* = 0.09, 0.14, 0.2, 0.3

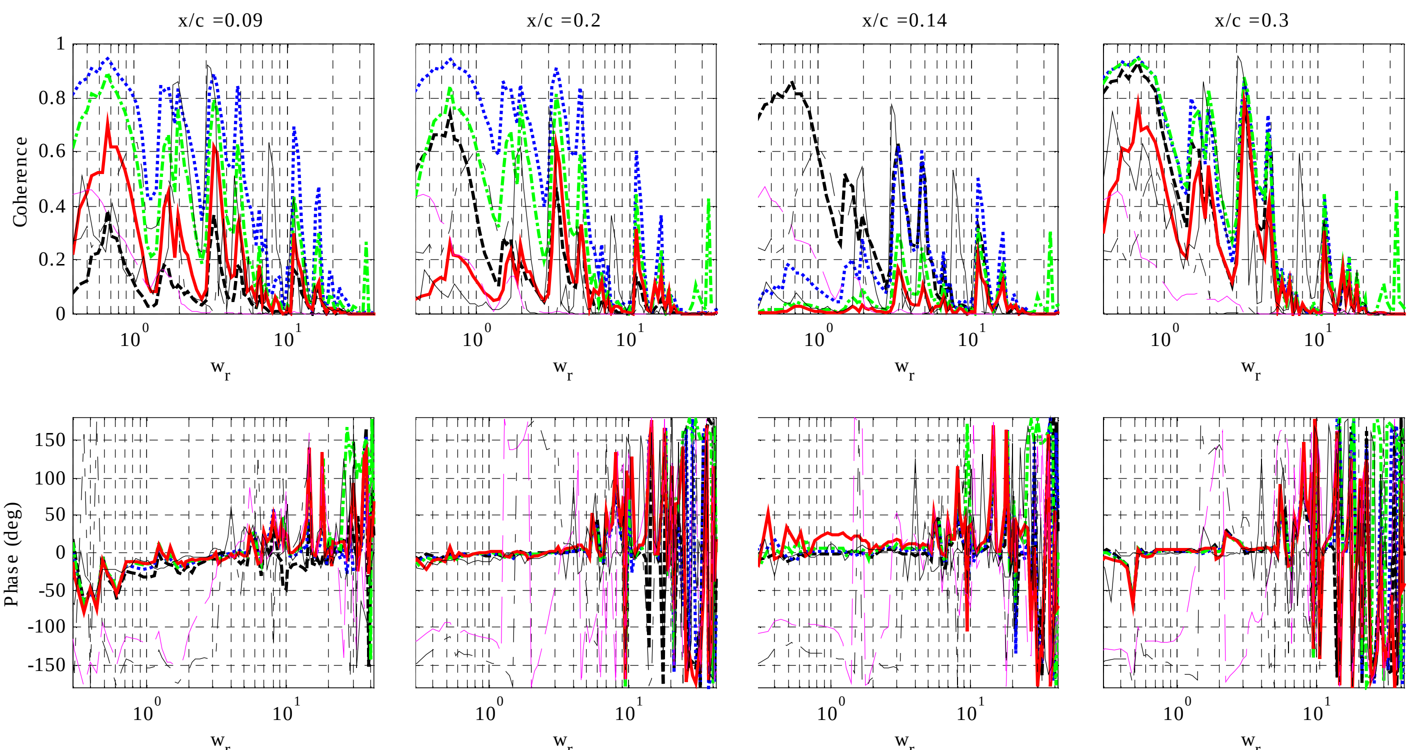

Figure 4.44: Coherence and phase of matched flow speed data plotted at all angles of attack with matched RPM data at $\alpha = 0°$ and reference (B&K) microphone data at *x/c* = 0.09, 0.14, 0.2, 0.3

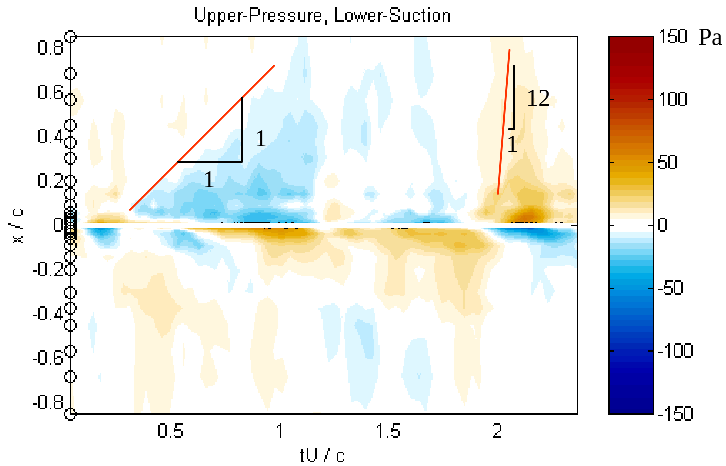

Figure 4.45: Instantaneous pressure at 0° AoA, *large* grid

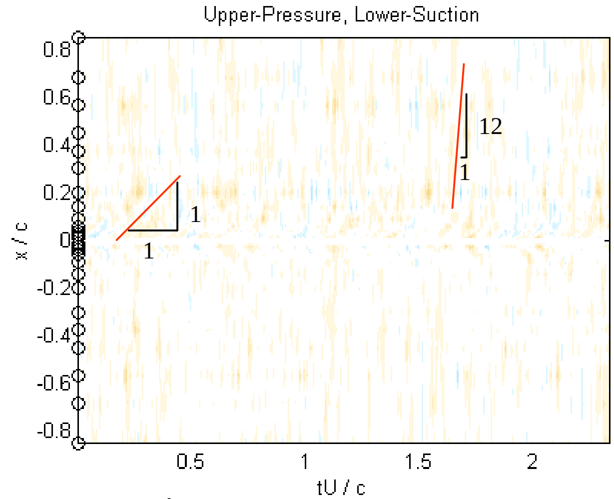

Figure 4.46: Instantaneous pressure at 0° AoA, *small* grid

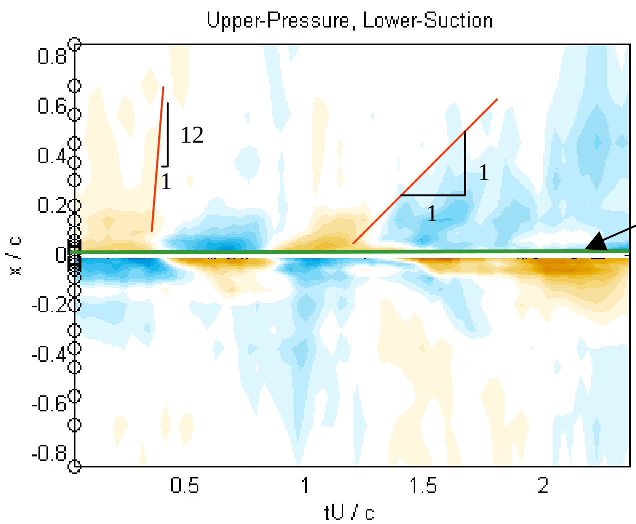

Figure 4.47: Instantaneous pressure at 4° AoA, *large* grid

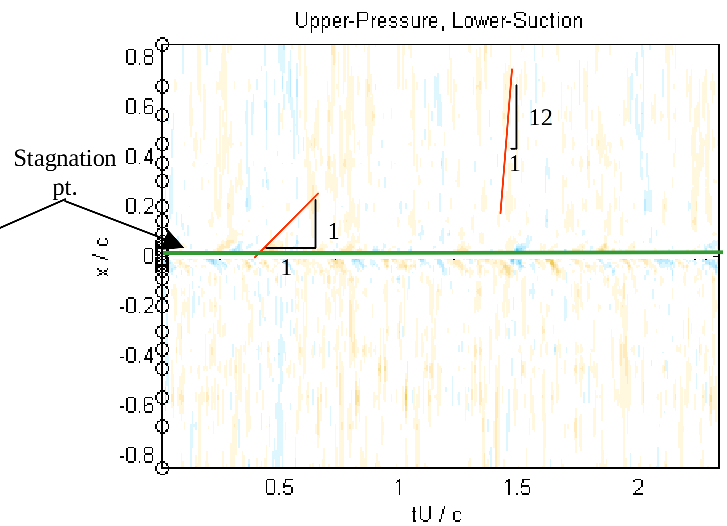

Figure 4.48: Instantaneous pressure at 4° AoA, *small* grid

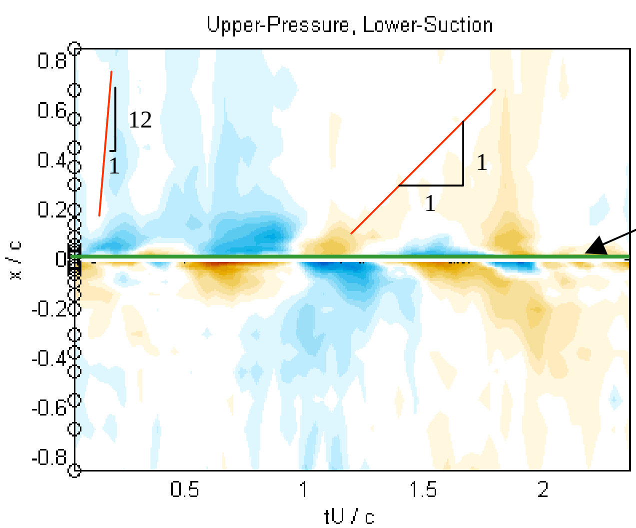

Figure 4.49: Instantaneous pressure at 8° AoA, *large* grid

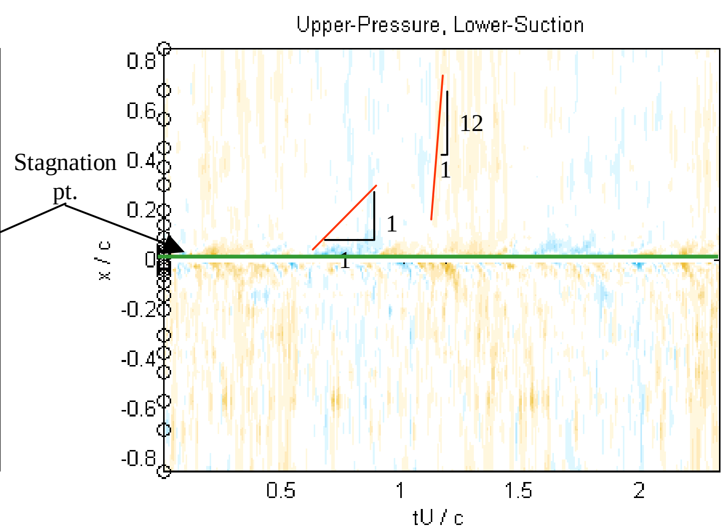

Figure 4.50: Instantaneous pressure at 8° AoA, *small* grid

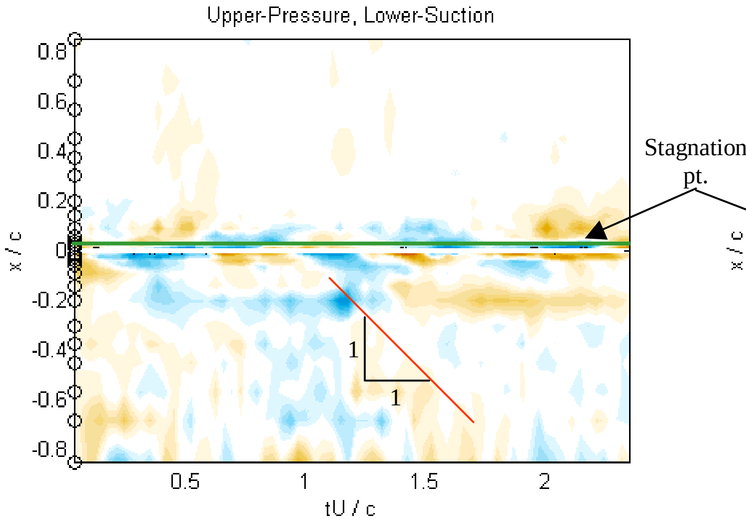

Figure 4.51: Instantaneous pressure at 12° AoA, *large* grid

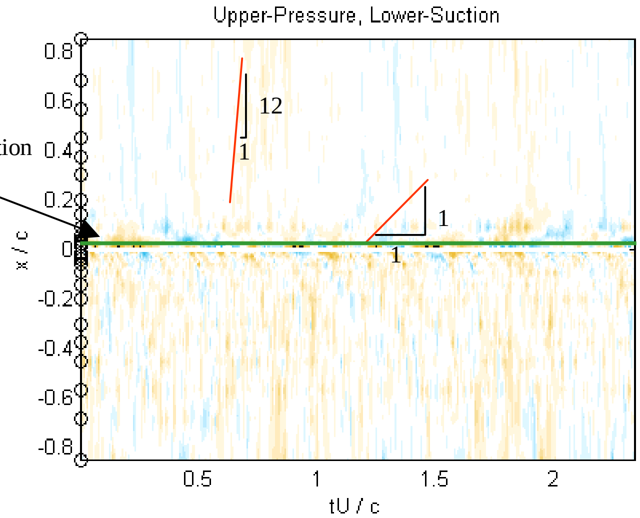

Figure 4.52: Instantaneous pressure at 12° AoA, *small* grid

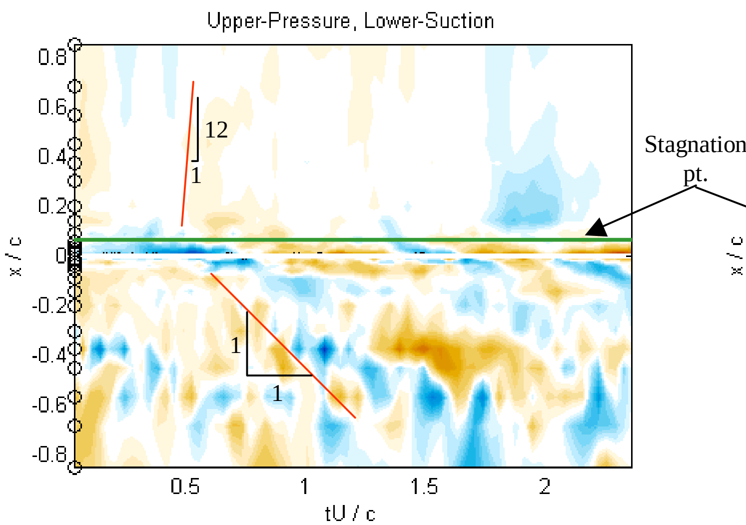

Figure 4.53: Instantaneous pressure at 16° AoA, *large* grid

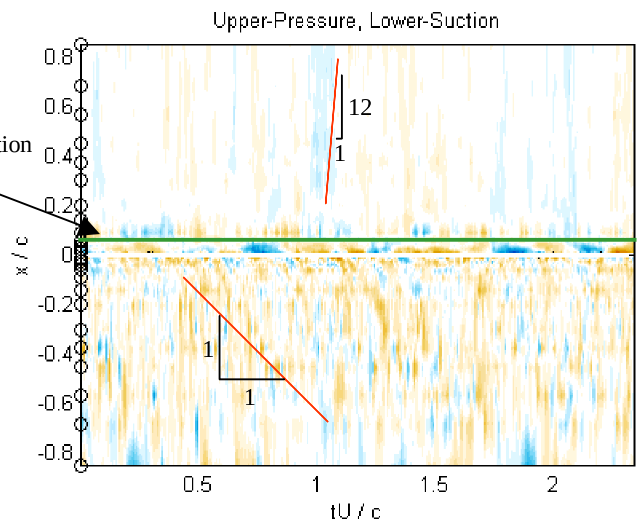

Figure 4.54: Instantaneous pressure at 16° AoA, *small* grid

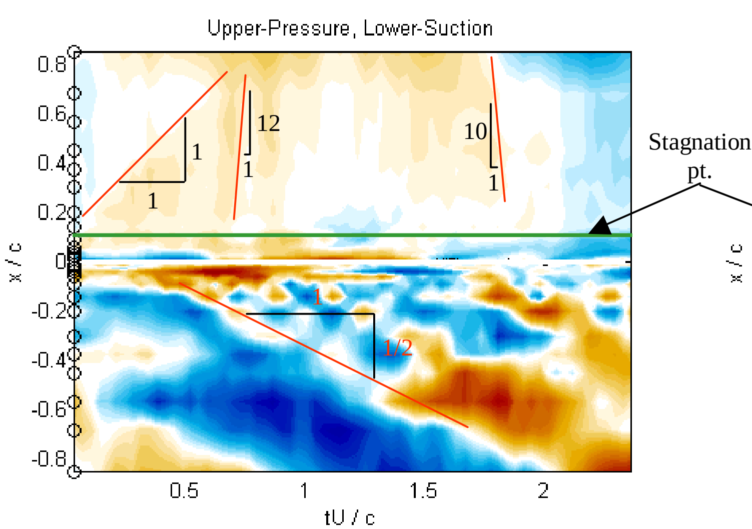

Figure 4.55: Instantaneous pressure at 20° AoA, *large* grid

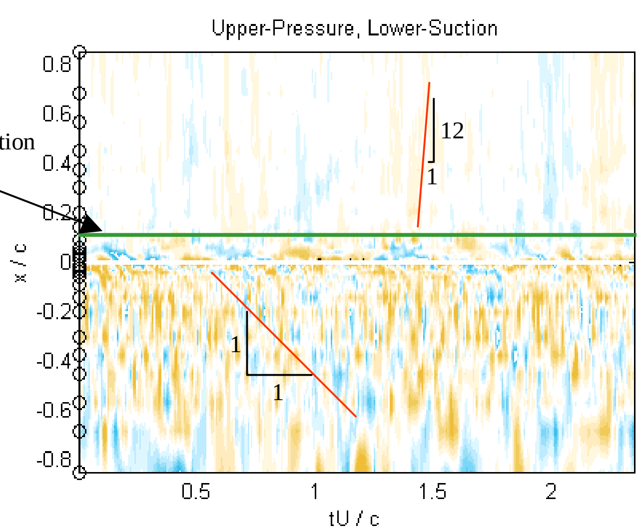

Figure 4.56: Instantaneous pressure at 20° AoA, *small* grid

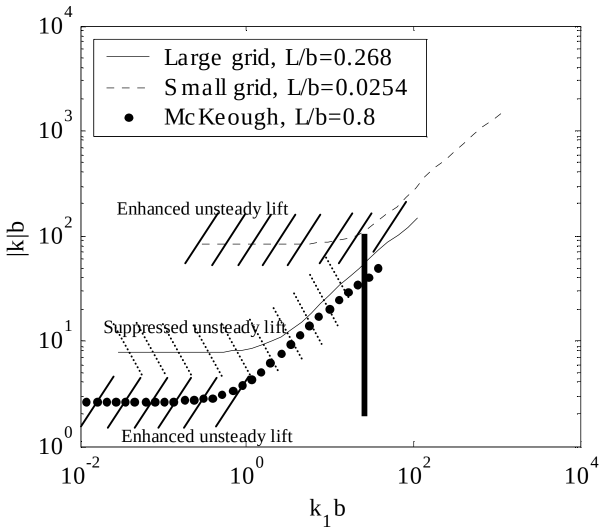

Figure 4.57: Relationship between the average wavenumber magnitude |k| and the streamwise wavenumber k_1 for the small and large grid turbulence, assuming von Karman spectral forms.

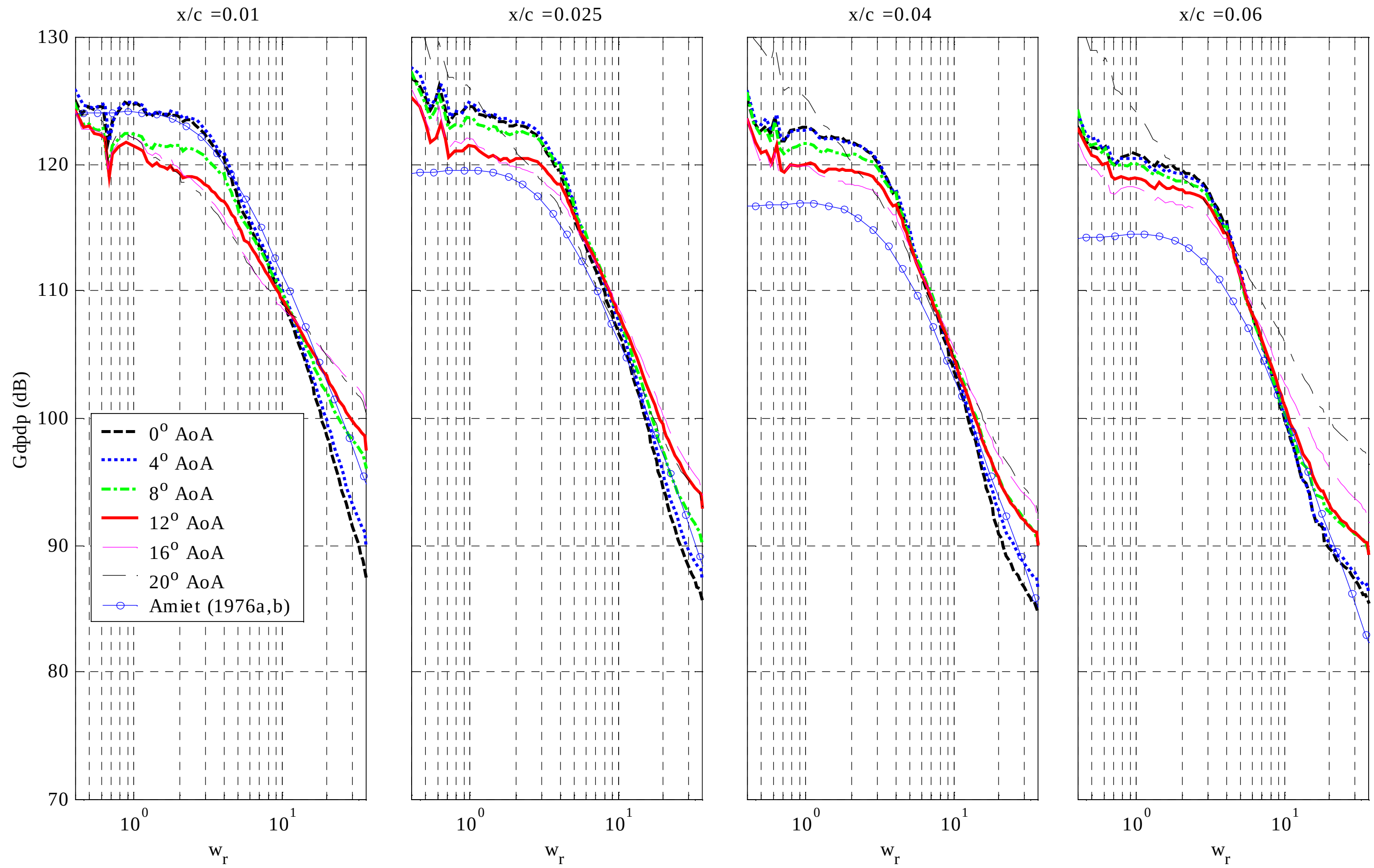

Figure 4.58: Pressure differenced auto-spectrum for L/r_c = 5.41 at x/c = 0.01, 0.025, 0.04, 0.06

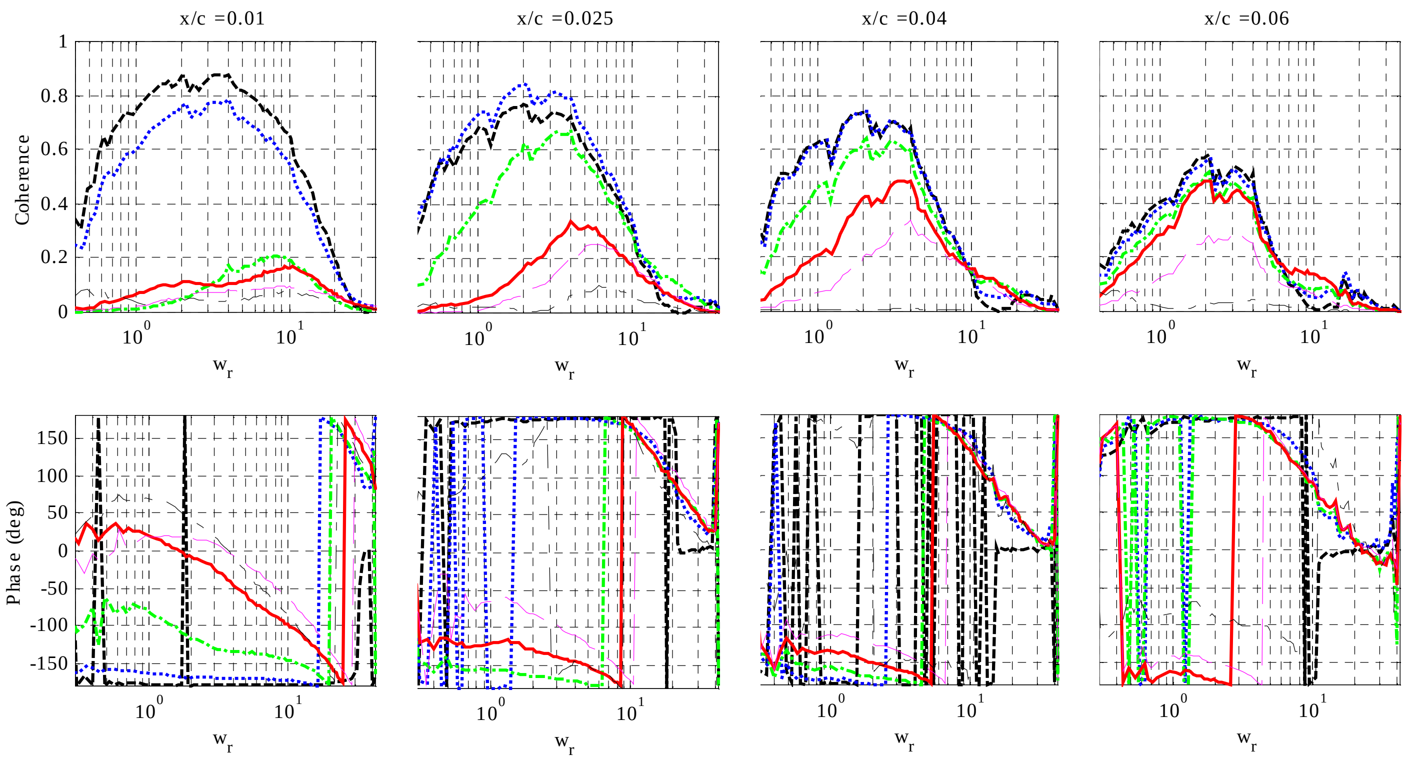

Figure 4.59: Pressure differenced coherence and phase for L/r_c = 5.41 at x/c = 0.01, 0.025, 0.04, 0.06

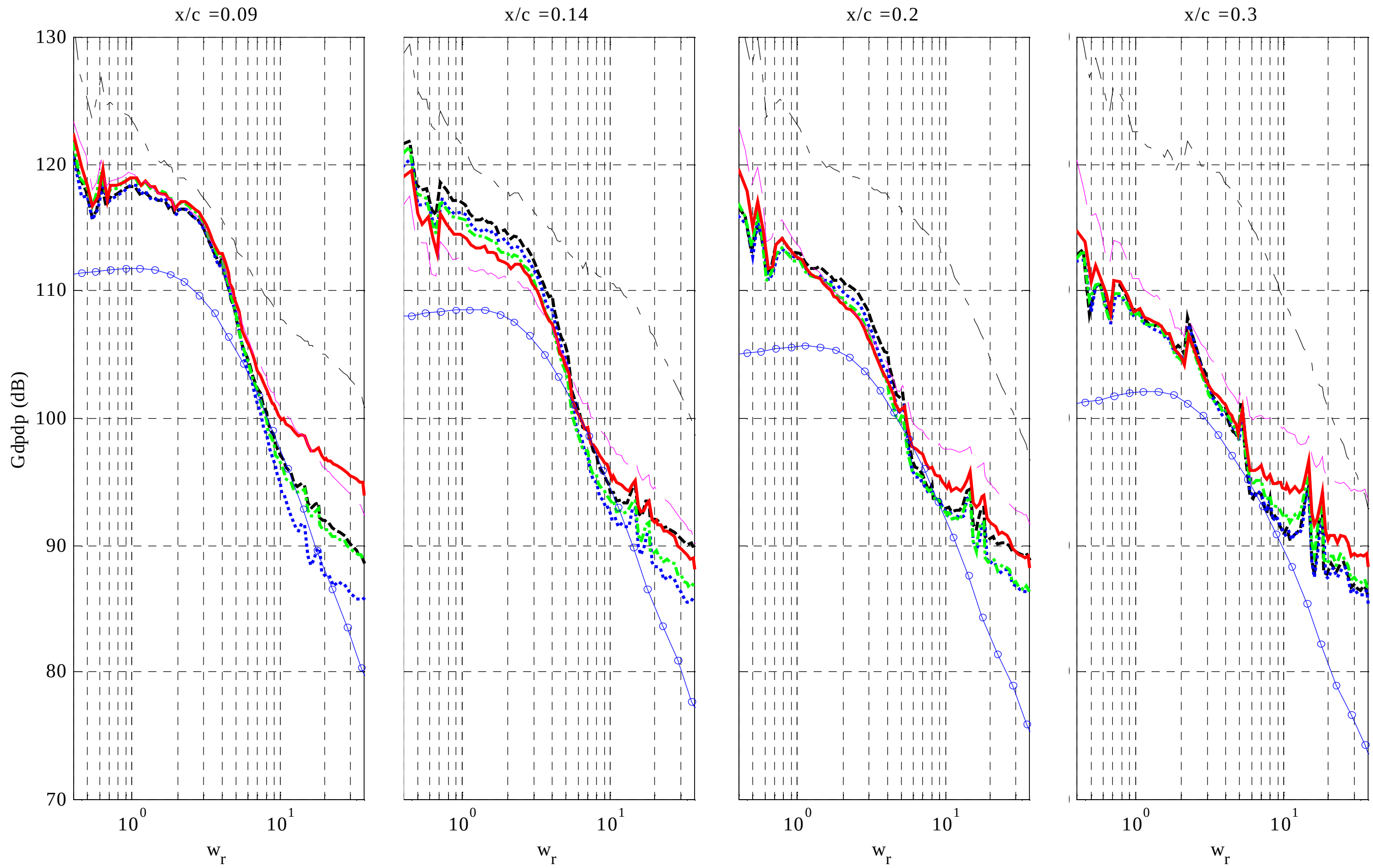

Figure 4.60: Pressure differenced auto-spectrum for L/r_c = 5.41 at x/c = 0.09, 0.14, 0.2, 0.3

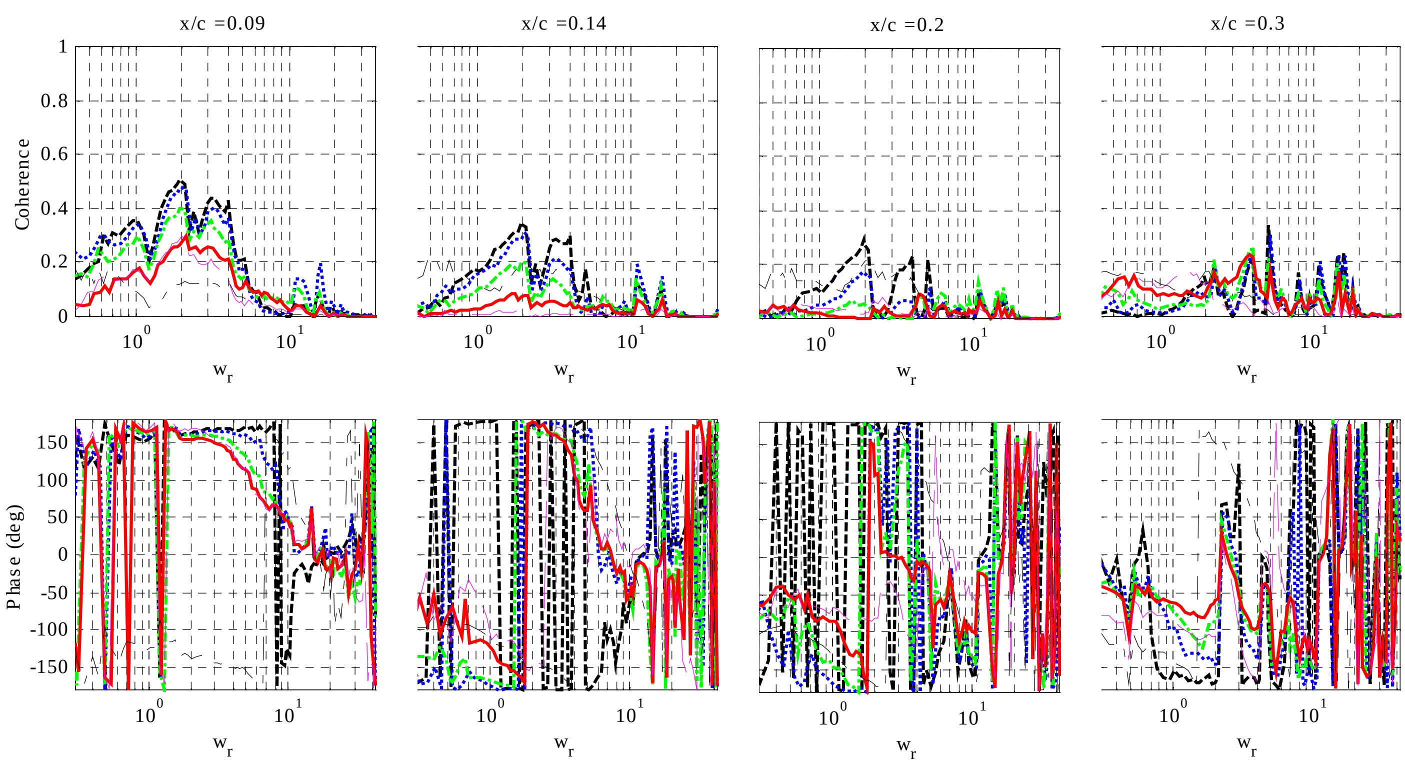

Figure 4.61: Pressure differenced coherence and phase for L/r_c = 5.41 at x/c = 0.09, 0.14, 0.2, 0.3

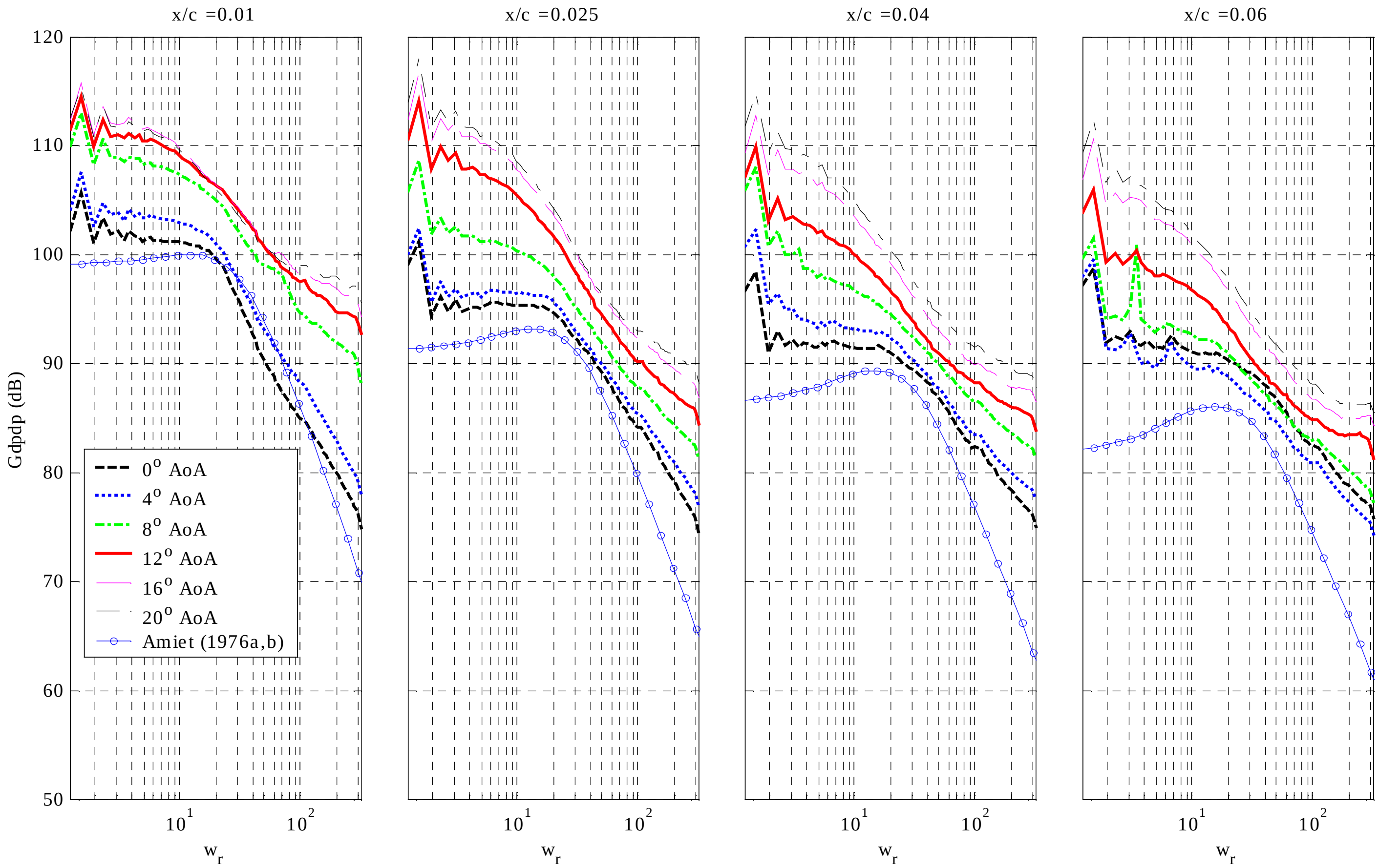

Figure 4.62: Pressure differenced auto-spectrum for L/r_c = 0.519 at x/c = 0.01, 0.025, 0.04, 0.06

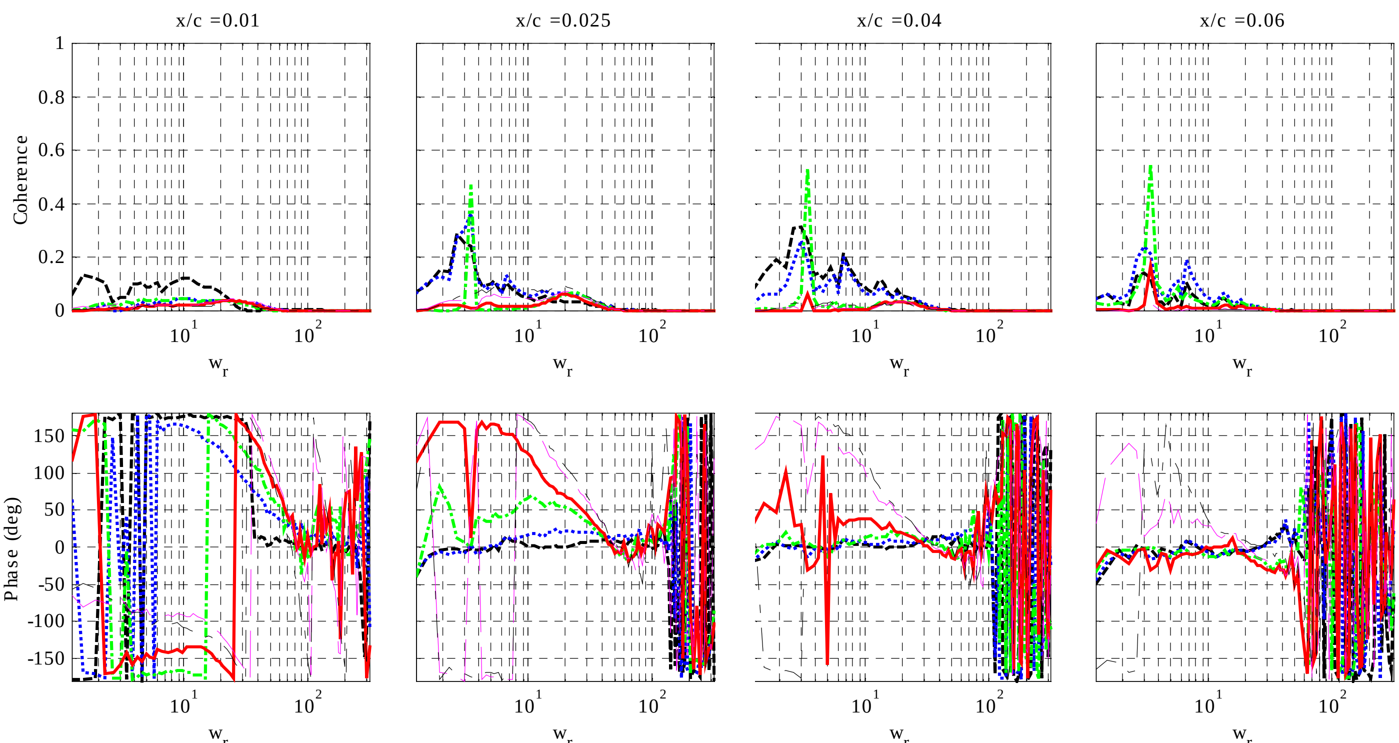

Figure 4.63: Pressure differenced coherence and phase for L/r_c = 0.519 at x/c = 0.01, 0.025, 0.04, 0.06

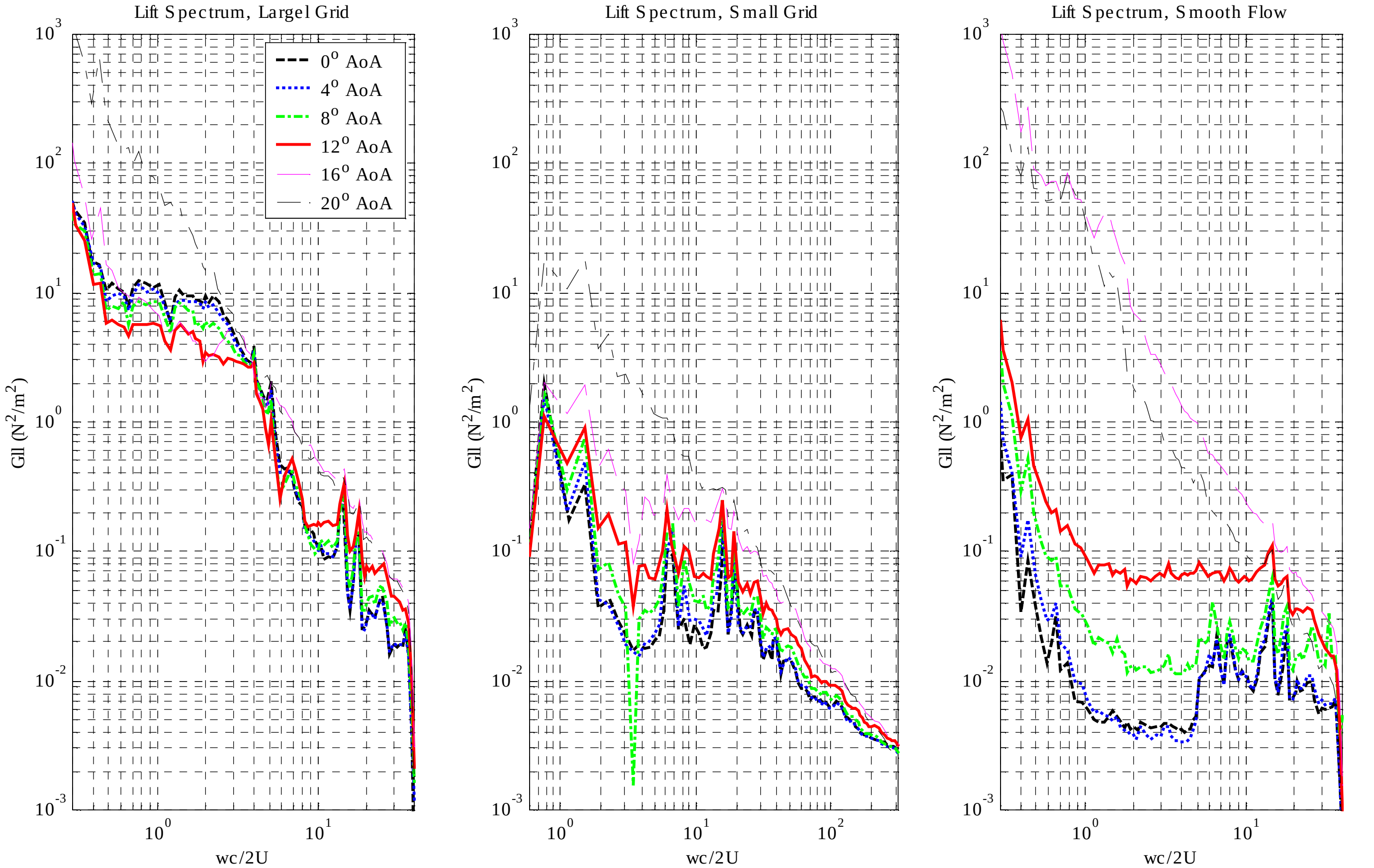

Figure 4.64: Lift spectrum formed over entire chord for L/r_c =5.41, L/r_c = 0.519, and smooth flow

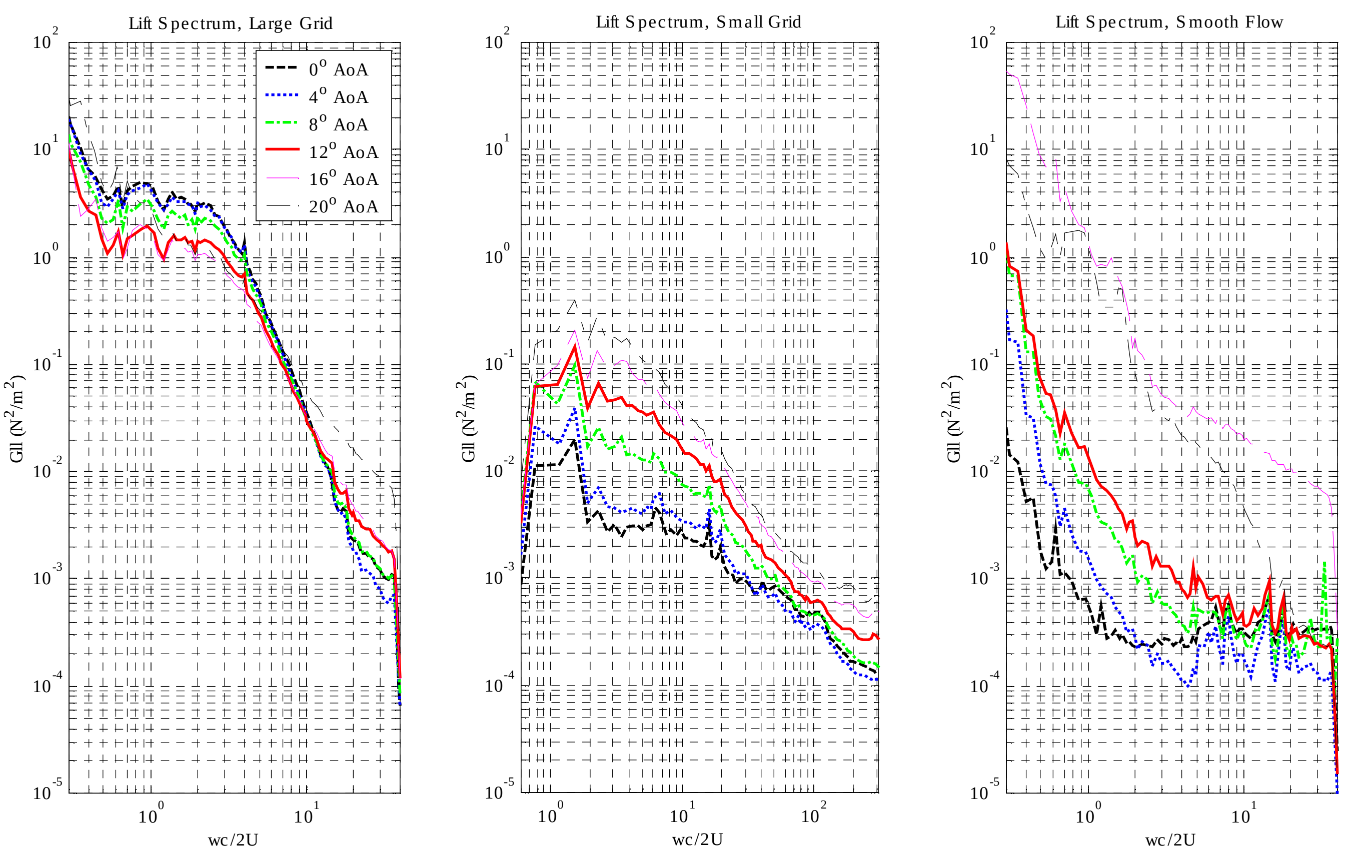

Figure 4.65: Lift spectrum formed over 0 to 14% chord for L/r_c =5.41, L/r_c = 0.519, and smooth flow

Figure 4.66: $|G_{\Delta P\Delta P'}|/G_{P1P1}$ for L/r_c = 5.41 at ω_r = 1.123, 2.9285, 5.8357, and 11.6481

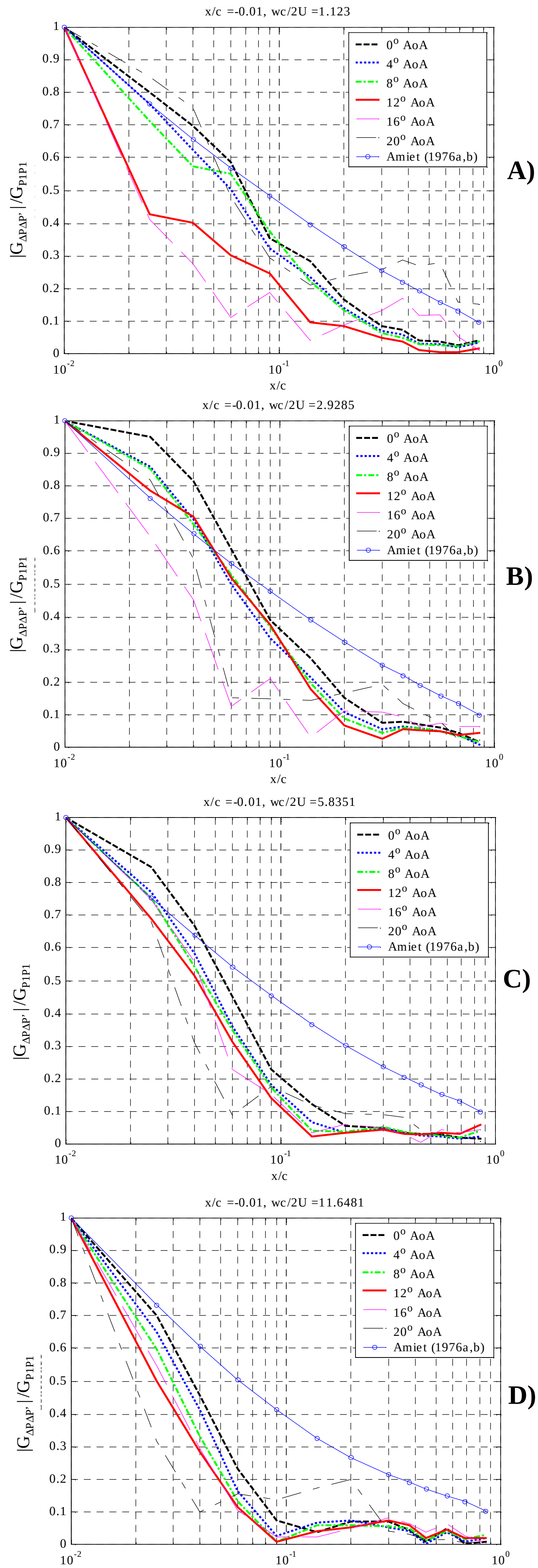

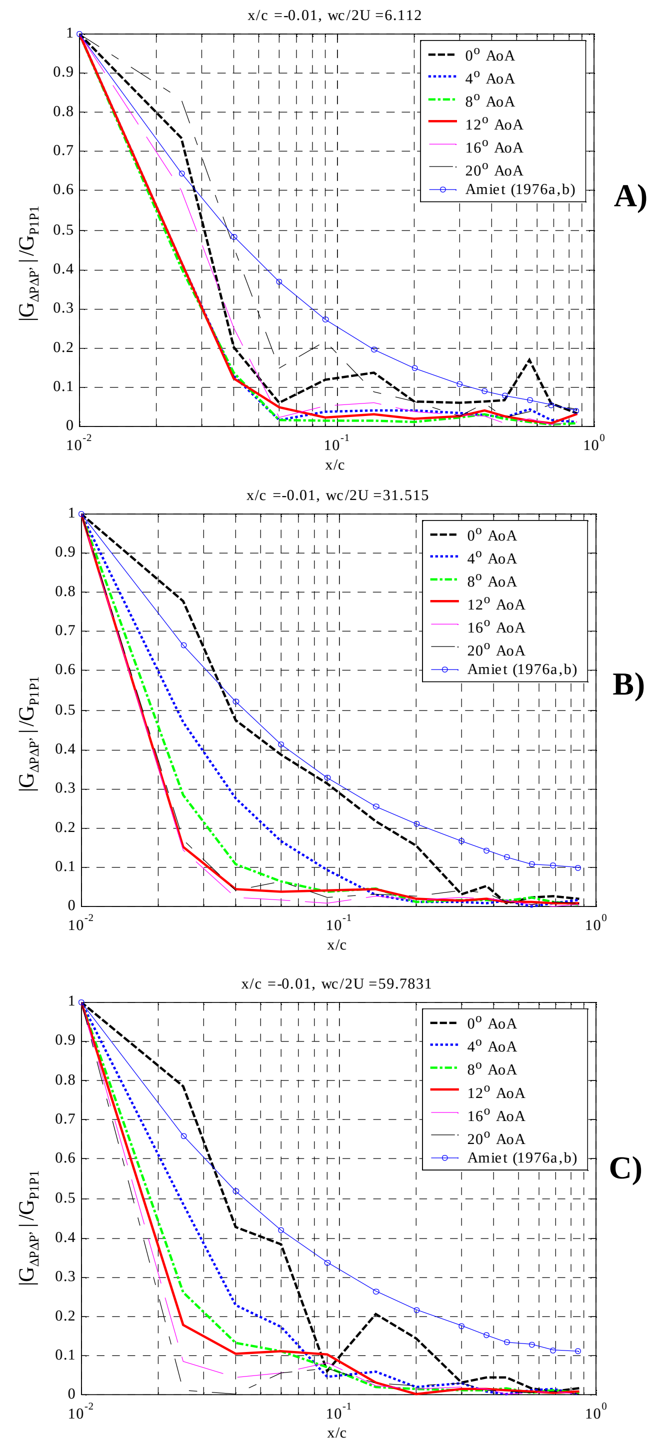

Figure 4.67: $|G_{\Delta P\Delta P'}|/G_{P1P1}$ for L/r_c = 0.519 at ω_r= 6112, 31.515, and 59.7831

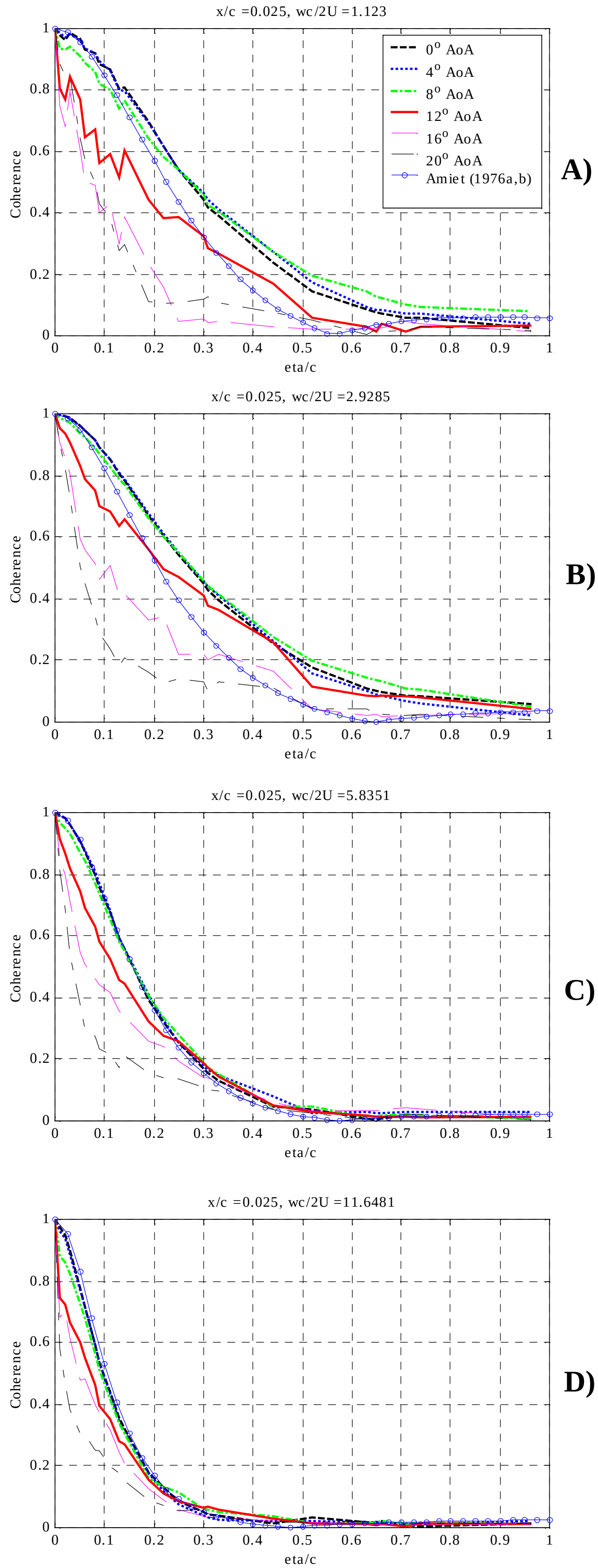

Figure 4.68: Coherence for L/r_c = 5.41 at x/c = 0.025 at ω_r = 1.123, 2.9285, 5.8357, and 11.6481

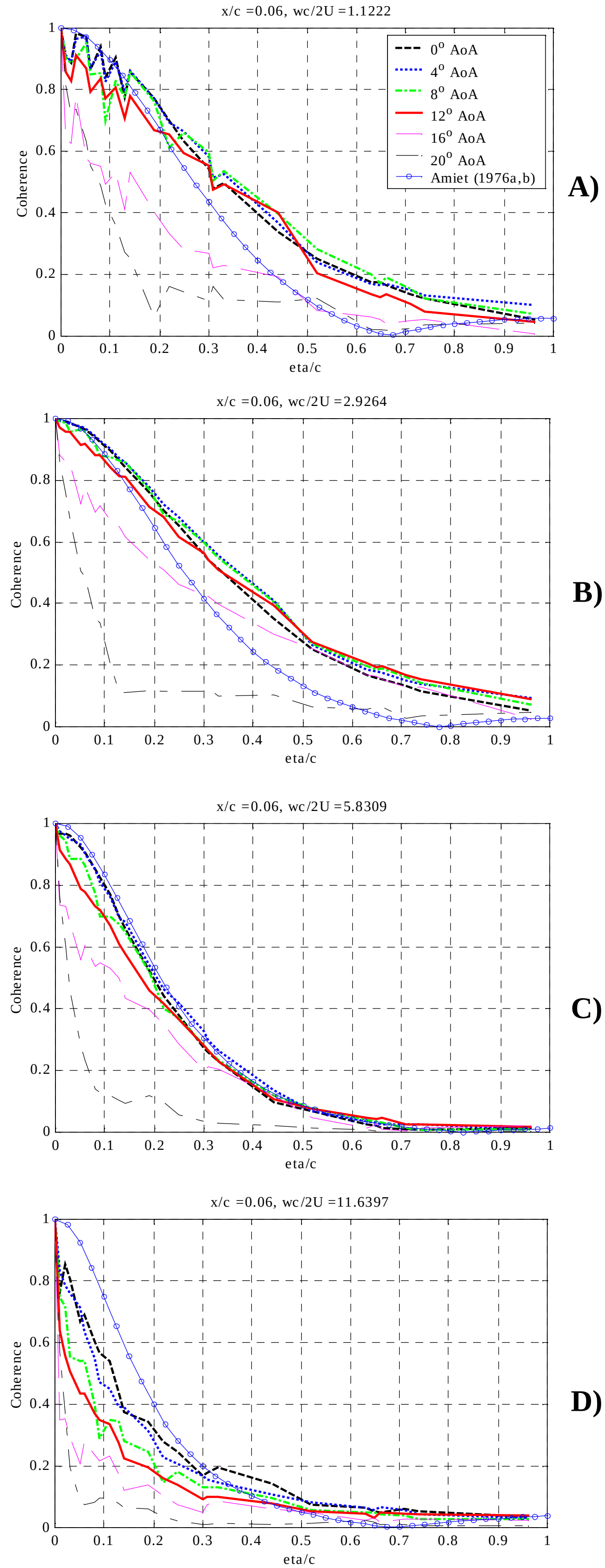

Figure 4.69: Coherence for L/r_c = 5.41 at x/c = 0.06 at ω_r = 1.123, 2.9285, 5.8357, and 11.6481

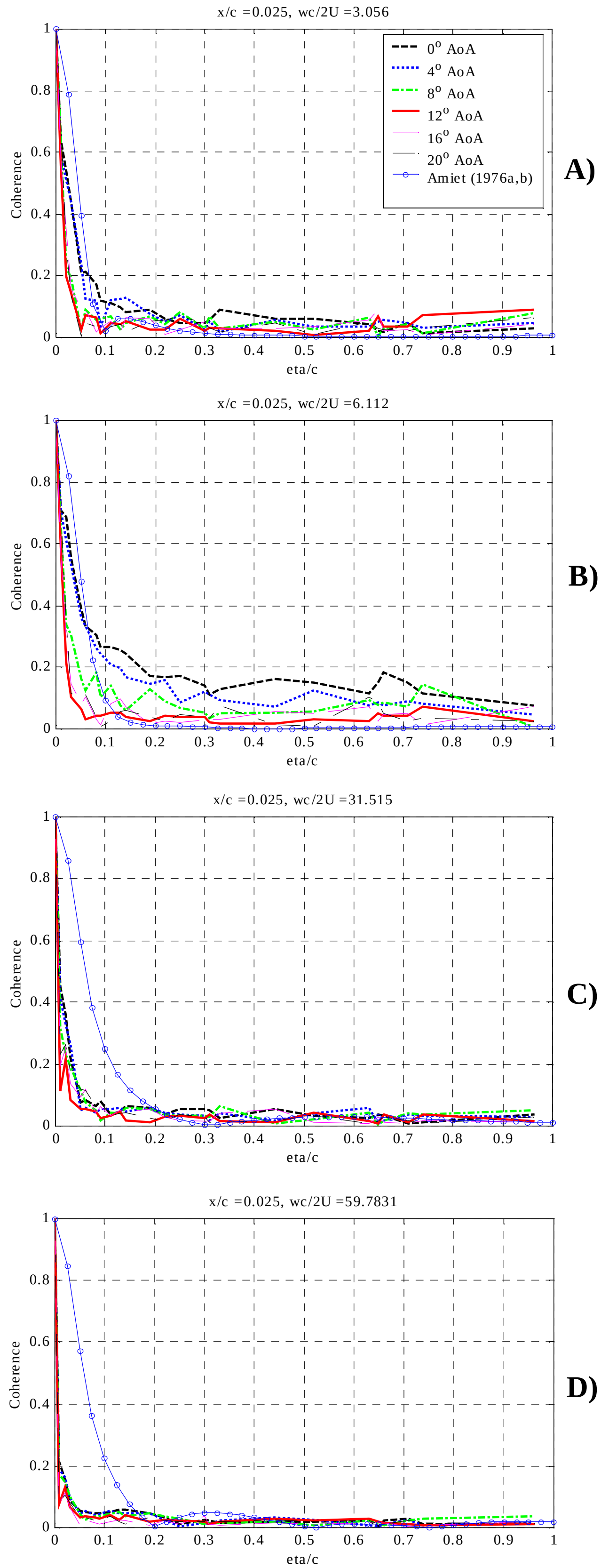

Figure 4.70: Coherence for L/r_c = 0.519 at x/c = 0.025 at ω_r= 3.056, 6.112, 31.515, and 59.7831

Vita: Patrick Francis Mish

EDUCATION:

M.S. Aerospace Engineering, June 2001
Research (experimental): Unsteady surface pressure response from turbulent flow interacting with a lifting airfoil
Virginia Tech, Blacksburg VA
GPA: 3.61/4.0

B.S., Ocean and Aerospace Engineering, May 1999
Virginia Tech, Blacksburg VA
GPA (in major): 3.6/4.0

EXPERIENCE:

GRADUATE TEACHING ASSISTANT
Virginia Tech Aerospace and Ocean Engineering Department, Blacksburg VA, *08/99-Present*

- Instructor for two undergraduate laboratory courses;
  1. AOE 3054 Experimental Methods
  2. AOE 4354 Ocean Engineering Laboratory

NAVAL ARCHITECT CO-OP
NSWC Carderock (formerly David Taylor Model Basin), detachment Norfolk, Combatant Craft Department, Suffolk VA, *05/96- 08/98*

- Worked with naval architect design code to support and develop Navy, Marine Corp, Army, and Special Warfare high speed craft
- Traveled throughout continental US to perform sea trials, drawing validations, scale weighings and provide on-site support for builders and customers
- Developed stability reports and performed structural analysis on MKV SOC, 120' TWR, 25' PBL, and 25'UB
- Developed Lines and Offsets drawing for Boston Whaler's 25' Guardian

MANAGER/LANDSCAPE ARCHITECT
Mish Brothers Landscaping, Gambrills MD, *04/86 - 08/95*

- Self-employed as landscape architect with approximately 30 clients
- Maintained several town contracts and provided monthly billing services

PROJECTS:

Worked on construction team building classic wood sport-fishing boat

- Worked in all phases of construction employing traditional boat-building techniques from lofting to launch
- Performed resistance and propulsion analysis
- Developed GHS hydrostatic model and performed intact and damaged stability analysis
- Suggested and implemented design improvements

COMPUTER SKILLS:

General HydroStatics (GHS)	AUTOCAD	MathCad
AutoShip	FORTRAN	WINDOWS
MATHEMATICA	MatLab	MS Office

AWARDS:

1999/00 ASNE James A. Pitt Scholarship recipient
1998/99 SNAME student scholarship recipient

PUBLICATIONS:

1. Mish, Patrick F., "Mean Loading and Turbulence Scale Effects on the Surface Pressure Fluctuations Occurring on a NACA 0015 Airfoil Immersed in Grid Generated Turbulence", Masters Thesis, Virginia Tech, June 2001
2. Mish, Patrick F. and Devenport, William J., "Mean Loading Effects on the Surface Pressure Fluctuations on an Airfoil in Turbulence", 7th AIAA/CEAS Aeroacoustics Conference, Maastricht, The Netherlands, 28-30 May 2001
3. Mish P, Wang H, Bereketab S, and Devenport W, "Measurement of the Space-Time Correlation of Surface Pressure Fluctuations on an Airfoil Immersed in Turbulence", Fluids 2000, Denver, CO, 19-22 June 2000
4. Mish, Patrick F., Gregory, Michael W., Mierzwicki, Timothy, Cyre, Jeffery, Chaney, Scott, Petzold, Megan., "Small Waterplane Twin Hull (SWATH) Design", Virginia Tech, June, 1999
5. Mish, Patrick F. and Whitford, Malcolm W., "25 ft Counter-Drug Patrol Boat Light (PBL-CD) Stability Analysis", NSWC det. Norfolk, Combatant Craft Department, November, 1998
6. Roots, Philip and Mish, Patrick F., "120 ft Torpedo Weapons Retriever Stability Analysis and Loading Guidelines", NSWC det. Norfolk, Combatant Craft Department, December, 1997

7. Mish, Patrick F., “MK V Special Operations Craft Increased Range Study”, NSWC det. Norfolk, Combatant Craft Department, May, 1997

ACTIVITIES:

SNAME student member
ASNE student member
AIAA student member
SNAME Virginia Tech Student Chapter 1998-99 Treasurer and Secretary
Church youth group
Peer counselor
Virginia Tech Weight Club